Challenges in the Hunt for Dark Energy Dynamics

Renée Hlozek

Thesis presented for the degree of Master of Science in the Department of Mathematics, Faculty of Science, University of Cape Town

2008

Supervisor: Professor Bruce Bassett

Contents

Acknowledgements

"*The only people with whom you should try to get even are those who have helped you.*" - John E. Southard.

I am really lucky to have many people in my life who have helped and shaped me during my studies. My mom, Glenda, and brother, Nick, have perfected the art of giving me advice when I need it and support when it is hard to 'keep on keeping on'; thank you both for such unconditional love and friendship. To Nicole, my sister across the sea; your loyalty and ability to make me laugh are still so special 21 years into our friendship.

My friends, both old and new have listened (and remained enthusiastic) through all my rantings about work, love and life during the MSc. As friends and fellow students Antonio, Aymen, Hassan, Jean-Claude, Marina, Maye, Melvin, Mike and Patrice have made the UCT Observational Cosmology Group a great environment to learn and grow. Alex, Amanda, Chris, Jeff, Julien, and Kishore have given me lots of food for thought during our discussions about Physics and other cool things in life.

Martin, thank you for your patience (especially when I have had too much coffee), it is a pleasure collaborating with you. I had the pleasure of many visits to the Institute for Cosmology and Gravitation in Portsmouth, so thank you to Bob and Roy and everyone who made me feel so welcome there. A special thanks to Hubert, Mat and David for discussions, aid and Monty Python. Thanks also to Ariel, Linda and Jakob and everyone at the University of Stockholm for discussions, smoked salmon and chocolate.

My degree would not have been the same without my 'non-work' friends: Adri, Amy, Aurélie, Claudia, Jo, Jurgen, Ross, Sarah, Thyla and Wendy; thanks for letting me be light and silly. To the other two of the Three Muskateers, Jacques and Yabe: I have learned so much from you, thank you for your friendship and collaboration. I look forward to watching your careers flourish, and hope to collaborate and stay in contact with you for years to come. Go Team Fisher! Many of the great events and outings would not be possible without the help of Michelle; thank you for your quiet support to me and the whole group.

And finally, I could not have hoped for a better experience in my Masters studies than under your supervision, Bruce. As supervisor, mentor and friend you taught me how to fly (and play golf!) The dedication and enthusiasm that you put into our group changes all of your students for the better. You lead by example, and make us strive to be better scientists with passion for what we do. It is fitting that my favourite quote was one that you placed in my path:

"*The young do not know enough to be prudent, and therefore they attempt the impossible - and achieve it, generation after generation.*" - Pearl S. Buck.

Thank you.

Plagiarism Declaration

I know the meaning of plagiarism and declare that all of the work in the document, save for that which is properly acknowledged, is my own.

Figures 1.10, 2.2, 2.3, 2.4, 3.2, 3.5, 3.8, 4.3, 4.4, 4.6, 4.7, 4.8, 4.9 were produced, either explicitly for this thesis or for the research papers they have been reproduced from, using my own code and code written in collaboration (Fisher4Cast).

This degree was funded by the Square Kilometer Array Human Capital Development Program.

Abstract

One of the greatest challenges in modern cosmology is determining the origin of the observed acceleration of the Universe. The 'dark energy' believed to supply the negative pressure responsible for this cosmic acceleration remains elusive despite over a decade of investigation. Hunting for deviation from the 'vanilla' cosmological model, ΛCDM, and detecting dynamics with redshift in the equation of state remains a key research area, with many challenges. We introduce some of the challenges in the search for such dark energy dynamics. We illustrate that under the assumption of well-motivated scaling models for dark energy dynamics, early universe constraints on the dark energy density imply that these models will be essentially indistinguishable from ΛCDM for the next decade. After introducing the Fisher Matrix formalism, we derive the Fisher Flex test as a measure of whether the assumption of Gaussianity in the likelihood is incorrect for parameter estimation. This formalism is general for any cosmological survey. Lastly, we study the degeneracies between dark energy and curvature and matter in a non-parametric approach, and show that incorrectly assuming values of cosmological components can exactly mimic dark energy dynamics. We connect to the parametric approach by showing how these uncertainties also degrade constraints on the dark energy parameters in an assumed functional form for w. Improving the accuracy of surveys and experiments to search for possible signatures of dark energy dynamics is the focus of much attention in contemporary cosmology; we highlight challenges in the hunt for dark energy dynamics.

Table of Definitions

Abbreviation/Symbol	Definition
$g_{\mu\nu}$	The metric (0 for time, $i = 1, 2, 3$ for spatial components)
$G = 6.674 \times 10^{-11}\mathrm{Nm}^2/\mathrm{kg}^2$	Gravitational constant, dimensions of $[L^3/(Mt^2)]$
$1\mathrm{eV} = 1.602 \times 10^{-19}\mathrm{J}$	Electron volt
$m_{\mathrm{pl}} = 1.22 \times 10^{19}$ GeV	Planck mass
$G_F = 1.16637 \times 10^{-5}$ GeV^{-2}	Fermi coupling constant
H_0 [kms^{-1}Mpc^{-1}]	Hubble constant
$\Box \equiv \nabla^2 - \partial^2/\partial t^2$	d'Alembertian
$\epsilon, \eta, \widetilde{\epsilon}, \widetilde{\eta}$	Slow-roll parameters
pc $\approx 3.1 \times 10^{15}$m	parsec
CMB	Cosmic Microwave Background
FLRW	Friedmann Lemaître Robertson Walker
EFE	Einstein Field Equations
CPL	Chevallier-Polarksi-Linder (dark energy parameterisation)
SN Ia	Type Ia Supernova
LRG	Luminous Red Galaxy
BBN	Big Bang Nucleosynthesis
BAO	Baryon Acoustic Oscillations
DETF	Dark Energy Task Force
ΛCDM	Λ Cold Dark Matter
SDSS	Sloan Digital Sky Survey
MCMC	Markov Chain Monte Carlo
FM	Fisher Matrix
FoM	Figure of Merit
FRIIb	Fanaroff-Riley Type IIb Radio Galaxies

Table 1: Definitions and symbols used in the thesis.

Chapter 1

Standard Cosmology

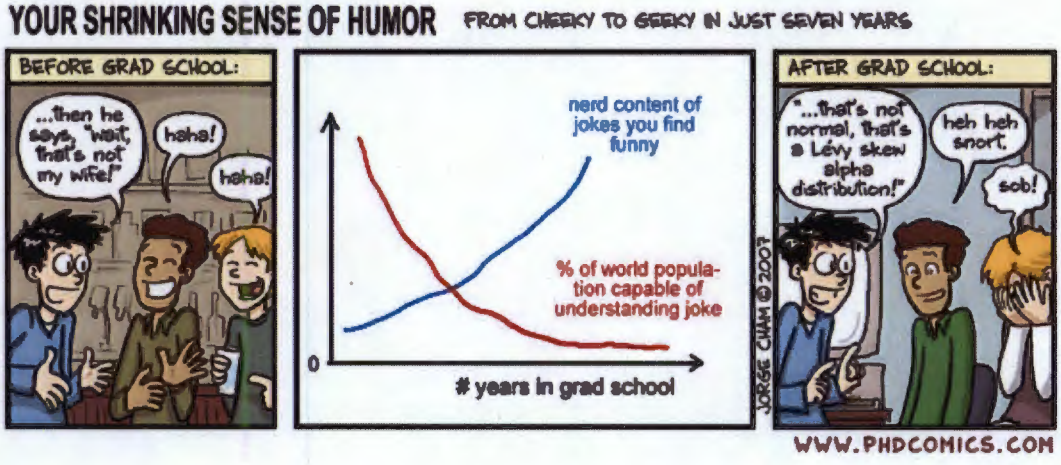

Figure 1.1: © Jorge Cham, online at www.phdcomics.com 30/05/2007

1.1 History of Modern Cosmology

Cosmology is the study of the Universe, its origins and its fate. Humanity has been trying to find answers to questions on the nature of time and space, where we come from and where we are going through the ages. Physical cosmology combines measurements and observations of the Universe with mathematical theories and predictions to try and determine some of the answers to those questions, such as constraining the age or size of the Universe. This constant balance and tension between observations and theory gives rise to many challenges and some successes in answering these age-old questions. We provide here a very brief overview of the modern history of cosmology.

Prior to the beginning of the twentieth century, Newtonian physics with its laws of motion and gravitation was the dominant paradigm. Kepler's laws of motion (which were originally derived by Johannes Kepler in 1605 before the time of Newton) could be derived using Newton's laws of motion, and they had been used to successfully predict the existence of planet Neptune.

However, towards the end of the nineteenth century, the scientific community had reached a state of crisis in that there was no complete understanding of the motion of light. It was assumed that waves of light needed a medium to propagate, like water waves. The famous interferometer experiment of Michelson and Morley was designed to detect such a propagation 'aether' by detecting changes in the time taken for light to bounce between mirrors based on the orientation of the mirrors - they expected the light to move more slowly as it moved through more of the 'aether'. They did not, however, detect any such variation due to the aether. This observational result would later be placed in the context of Einstein's theory of Special Relativity, which defines the speed of light to be constant.

Many theoretical developments were also made towards the end of the 1900's, by people such as Hendrik Lorentz, who introduced a method of converting measurements such as lengths and times between observers at rest and moving observers. The Lorentz transform now bears his name.

These observational results and theoretical insights all paved the way for Einstein's theories, the first of which was published in 1905. Special (and later General) Relativity changed the paradigm of science at the time. Special Relativity defined the speed of light as an upper bound for all motion in the Universe, and included the theory of Lorentz transforms between reference frames of observers. General Relativity would, in addition, radically change the way we view space and matter - in that matter and energy are interchangeable, and that the curvature of space and the energy are related.

One of the outstanding challenges in contemporary cosmology is the direct detection of dark matter. First proposed by Fritz Zwicky in 1933 based on observations of the Coma cluster, dark matter was suggested to explain the rotation curves of galaxies. The mass inferred from the luminosity of these galaxies was unable to account for their rotation. While the origin of this

dark matter is still unknown, there are many observations such as gravitational lensing which seem to confirm the dark matter hypothesis. These observations indirectly detect dark matter in that they detect its gravitational effects, while a confirmed detection of a dark matter particle would, however, rule out different cosmological models.

Various fundamental solutions of the Einstein Field Equations were developed in the years following the formulation of the theory of General Relativity, with some of the most well known being the Schwarzschild black-hole solution to the field equations, and the Friedmann-Lemaître-Robertson-Walker (FLRW) expanding universe, first suggested by Alexander Friedman in 1922.

Einstein was himself biased towards a static model of the Universe, and so introduced the concept of the cosmological constant, or Λ, which he later recalled as his greatest blunder. The observations by Edwin Hubble and Vesto Slipher which led to Hubble's law in 1929, however, indicated a correlation between the distance of galaxies and their redshifts. In other words, galaxies further away from us were moving away from us with greater speed. This was conclusive evidence in support of the FLRW solutions, and the expanding Universe.

These theoretical and observational results started intense debate in the scientific community about the origin of the expanding Universe, as opposed to the infinite static Universe proposed by people such as Hermann Bondi, Thomas Gold and Fred Hoyle, who invented the term 'Big Bang' as a derogatory term for the expanding Universe theories, which has stuck to this day.

The overwhelming support of the expanding Universe, however, came from the discovery of the Cosmic Microwave Background (CMB) by Penzias and Wilson in 1965, which confirmed the predictions of theorists such as Ralph Alpher, Hans Bethe and George Gamow on the production of elements and the relic radiation (the CMB) from such a hot big bang. The CMB is still an active research area in modern cosmology. Measurements of the CMB from experiments like the Cosmic Background Explorer (COBE) [1], the Arcminute Cosmology Bolometer Array Receiver (ACBAR) [2], MAXIMA [3], the Cosmic Background Imager (CBI) [4], Balloon Observations of Millimetric Extragalactic Radiation and Geophyiscs (BOOMERANG) [5] and the Wilkinson Microwave Anisotropy Probe (WMAP) [6] have constrained various cosmological parameters. The power spectrum data from these experiments is given in Figure 1.2, which is found in [7] as Figure 2.

The CMB also provides support for another important theory of cosmology, that of inflation. In the early 1980's, a period of rapid inflation the early Universe was proposed [8, 9, 10, 11, 12] to explain the following key problems in cosmology.

- The Flatness problem arises because present observations of the Universe suggest that the universe is nearly flat, however in standard big-bang theory the Universe would evolve away from flatness (either expand or collapse) very quickly.
- The Horizon problem describes the fact that the size on the sky of causally connected regions should be no larger than 1°, whereas the CMB sky is the same temperature to high

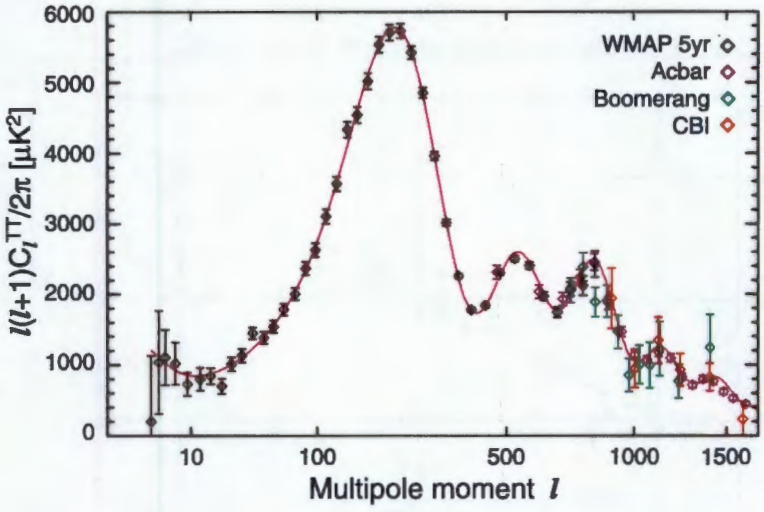

Figure 1.2: **The power spectrum of the Cosmic Microwave Background.** The power spectrum from WMAP, as Figure 2 in [7]. combined with data from the ACBAR ([2] **purple**), BOOMERANG ([5] **green**), and CBI ([4] **red**) experiments. The red curve is the best-fit ΛCDM model to the WMAP data. Measurements of the CMB constrain cosmic parameters such as the energy density of dark energy, and provide tests for various models of inflation.

precision ($\Delta T/T < 10^{-5}$).

- The origin of structure problem refers to the fact that the temperature fluctuations are distributed on such large scales that it would not be possible to generate them in a FLRW metric between the Big Bang and the epoch of last scattering, via causal processes [13].
- The relic density problem describes the fact that symmetry breaking in the early universe would have produced many relic magnetic monopoles and other topological defects which should be present and plentiful today, which again are not observed [13].

Inflation answers these problems by having a period of rapid expansion in the early universe. This stretching out of space drives the universe towards flatness, as this rapid expansion would allow causal contact between regions larger than the 1° regions we observe today, since they would in fact have been close together in the early universe, thereby solving the horizon problem. Inflation also provides a causal mechanism to generate the fluctuations which will seed the structure in the universe, through fluctuations in the inflaton field. Lastly, during inflation the energy density of the Universe decreases slowly, while the energy density of the magnetic monopoles decreases like a^{-3}, and so these monopoles will be red-shifted away during the expansion, provided the period of inflation is long enough [13]. Today much interest centers around testing the inflationary model which has provided such a strong link to the cosmos we observe today and the quantum

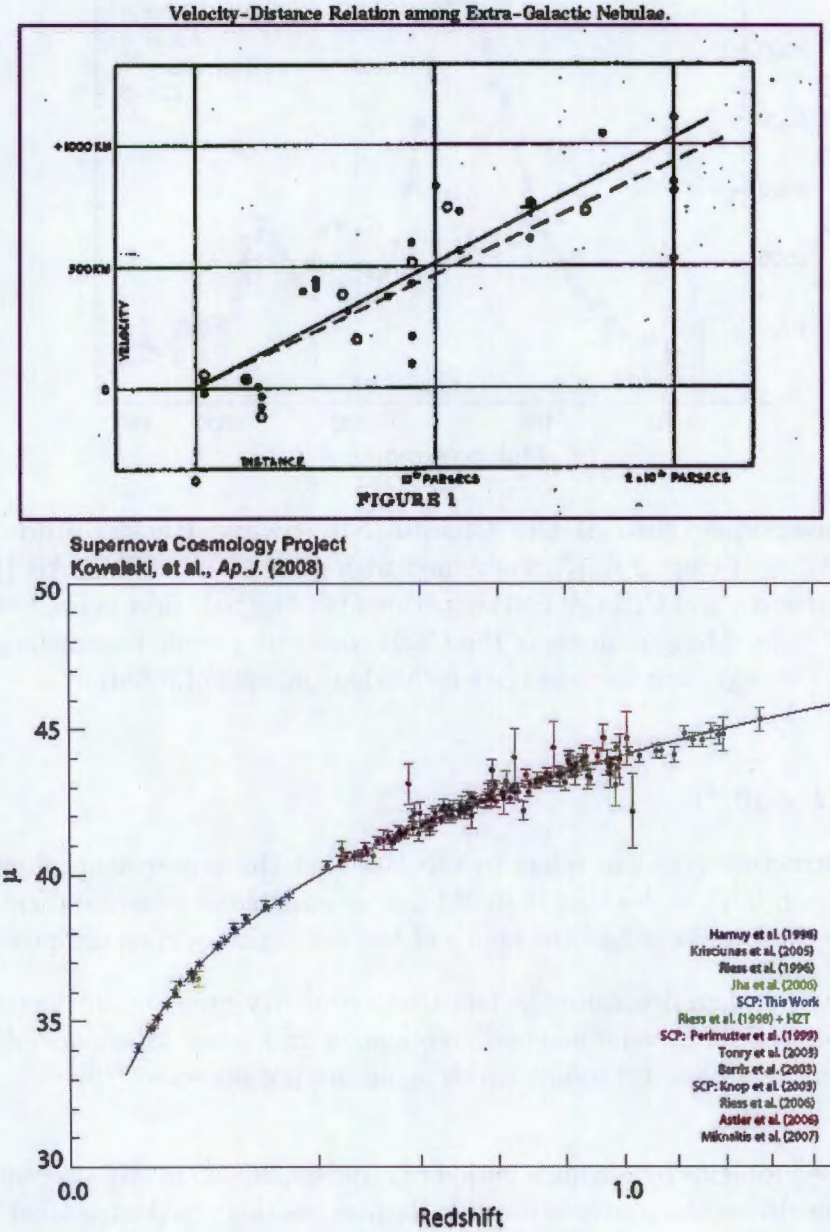

Figure 1.3: **The Hubble diagram - then and now.** Hubble's original plot (**top**) of the velocity-distance relation of galaxies provided evidence for the expansion of the Universe, which is Figure 1 in [18]. The estimated constant (later known as the Hubble constant) in the relation was an order of magnitude too large. Measurements of SNe Ia from various surveys (**bottom figure**), collated in [19], show not only that the universe is expanding, but suggest that the expansion is in fact accelerating.

nature of the early Universe [14, 15, 16, 17]. A review of inflationary models can be found in [13].

Another significant change in the cosmological paradigm occurred with the observations of Type Ia Supernovae (SNe Ia) [20, 21], which strongly suggest that the Universe is not only expanding as found by Hubble and others, but that it is doing so at an ever increasing rate. Figure 1.3 shows Hubble's original plot of velocity and distances [18] together with a contemporary Hubble diagram from the Union Supernova Compilation [19]. Complimentary observations, such as the CMB, provide further support to this claim of late-time acceleration. The problem with this current paradigm is that the origin of this acceleration, which has been dubbed the 'dark energy', is unknown.

This exciting history seems to leave us with more questions than answers. As the scientific community struggles to understand the nature and origin of dark matter and even more so of dark energy, we are again poised at the brink of a paradigm shift, when the ideas and theories of the past are re-evaluated and we search for new theories to explain the Universe we observe.

In the sections that follow we will outline some of the key concepts in modern cosmology, and the mathematical tools needed to make inferences about the Universe we inhabit.

1.2 The Metric

In general relativity the metric is defined in terms of the line element as

$$ds^2 = g_{\alpha\beta}dx^\alpha dx^\beta, \tag{1.1}$$

where the 'upper' indices are contravariant and the 'lower' indices are covariant indices, and we make use of the Einstein summation convention. We define the 4-vector $dx^\alpha = (cdt, dx, dy, dz)$ in flat space. Throughout this work we will use the metric signature (-1,1,1,1). Table 1 contains a list of further notation and abbreviations we will follow; Appendix A gives a short introduction to Tensor Algebra.

The inverse metric $g^{\alpha\beta}$ is defined so that the product $g^{\alpha\beta}g_{\beta\gamma} = g_{\gamma\beta}g^{\beta\alpha} = \delta^\alpha_\gamma$, where δ^α_γ is the Kronecker delta. We can use the metric (and its inverse) to raise and lower indices of general tensors, for example, $t^{\beta\gamma}_\alpha = g_{\alpha\nu}t^{\nu\beta\gamma}$.

1.3 Curvature

The metric is used to calculate geodesics (analogous to the 'shortest distance between two points' in Euclidean space), and will describe the motions of test particles. In this section we define

derivatives in curved space, and illustrate how the curvature of the space is fully contained within the metric.

Firstly, we define the concept of a derivative in a curved space, known as the covariant derivative, ∇_μ. It is defined in terms of the usual partial derivative ∂_μ and the Christoffel symbols, or connection coefficients $\Gamma^\nu_{\mu\lambda}$, as

$$\nabla_\mu = \partial_\mu + \Gamma^\nu_{\mu\lambda}. \tag{1.2}$$

This covariant derivative is a tensor, and so obeys all the transformation properties of a tensor (see Appendix A for an introduction to tensor algebra). One of the key characteristics of the metric tensor is that the covariant derivative is 'compatible' with the metric tensor [22], or $\nabla_\rho g_{\mu\nu} = 0$. This property defines the connection in terms of the metric tensor and its derivatives,

$$\Gamma^\sigma_{\mu\nu} = \frac{1}{2} g^{\sigma\rho} \left(\partial_\mu g_{\nu\rho} + \partial_\nu g_{\rho\mu} - \partial_\rho g_{\mu\nu} \right). \tag{1.3}$$

We assume here without proof the Riemann tensor (or curvature tensor) to be given as

$$R^\rho_{\sigma\mu\nu} = \partial_\mu \Gamma^\rho_{\nu\sigma} - \partial_\nu \Gamma^\rho_{\mu\sigma} + \Gamma^\rho_{\mu\lambda}\Gamma^\lambda_{\nu\sigma} - \Gamma^\rho_{\nu\lambda}\Gamma^\lambda_{\mu\sigma}. \tag{1.4}$$

We can perform contractions on the Riemann tensor over one index to yield the Ricci tensor; $R_{\mu\nu} = R^\lambda{}_{\mu\lambda\nu}$ and over two indices to form the Ricci scalar: $R = R^\mu{}_\mu = g^{\mu\nu} R_{\mu\nu}$. By performing covariant derivatives of the Riemann tensor, we obtain the Bianchi identity, or

$$\nabla_\lambda R_{\rho\sigma\mu\nu} + \nabla_\rho R_{\sigma\lambda\mu\nu} + \nabla_\sigma R_{\lambda\rho\mu\nu} = 0. \tag{1.5}$$

We perform contraction over Eq. (1.5) twice to obtain

$$\begin{aligned} g^{\nu\sigma} g^{\mu\lambda} \left(\nabla_\lambda R_{\rho\sigma\mu\nu} + \nabla_\rho R_{\sigma\lambda\mu\nu} + \nabla_\sigma R_{\lambda\rho\mu\nu} \right) &= 0 \\ \therefore \nabla^\mu R_{\rho\mu} - \nabla_\rho R + \nabla^\nu R_{\rho\nu} &= 0 \\ \therefore \nabla^\mu R_{\rho\mu} &= \frac{1}{2} \nabla_\rho R. \end{aligned} \tag{1.6}$$

If we then define the Einstein tensor to be

$$G_{\mu\nu} = R_{\mu\nu} - \frac{1}{2} R g_{\mu\nu}, \tag{1.7}$$

then Eq. (1.6) is equivalent to the expression $\nabla^\mu G_{\mu\nu} = 0$.

1.4 Linking Energy to Geometry

The stress-energy (or energy-momentum) tensor $T_{\mu\nu}$, describes the energy content of the universe, and is linked to the geometry of the Universe through the Einstein field equations. It describes the flux of four-momentum p^μ in spacetime orthogonal to the x^ν direction [22, 23].

In a perfect fluid description (which we will address in more detail later), the energy-momentum tensor is simply given by

$$T^{\mu\nu} = \begin{pmatrix} -\rho & 0 & 0 & 0 \\ 0 & p & 0 & 0 \\ 0 & 0 & p & 0 \\ 0 & 0 & 0 & p \end{pmatrix} \tag{1.8}$$

Both the energy-momentum tensor, given by Eq. (1.14) and the Einstein tensor given by Eq. (1.7) satisfy

$$\nabla^{\mu} G_{\mu\nu} = 0, \qquad \nabla^{\mu} T_{\mu\nu} = 0. \tag{1.9}$$

Hence we define a relationship between them, namely

$$G_{\mu\nu} = R_{\mu\nu} - \frac{1}{2} R g_{\mu\nu} = 8\pi G T_{\mu\nu}, \tag{1.10}$$

which is nothing but the tensor form of the Einstein Field Equations (EFE), and relates how the curvature of space reacts to the presence of energy. Figure 1.4 illustrates the link between the energy content and the geometry of space. The energy content curves the space around it, while the geometry of space determines the geodesics along which matter moves [24], which is well summarised by the catch-phrase coined by John Wheeler: 'matter tells space how to curve and space tells matter how to move'.

Figure 1.4: **General relativity links energy and geometry.** This schematic figure illustrates how the energy content of the Universe curves the space around it, while the curvature of space influences the geodesics along which matter travels. Figure taken from [25].

1.4.1 The Energy Conditions

Given the definition of the stress energy tensor, one might ask what the restrictions are on it (and therefore by construction the restrictions on the metric) - or in other words, what are 'realistic' components of the stress-energy tensor. The most common property that we require of $T_{\mu\nu}$ is that only positive energy densities are allowed (or in other words that negative masses are not allowed) [22]. This leads to the formulation of the strong and weak energy conditions.

The weak energy condition states that for all time-like vectors, say χ^μ the density satisfies [22]

$$\rho = T_{\mu\nu}\chi^\mu\chi^\nu \geq 0, \tag{1.11}$$

which also implies that $\rho + p > 0$ for all observers [23].

The strong energy condition on the other hand states that not only that the matter density is non-negative, but that the trace of the tidal tensor is always greater than 0 [22], or that:

$$\left(T_{\mu\nu} - \frac{1}{2}Tg_{\mu\nu}\right) \geq 0, \tag{1.12}$$

in other words that $\rho + 3p > 0$ in a fluid description [23].

The description of the tensor in terms of perfect fluids (in Section 1.6) hence places bounds on the relationship between the pressure and the density of a barotropic fluid.

1.5 The Friedmann Lemaître Robertson Walker Model

Much of modern cosmology centers around the Friedmann-Lemaître-Robertson-Walker (FLRW) model, named after the four scientists who were instrumental in formulating the properties of this solution to the Einstein Field Equations. Alexander Friedmann first derived the main results of the model in 1922, while Georges Lemaître arrived independently at the same results in 1927. Howard Percy Robertson and Arthur Geoffrey Walker also worked on the problem and proved its uniqueness as a spatially homogenous and isotropic metric on a Lorentzian manifold in 1935. These two properties of spatial homogeneity and isotropy are the key distinction between FLRW and other solutions to the EFE.

Isotropy implies that the metric is invariant under spatial *rotation*, or in other words that the Universe looks the same in all directions. Homogeneity, however, implies that the metric is invariant under spatial *translation*, or that the Universe looks the same at all points in space. On small scales this may not be valid but FLRW is constructed under the assumption that these conditions hold on large scales.

These assumptions are used to formulate the FLRW metric, in that isotropy and homogeneity imply maximal symmetry in the spatial directions. The FLRW is also constructed to be an expanding Universe, which fits what we observe today.

1.5.1 The Scale Factor and the Metric

This expansion of the Universe is described by the scale factor $a(t)$, which we explicitly assume to be only a function of time (if there was a spatial component this would violate the assumptions of the model). The FLRW metric is then defined as

$$ds^2 = -dt^2 + a^2(t)\left(\frac{dr^2}{1-kr^2} + r^2\left(\mathrm{d}\theta^2 + \sin^2\theta \mathrm{d}\phi^2\right)\right), \tag{1.13}$$

where the curvature parameter k can take on three values, $-1, 0, +1$, and represents **open**, **flat** and **closed** universes respectively.

The energy content of the universe in the FLRW picture is usually modelled by a perfect fluid, which by definition is a fluid which is isotropic in its rest frame [22]. The energy-momentum tensor in this model is therefore given by

$$T^{\mu}_{\nu} = \mathrm{diag}(-\rho, p, p, p). \tag{1.14}$$

Taking the trace of Eq. (1.14), we obtain

$$T = T^{\mu}_{\mu} = -\rho + 3p \tag{1.15}$$

By taking the 00 term in the conservation equation, or, $\nabla_{\mu} T^{\mu}_{0}$ we obtain

$$\begin{aligned} \partial_{\mu} T^{\mu}_{0} + \Gamma^{\mu}_{\mu 0} T^{0}_{0} - \Gamma^{\lambda}_{\mu 0} T^{\mu}_{\lambda} &= 0 \\ \therefore -\partial_0 \rho - 3\frac{\dot{a}}{a}(\rho + p) &= 0 \end{aligned} \tag{1.16}$$

1.5.2 Evolution Equations

The Einstein field equations are given by Eq. (1.10) as

$$R_{\mu\nu} = 8\pi G\left(T_{\mu\nu} - \frac{1}{2} g_{\mu\nu} T\right) \tag{1.17}$$

The ii components of Eq. (1.10) yield [23]:

$$\frac{\ddot{a}}{a} = -\frac{4\pi G}{3}(\rho + 3p), \tag{1.18}$$

which is known as the acceleration or Raychaudhuri equation.

The $\mu\nu = 00$ component of Equation (1.10) is:

$$\left(\frac{\dot{a}}{a}\right)^2 = \frac{8\pi G}{3}\rho - \frac{k}{a^2}, \tag{1.19}$$

which is known as the Friedmann equation. We define the Hubble parameter to be

$$H \equiv \frac{\dot{a}}{a}. \tag{1.20}$$

With the concept of the scale factor to quantify the expansion of the Universe in the Friedmann-Lemaître-Robertson-Walker metric, cosmological background observables can be defined in this metric. Many cosmological observations are made by recording radiation and determining the fractional change in frequency (or wavelength) of the radiation received in relation to the emitted frequency. Redshift is defined as the dimensionless measure of the fractional change in wavelength, as $z = \frac{a_0}{a} - 1$, since the wavelength of the light is stretched by a, a_0 is the scale factor today (with $a_0 = 1$ in a flat Universe), λ_0 is the wavelength of the received photon, and λ is the wavelength of the emitted photon. Hence one can express the evolution equations either in terms of the redshift z or the scale factor a.

1.6 Cosmological Components

Consider a barotropic fluid with a linear relationship between the pressure and the density or

$$p = w\rho, \tag{1.21}$$

where w is defined as the equation of state of the fluid. This description is used ubiquitously in cosmology, and particularly in dark energy analysis, since we model the dark energy component with such a fluid, where w is either left constant, or is allowed to vary as a function of redshift. This is discussed further in Section 1.11.

The conservation equation $-\partial_0\rho - 3\frac{\dot{a}}{a}(\rho + p) = 0$, (given as Eq. (1.16)) can thus be rewritten in terms of the parameter w; as

$$\frac{\dot{\rho}}{\rho} = -3(1+w)\frac{\dot{a}}{a}, \tag{1.22}$$

with ∂_0 the derivative with respect to proper time. Under the assumption that the equation of state w is constant, we can integrate the above equation to obtain:

$$\rho \propto a^{-3(1+w)} \propto (1+z)^{3(1+w)}. \tag{1.23}$$

The value of w is specified by the type of fluid we consider. We define the density parameter as the density required to ensure flatness of space. More explicitly,

$$\Omega = \frac{8\pi G}{3H^2}\rho \equiv \frac{\rho}{\rho_{crit}} \tag{1.24}$$

is the density parameter, where ρ_{crit} is the critical density of flat space, and is given by $\rho_{crit} = \frac{3H^2}{8\pi G}$. It is important to note that since $H = H(z)$ the critical density will also change as a function of redshift.

1.6.1 Matter and Radiation

We introduced the equation of state in the previous section, and the general form for the energy density of a perfect fluid. A common example of such a fluid is collisionless "dust". When the dominant component of the total energy density of the Universe is that of matter we say that the Universe is matter-dominated.

For this collisionless fluid $w = 0$, and hence the density of matter evolves as $\rho \propto a^{-3}$, which can be understood as the density of matter decreasing with the volume of space, and hence the a^{-3} term.

In the case of radiation, the number density of photons will also decrease with volume in the Universe, but there is an additional component related to the wavelength of the light. Since this is stretched by the same factor a^{-1} we find that $\rho_{rad} \propto a^{-4}$, and hence we from Eq. (1.23) have that $w_{rad} = 1/3$.

1.6.2 Curvature

If we rewrite Eq. (1.19) in terms of Eq. (1.20), and use Eq. (1.24) we find the Friedmann equation in the form

$$\Omega - 1 = \frac{k}{H^2 a^2}. \tag{1.25}$$

Since H^2 and a^2 are both positive, we then find that the critical density and the curvature (the sign of k) are closely related in that if

- $\Omega < 1$
  This means k = -1, which means that the Universe is open.
- $\Omega = 1$
  This implies that $k = 0$, and we have a flat universe.

- $\Omega > 1$
  Hence $k = +1$ and we live in a closed universe.

One can apply the definition that $\Omega_{rad} + \Omega_m + \Omega_k + \Omega_{\rm DE} = 1$, and so if the sum of the other Ω's adds up to less than 1, we have that the curvature energy density (Ω_k) is greater than zero - we have to 'top-up' the Universe with curvature to ensure flatness. The opposite of course applies for if $\Omega_k < 0$; then we are dealing with a closed universe. The curvature of the universe influences the geodesics, in that they remain parallel in a flat universe, they converge in a closed universe and diverge in an open universe. This is illustrated schematically in Figure 1.5 on a map of the CMB taken with the BOOMERANG experiment [5].

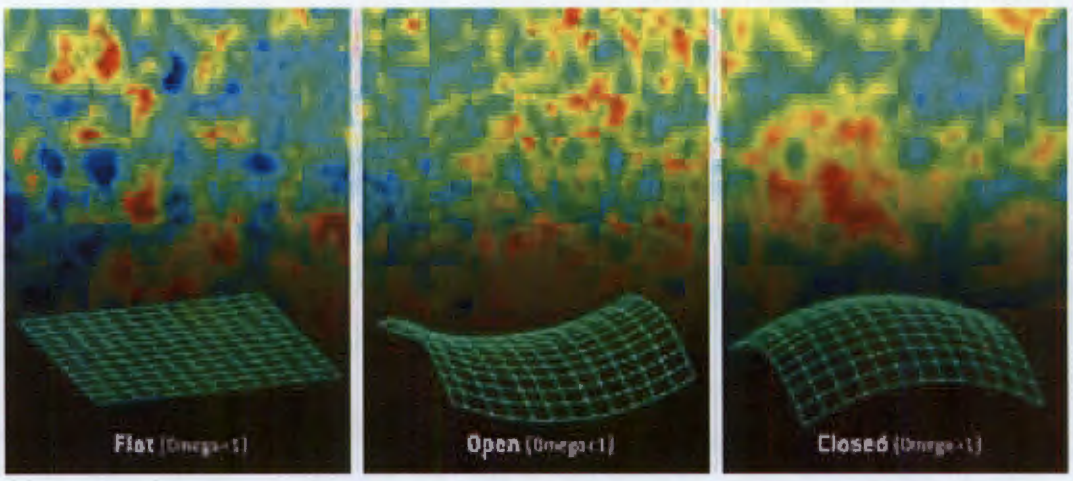

Figure 1.5: **The effect of cosmic curvature on the CMB.** Schematic diagram showing the Cosmic Microwave Background taken by Balloon Observations of Millimetric Extragalactic Radiation and Geophyiscs (BOOMERANG) for different values of the curvature of the Universe. In a closed universe and the geodesics converge, the hot and cold spots would appear larger than in the flat universe case. On the other hand, an open universe would have geodesics that diverge, and so the spot would appear smaller. Figure taken from [26].

1.6.3 Dark Energy in FLRW

The 'cosmological constant' term that Einstein introduced to his solution of GR was originally intended to force a static universe. This idea was abandoned after the discovery that the Universe was in fact expanding, but has been resurrected as the potential agent for the observed cosmological acceleration. We note that we can modify the Einstein equations (Eq. (1.10)) instead as

$$G_{\mu\nu} = 8\pi G T_{\mu\nu} - \Lambda g_{\mu\nu}, \tag{1.26}$$

which will still be invariant under the derivative $\nabla_\mu G^{\mu\nu}$. We can, in fact "absorb" the term with Λ into the general energy tensor, with:

$$T^{\text{vac}}_{\mu\nu} = -\frac{\Lambda}{8\pi G} g_{\mu\nu}. \tag{1.27}$$

The cosmological constant is then described by a perfect fluid with constant energy density $\rho = -p = -\Lambda/8\pi G$, and therefore we see that Λ corresponds to $w = -1$.

We stated the weak and strong energy conditions in Section 1.4.1. Given that we can express the energy momentum tensor in terms of the pressure and density of a perfect fluid, we can express these conditions in terms of those fluid properties. Hence the weak energy condition means that $\rho + p > 0$, while the strong energy condition implies that $\rho + 3p > 0$. The condition for acceleration is $\ddot{a} > 0$. Imposing this condition on Eq. (1.18), implies $\rho + 3p < 0$, or alternatively that $w < -1/3$. Hence we see that acceleration from dark energy violates the strong, but not the weak energy condition.

We now discuss the observables used to constrain cosmological models.

1.7 Hubble Parameter

The Hubble parameter is a measure of the expansion rate of the Universe. It is taken directly from the Friedmann equation, given by Eq. (1.19), which is $(\dot{a}/a)^2 = (8\pi G\rho)/3 - k/a^2$. The total density can be expressed in terms of a sum over the densities of the separate components (excluding curvature since it is the last term on the RHS of Eq. (1.19)) as

$$\begin{aligned} \rho &= \rho_{\text{rad}} + \rho_m + \rho_{\text{DE}} \\ &= \frac{3H_0^2}{8\pi G}\left[\Omega_{rad}(1+z)^4 + \Omega_m(1+z)^3 + \Omega_{\text{DE}} f(z)\right], \end{aligned} \tag{1.28}$$

where H_0 is the Hubble parameter today, $\Omega_m, \Omega_{\text{DE}}$ are the density parameters of matter and dark energy today (as opposed the ρ_m^0 for example, which is energy density of dark energy today) and $f(z)$ is the equation describing the evolution of the density of dark energy as a function of redshift, or

$$f(z) = \exp\left[3\int_0^z \frac{1+w(z')}{1+z'} dz'\right]. \tag{1.29}$$

If we then substitute in the relation (Eq. (1.20)), namely $H = \dot{a}/a$, into Eq. (1.19), we are then left with the equation for the Hubble parameter,

$$H(z) = H_0\sqrt{\Omega_{rad}(1+z)^4 + \Omega_m(1+z)^2 + \Omega_{\text{DE}} f(z) + \Omega_k(1+z)^2}, \tag{1.30}$$

where $\Omega_k = -\frac{k}{H_0^2 a^2} = 1 - (\Omega_m + \Omega_{DE} + \Omega_{rad})$ is the density parameter of curvature. This is also often denoted by

$$H(z) = H_0 E(z), \tag{1.31}$$

where $E(z)$ is clearly the square-root term in Eq. (1.30).

The specific model for dark energy comes enters Hubble parameter via $f(z)$ as an integral over $(1+w(z))/(1+z)$, and so it is clear that any measurements of $H(z)$ will 'smear' out or smooth the contribution from w through the integral.

1.7.1 Age Measurements

The Hubble parameter can be measured indirectly through differential measurements of the ages of sources such as luminous red galaxies (LRGs) [28, 29]. This can be seen by considering the equation for the Hubble rate (eq. (1.20)) and substituting into it the scale factor-redshift relation:

$$\begin{aligned} H(z) &= \frac{\dot{a}}{a(z(t))} \\ &= -\frac{1}{1+z}\frac{dz}{dt}. \end{aligned} \tag{1.32}$$

Hence precise measurements of the age of the sources over a redshift range are needed to estimate $H(z)$. The spectra of LRGs evolve with age and hence by fitting the observed spectrum to simulated spectra we can accurately determine the age of the galaxy (at a particular redshift) and thus determine $H(z)$. Figure 1.6 gives an example of the image and spectrum of a LRG, taken from the Sloan Digital Sky Survey (SDSS) [27].

1.7.2 Baryon Acoustic Oscillations

Another way to determine the Hubble parameter as a function of redshift is to measure the Baryon Acoustic Oscillations (BAO) in the matter power spectrum of galaxies. We give a very brief summary of the technique here, detailed descriptions of the physics and the measurement techniques of the BAO can be found in [30, 31, 32, 33, 34].

The baryon acoustic oscillations result from physical processes in the early universe. Before the Universe cooled enough for protons and electrons to combine to form atoms, the universe consisted of a hot plasma of photons and baryons which were tightly coupled via Thomson scattering.

The competing forces of radiation pressure and gravity set up oscillations in the photon fluid. Because of the tight coupling of the photons to the baryons, the perturbations in the coupled fluids

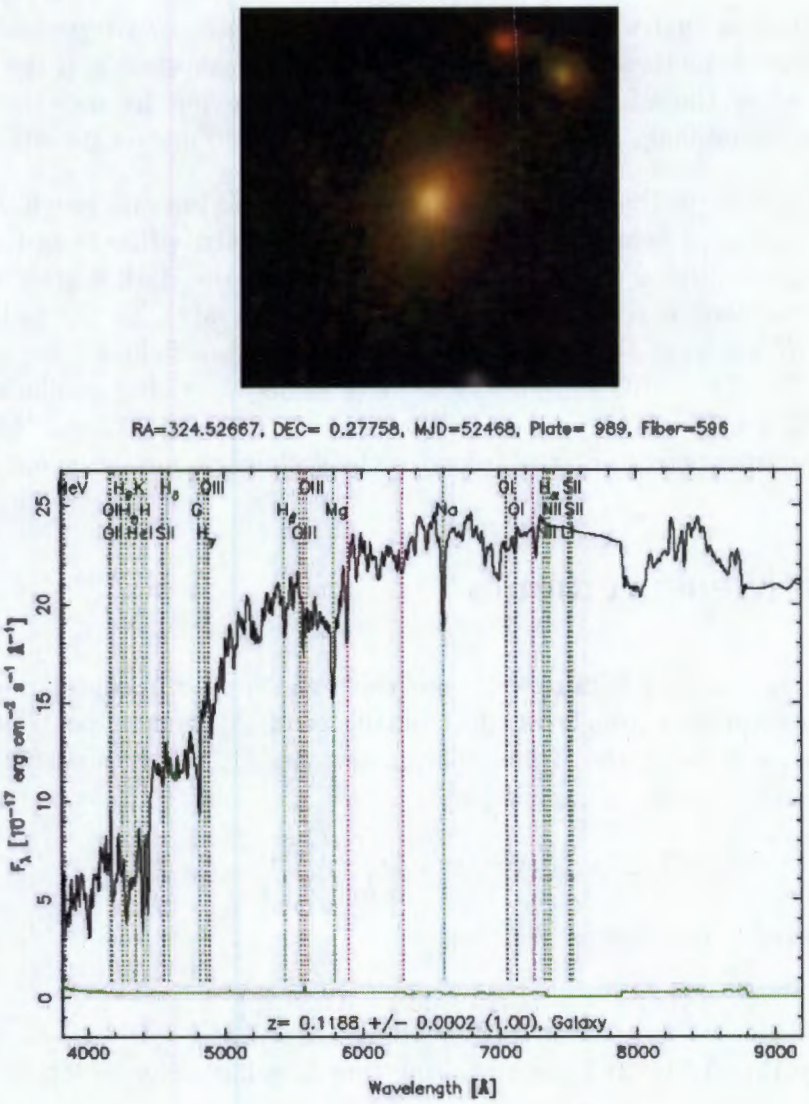

Figure 1.6: SDSS image and spectrum of a typical LRG with $(\text{ra}, \text{dec}) = (324.527, 0.2776)$. The spectra of these passive, red galaxies (note from the image the lack of blue light from young hot stars) evolve with redshift in a well-described way. Hence measurements of the ages of these galaxies at different redshifts yields a measurement of the Hubble parameter. Figures taken from [27].

oscillated as sound waves with sound speed in the plasma of $v = c/\sqrt{3}$. This pressure-supported oscillation continued until recombination, when the photons decoupled from the baryons in the plasma and the photons free streamed away, removing the pressure support. This radiation is the cosmic background radiation that we observe redshifted into the microwave part of the electromagnetic spectrum. The characteristic scale of the oscillations is imprinted on the distribution of the baryons and is set by the sound horizon, which is the comoving distance the sound wave could have travelled by decoupling, and depends on the baryon and matter densities.

After decoupling dark matter in the universe and the baryons still interact gravitationally, and so the dark matter also clumps near this excess in the baryon distribution from the oscillation scale. This means that the characteristic scale is imprinted in the dark matter distribution. Measurements of this oscillation scale, which we will denote by $s(z)$, in the radial direction give measurements of H via $s'(z) = c/H(z)$ where c is the speed of light. Using this method, Gaztanaga *et al.* use the SDSS LRG sample [35] to reconstruct the radial oscillation scale and find $H(0.24) = 79.7 \pm 2.1 \pm 1$ kms^{-1}Mpc^{-1} and $H(0.43) = 86.5 \pm 2.5 \pm 11$ kms^{-1}Mpc^{-1}, where the first error is the statistical error and the second is the systematic measurement error.

1.8 Distance Measurements

Distance measures are another key background observable which used in contemporary cosmology. Curvature alters distances through its effect on the geodesics and its contribution to the expansion of the Universe through the Hubble parameter, Eq. (1.30). It is useful therefore to define the comoving radial distance, $D_r(z)$ as [36]

$$D_r(z) = \frac{c}{H_0}\chi(z) \equiv \frac{c}{H_0}\int_0^z \frac{dz'}{E(z')}, \tag{1.33}$$

and the comoving transverse distance as [36]

$$D_t(z) = \frac{c}{H_0}\frac{1}{\sqrt{-\Omega_k}}\sin\left(\sqrt{-\Omega_k}\chi(z)\right), \tag{1.34}$$

where $E(z)$ is given by Eq. (1.31). It is worth noting that in a flat universe ($\Omega_k = 0$), $D_t(z) = D_r(z)$.

Eq. (1.34) shows the explicit link between curvature and distance in the Universe. This link can be intuitively understood in that the curvature changes the geodesics on which light travels, hence measurements of distances are crucial in determining the curvature. This is illustrated schematically in Figure 1.7.

The definition of the radial and transverse distances are in turn used to define the angular diameter distance $d_A(z)$ and luminosity distance $d_L(z)$ as a function of redshift [36]:

$$d_L(z) = (1+z)D_t(z), \quad d_A(z) = \frac{D_t(z)}{1+z}. \tag{1.35}$$

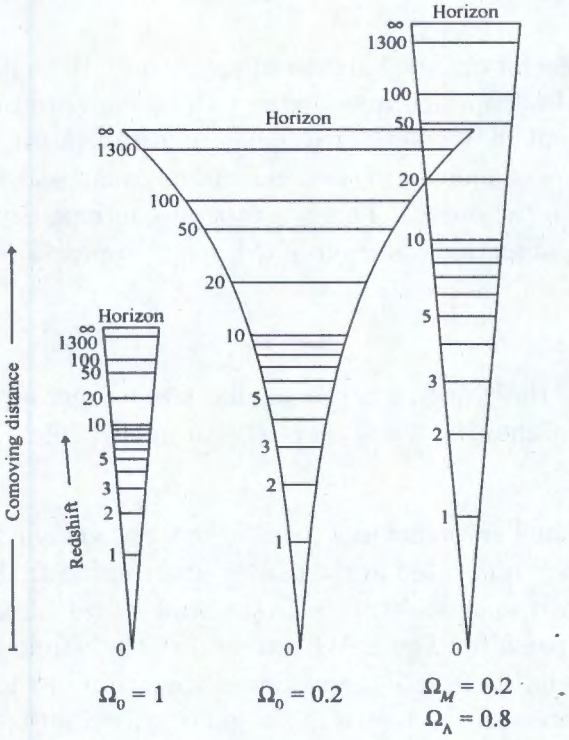

Figure 1.7: This figure, taken from [37], illustrates the relationship between the curvature of the space, distances and physical sizes in the Universe. Each wedge in the diagram is of a cone of *fixed* opening angle, with the observer (us) at the point of the cone, at zero redshift. The wedges illustrate the connection between the comoving radial distances (the vertical direction) and transverse (horizontal) directions, and the physically observable quantities such as redshift (marked as the 'long arms' of the triangle) and angular separation. These are shown here for three different cosmological models, namely a flat matter-dominated Universe in the left panel, an open matter-dominated Universe with $\Omega_0 = 0.2$ (whereΩ_0 is the total Ω) in the middle of the row, and finally a flat Universe with a cosmological constant, $\Omega_\Lambda = 0.8$ on the right.

By examining Eq. (1.35) we note the distance duality $d_L(z) = (1+z)^2 d_A(z)$, which is valid in all metric theories of gravity. Independent measurements of luminosity distance and angular diameter distance can be used to test whether this duality holds in the observable Universe [38].

1.8.1 Angular Diameter Distance from Baryon Acoustic Oscillations

We have given the equations for distance in cosmology, as both the angular diameter distance and the luminosity distance. However, one must extract those distance measures from observations. For this we need the concept of a 'ruler', or a fixed quantity against which we can compare our measurements. In the case of angular measurements, angular scales measured on the sky are converted into a distance to the object. This is a process continuously performed on Earth when determining how far away something is from how large it appears. Mathematically the angular diameter distance is

$$d_A = \frac{L}{\theta}, \tag{1.36}$$

where L is the true scale of the object, θ is the angular size we measure and d_A the angular diameter distance. Clearly then knowing the scale of the 'standard ruler' L is crucial in determining d_A.

The linear theory behind the baryon acoustic oscillations was outlined in the previous section. It is this known oscillation scale imprinted in the matter distribution that we then use to reconstruct the transverse comoving distance as $s(z) = D_t(z)$, and hence measure the angular diameter distance as a function of redshift. The BAO reconstruct the 'standard ruler' statistically from measurements of the correlation function and power spectrum of the galaxy distribution. This acoustic scale has been successfully detected in the galaxy distribution [32, 30, 31, 39], and future surveys will concentrate on measuring both the angular diameter distance and Hubble parameter at high redshift $z \approx 3$ in coming years [40, 127, 41, 42].

The angular diameter distance is not only probed using the BAO. Observations of Fanaroff-Riley IIb (FRIIb) radio galaxies use the angular size of large extended radio jets in the galaxies as a standard ruler [43], while compact radio sources [44, 45] and observations of X-ray clusters [46] are examples of other 'standard rulers' to measure the angular diameter distance.

1.8.2 Luminosity Distance from Type Ia Supernovae

As opposed to a 'standard ruler', another state of the art technique uses 'standard candles' to determine the distance to cosmological objects. The concept of a standard candle is a simple one that we use intuitively on a daily basis. Consider a source with a known luminosity L, and flux F. The flux received from that object decreases spherically symmetrically with the distance

from the source as

$$F = \frac{L}{4\pi d_L^2}. \tag{1.37}$$

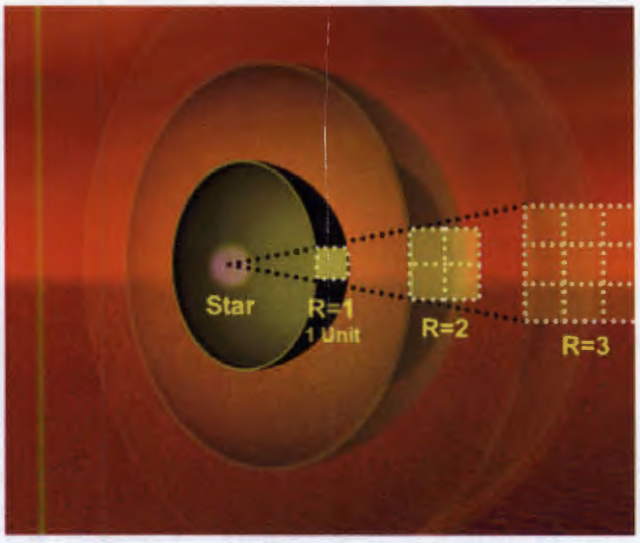

Figure 1.8: **The relationship between luminosity and flux.** Assuming spherically symmetric radiation propagating from an object, the flux received decreases with the inverse of distance squared. This defines the luminosity distance. Figure taken from [47].

Using fluxes leads us to the notion of the magnitude of an object. The luminosity distance is defined in terms of the apparent magnitude m of the object (the magnitude that we observe) and the absolute magnitude M, which is defined to be the apparent magnitude the source would have at a standard distance (for example 10 Mpc), or

$$\mu = m - M = 5 \log d_L + 25, \tag{1.38}$$

with d_L measured in Mpc as given in the first equation in Eq. (1.35), and $\mu = m - M$ is defined as the distance modulus of the object. Of course both μ and d_L vary with redshift.

SNe Ia were first conclusively used as standard candles to detect the acceleration of the Universe [20, 21]. Certain assumptions about the amount of mass in each explosion of the SN Ia and the key characteristics of the explosion are used in order to exploit them as such standard candles. Firstly it is assumed that the white dwarf progenitors are in accreting binary systems and explode once they exceed the Chandrasekhar mass limit of $1.4 M_\odot$, where the dot refers to solar mass. This uniformity in mass leads to a uniformity in the energy released during the explosion, and hence a uniformity in the intrinsic luminosity of the sources. More importantly, however, an empirical correlation between lightcurve decay time and the intrinsic brightness of the SN at maximum light [50, 51] is used to standardize these sources, and reduce the scatter in the distribution of

absolute magnitudes of the SNe Ia. This in turn reduces the error in the estimate of the distance modulus of these objects. The distance modulus is plotted as a function of redshift, and different cosmological models are fitted to this data, enabling us to constrain cosmological parameters in those models.

Future missions will continue to use SNe as cosmological acceleration probes, from space (e.g.[52]) and from the ground (e.g. [53]), and will probe to higher redshifts in order to constrain parameters like dark energy more effectively.

1.9 Volume Measurements

Another background observable can be made from combinations of measurements of the distance measure and the Hubble rate. The comoving volume per unit solid angle $\mathrm{d}\Omega$ on the sky and per unit redshift z is defined as

$$V'(z) \equiv \frac{\mathrm{d}^2 V}{\mathrm{d}z\mathrm{d}\Omega} = \frac{c^3 D(z)^2}{H_0^2 H(z)}, \tag{1.39}$$

where the prime is the derivative with respect to redshift. This clearly shows that measurements of the volume depend on the cosmic parameters in a model through their contribution to the distance and the rate of expansion of the Universe. For example, the degeneracy between curvature and the dark energy contribution is discussed in Chapter 4.

1.9.1 Galaxy Clusters as a Volume Tracer

In principle, one way to measure the volume is to measure the number counts of galaxies, or the apparent abundance of galaxies per unit redshift and solid angle [54] $\mathrm{d}N/\mathrm{d}z$, as

$$\frac{\mathrm{d}N}{\mathrm{d}z} = n(z)\frac{\mathrm{d}V}{\mathrm{d}z}, \tag{1.40}$$

where $n(z)$ is the comoving number density of the particular object. This test has been shown to have the potential to constrain cosmology effectively when $n(z)$ is known (for example it is predicted by the luminosity function of the object) and also when $n(z)$ is very sensitive to the underlying cosmology [54].

The Atacama Cosmology Telescope (ACT) [55, 56] and South Pole Telescope [57] use the Sunyaev-Zel'dovich (SZ) effect to detect clusters in the microwave region of the electromagnetic spectrum. The Dark Energy Survey (DES) [58], whose imaging area was selected to overlap with the SPT, will correlate the SZ decrement with the optical richness of the clusters measured using multi-band photometry in the optical regime, as a function of redshift. Surveys like the Deep

Extragalactic Evolutionary Probe 2 (DEEP2) [54, 59] however, take spectra of galaxies in fields on the sky, and group them as a function of their redshift and velocity dispersion. These 'groups' of galaxies are then counted and used in the above prescription to constrain dark energy.

1.10 The Dark Energy Task Force Experiment Stages

In discussing current and future experiments, it is useful to classify the experiments in terms of cost, timescale and precision. The report of the Dark Energy Task Force [60] defines stages of current and future dark energy surveys. Stage I represents dark-energy projects that have been completed while Stage II represents current dark energy experiments. In this work we are more interested in the Stage III and Stage IV experiments: Stage III comprises near-term, medium-cost, currently proposed projects, such as WFMOS [40, 61], and Stage IV comprises long-term future dark energy projects, including those such as the Large Synoptic Survey Telescope (LSST) [53, 62] and the proposed experiments of the Joint Dark Energy Mission (JDEM) such as the SuperNova Acceleration Probe (SNAP) [52].

1.11 Dark energy

Measurements of the expansion rate and distance probes provide strong evidence for acceleration in the late Universe. An accelerating Universe driven by a component with negative pressure acting against gravity was suggested in the late 1990's [63, 64, 65, 66]. Measurements of the luminosity distance of SNe Ia by two independent groups [21, 20] confirmed this acceleration; the supernovae 'standard candles' were too far away given only a flat, expanding Universe. Since then understanding the nature of the 'dark energy' driving the acceleration remains one of the biggest challenges in observational cosmology.

The original SNe Ia data has been supplemented both by larger SN samples [68, 69, 19, 70, 71], by observations of the CMB [1, 26, 4, 2, 6], measurements of the BAO in the distribution of galaxies [32, 35, 31, 39], angular diameter distance constraints from X-ray clusters [46] and compact radio sources [44, 45] and weak and strong lensing [72, 73, 74]. While the data from one experiment might be explained without acceleration, the combination of data from these different and complimentary probes strongly supports an accelerating cosmos, and allows us to constrain how much of the total energy is 'dark'. For example, the CMB constrains the flatness of the Universe through the acoustic peaks [1]. Combined with constraints on the matter content from observations of clusters [46, 75, 76, 77], this suggests that the dark energy component contributes roughly 70% of the energy density of the Universe at late times. Figure 1.9 from the Supernova Cosmology Project [78, 67] illustrates the complimentarity between different probes.

[1] Although we note that curvature is degenerate with the dark energy. This is discussed in Chapter 4.

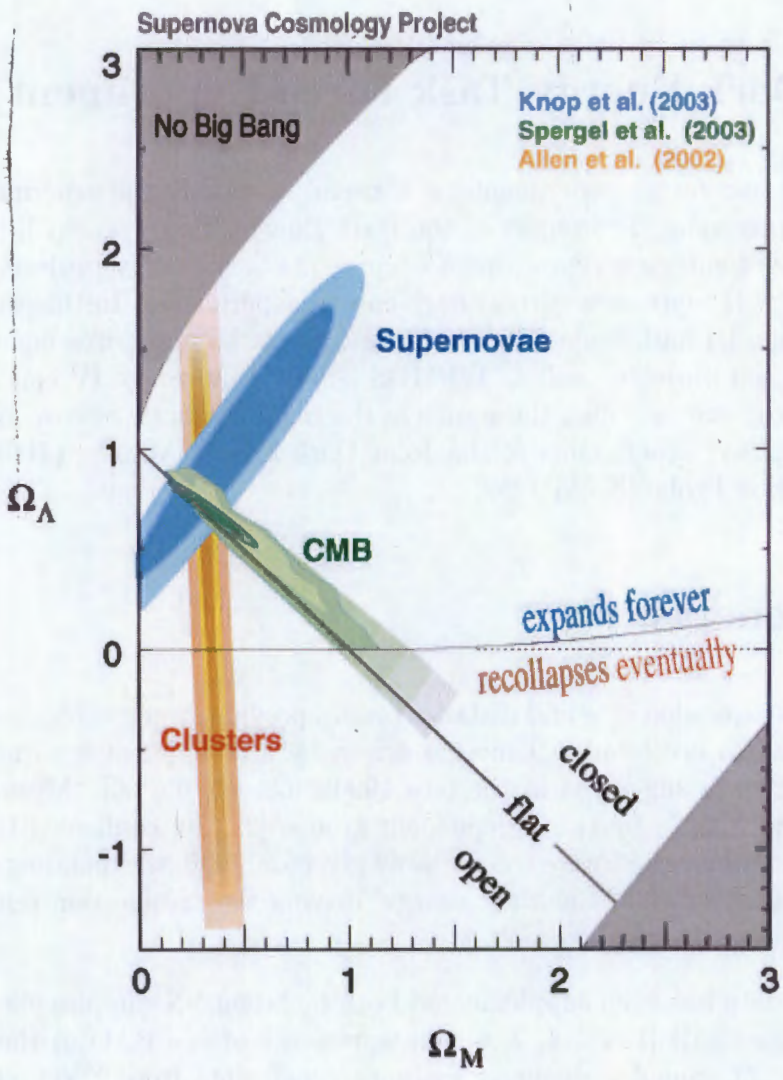

Figure 1.9: **Combining data from many probes.** Multiple probes provide constraints on the densities of dark energy and dark matter in the Universe. Measurements of galaxy clusters (**orange ellipse**) constrain Ω_m but not dark energy (the degeneracy direction is vertical) while the CMB suggests that the Universe is nearly flat (**the green ellipse**). Hence combining these probes with data from the SNe (**blue ellipse**) constrain Ω_m, Ω_Λ. Figure taken from [67].

The different degeneracy directions in the $\Omega_m - \Omega_\lambda$ plane combine to give tight constraints on the matter and dark energy densities.

1.11.1 Challenges in Dark Energy

The evidence for acceleration in the Universe has provided modern cosmology with many challenges. A fundamental problem is that of the Coincidence Problem. Observations suggest that the acceleration of the Universe started at a time remarkably similar to the beginning of life, so it would appear we live at a very special time in the Universe. While acceleration at redshifts much larger than 2 would mean that galaxies would not be able to form, and hence life would not exist as we know it, one might ask why we happen to live so near the start of acceleration? This could also be restated in terms of the size of the density parameters of the Universe, since given that $0 < \Omega_{\rm DE}, \Omega_m < \infty$ (assuming the energy conditions hold), we happen to observe $\Omega_{\rm DE} \approx \Omega_m$ today. If we reject the idea that we live at this special time, we need to challenge the fundamental assumption of the Copernican Principle, that we do not live at a special place in the Universe. This has been investigated recently in the literature [79].

In addition to the Coincidence Problem - that we live near the onset of acceleration, the origin itself of the cosmic acceleration still remains a mystery. In the current 'flavour of the month' cosmology, dark energy as a cosmological constant Λ is the driving force behind this observed acceleration. This constant term Λ was introduced by Einstein almost a century ago in 1918 in order to impose a static Universe in his solutions, and was recently revived as the ideal candidate for the dark energy in that is occurs naturally as the vacuum energy density of the Universe in particle physics. The problem with this explanation is that if Λ originates from the vacuum, it is in fact expected to be much larger than we what we observe today, given that Λ is of the same order as the value of the Hubble constant, or $\Lambda \approx H_0^2 = (2.13h \times 10^{-42}{\rm GeV})^2$, where h is the Planck constant [80]. This means that the energy density of the dark energy today is

$$\rho_\Lambda = \frac{\Lambda m_{\rm pl}^2}{8\pi}, \tag{1.41}$$

with $m_{\rm pl} = 1.22 \times 10^{19}{\rm GeV}$ as the Planck mass. The attractive property of Λ was that one can sum the zero-point energies of the vacuum together to account for the value of Λ. The vacuum energy that results from summing the zero-point energies of quantum fields with mass m is given by the following integral over momentum vector $\mathbf{k}$ [80]:

$$\begin{aligned} \rho_{vac} &= \frac{1}{2}\int_0^\infty \frac{d^3\mathbf{k}}{(2\phi)^3}\sqrt{k^2+m^2} \\ &= \frac{1}{4\pi^2}\int_0^\infty k^2\sqrt{k^2+m^2}\, dk, \end{aligned} \tag{1.42}$$

where in the second line we have assumed spherical symmetry to integrate out angular component, to get a volume of 4π. Clearly this integral diverges, unless you apply some cut-off scale

k. Various theories give different values for this cut-off scale (for example at the Planck mass mp $= 1.22 \times 10^{19}$GeV), but these methods typically yield values of the energy density of Λ that is far too large, by around 120 orders of magnitude. This major challenge is commonly known as the fine tuning problem.

1.11.2 Parametrisations of Dynamical Dark Energy

The cosmological constant, or Λ can be seen as a *constant* dark energy equation of state $w = -1$. Even given all the theoretical mysteries surrounding Λ, however, it seems to provide a good fit to current data [6, 30, 31, 32, 68, 69]. Recently, attention has been focused on detecting dynamical evolution in the dark energy equation of state, in other words if $w = w(z)$.

A plethora of dark energy parametrisations can now be found in the literature. Some approaches are to parameterise the dark energy equation of state with a Taylor series in z with w_0, the late-time value of the equation of state. One example of this was proposed as [81]

$$w(z) = w_0 + w_1 z + w_2 z^2 + ... \tag{1.43}$$

Another popular model is to parameterise the redshift dependence of the equation of state using instead the scale factor itself and not the redshift, for example the Chevallier-Polarski-Linder (CPL) parametrisation [82, 83]

$$w(a) = w_0 + w_a(1 - a), \tag{1.44}$$

which can be written in terms of redshift as

$$w(z) = w_0 + w_a \frac{z}{1+z}. \tag{1.45}$$

Others [84, 85] consider a 4-parameter family of curves, given (for example) by

$$w(z) = w_0 + \frac{(w_f - w_0)}{1 + \exp\left(\frac{z_t - z}{\Delta}\right)}, \tag{1.46}$$

where $w_0 = 0$ is the initial equation of state, w_f is the final equation of state, z_t is the redshift of the sharp transition and Δ is the width of the transition, which describes how rapidly the dark energy changes. These parametrisations of dynamical dark energy are illustrated schematically in Figure 1.10.

Models such as the 'kink' parametrisation [84, 85] allow for more flexibility in the dark energy, and therefore can describe dynamics more effectively than a very compressed parametrisation, such as Eq. (1.45). However, we are only sensitive to observables which contain at least one integration over redshift, and will 'smooth' out features in the dark energy, making it harder to

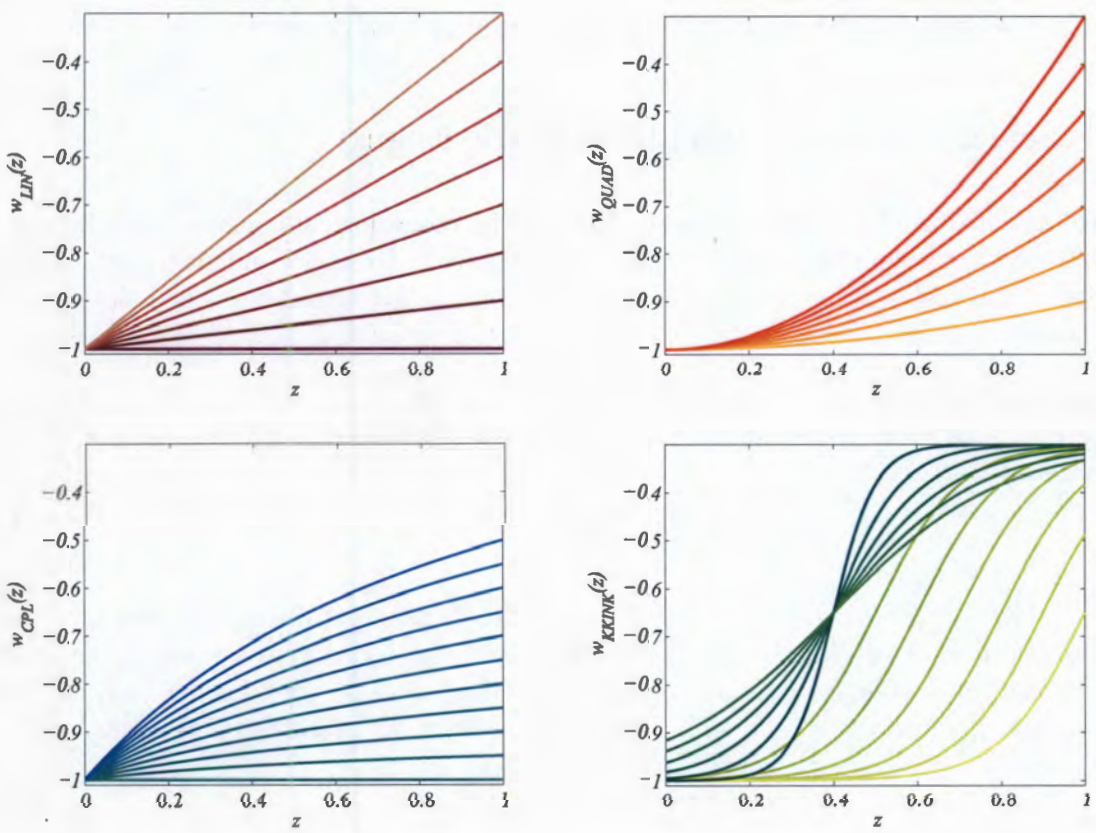

Figure 1.10: **Models of dynamical dark energy.** Schematic plot of various parametrisations, namely the linear parametrisation, or first order Taylor series (**pink curves**) [81], the second-order Taylor series expansion (**red curves**) [81], the CPL parametrisation (**blue curves**) [82, 83] and the four parameter 'kink' model of dark energy (**green curves**) [84, 85]. The curves are plotted for various values of the constants in these models. In the linear case, $w_0 = -1$ is fixed, with $0 < w_1 < 0.7$. The quadratic model is also fixed with $w_0 = -1$, and $w_1 = 0$ but with $0.1 < w_2 < 0.7$. The CPL parametrisation is for the range $w_0 = -1, 0 < w_a < 1$. Finally the 4-parameter model is specified with constant values of $w_0 = -1, w_f = -0.3$, with the two sets of curves corresponding to a fixed $\Delta = 0.1$ with changing $0.1 < z_t < 1$ (**light green curves**), and a fixed $z_t = 0.4$, $0.05 < \Delta < 0.2$ (**dark curves**) respectively. All models are plotted on the same scale on the y axis to illustrate the power of the models to describe different types of dynamics.

reconstruct more than around two parameters in any expansion. So the tension remains between models with enough flexibility to be accurate, and models that reflect the accuracy with which we are able to make measurements. Measurements of $w(z)$ (through measurements of the cosmic observables) at high redshift will hopefully help constrain the value of w through the long lever arm of such observations; and will provide insight into possible dynamics.

1.11.3 Scalar Fields as Dynamical Dark Energy

Scalar field models of dark energy naturally extend the cosmological constant Λ (which corresponds to a constant potential) to a dark energy model with redshift-dependent equation of state. See [80] for an extensive review of dynamical dark energy. We consider a scalar field ϕ rolling down its potential $V(\phi)$.

The dynamics of scalar fields are best described using the principle of least action. The general action is given as an integral over spacetime of the Lagrangian density which for scalar fields can be expressed as:

$$S = \int d^4x\sqrt{-g}\,[F(X) - V(\phi)]\,, \tag{1.47}$$

where $X = (\Box\phi)^2 = g^{\mu\nu}\partial_\mu\phi\partial_\nu\phi$, $g = \det g_{\mu\nu}$ is the determinant of the metric and $V(\phi)$ is the potential of the field ϕ. $F(X)$ is some general function of X, F differs for various scalar field models (for e.g. in k-essence F is a non-linear function of X). We consider the field to be minimally coupled to gravity [2], and so in this case the functional form for F is given by

$$F(X) = -\frac{1}{2}X = -\frac{1}{2}(\Box\phi)^2. \tag{1.48}$$

The energy momentum tensor of the field is obtained by varying the action given above in Eq. (1.47) in terms of the metric $g^{\mu\nu}$ (where $g = det(g_{\mu\nu})$), and is given by [80]:

$$\begin{aligned} T_{\mu\nu} &= -\frac{2}{\sqrt{-g}}\frac{\delta S}{\delta g^{\mu\nu}} \\ &= \nabla_\mu\phi\nabla_\nu\phi - g_{\mu\nu}\left[\frac{1}{2}g^{\alpha\beta}\nabla_\alpha\phi\nabla_\beta\phi + V(\phi)\right]. \end{aligned} \tag{1.49}$$

In order to derive the evolution equations for ϕ we vary the action in terms of ϕ. Under the assumption of a homogeneous scalar field, varying the action leads to the Klein-Gordon equation:

$$\ddot{\phi} + 3H\dot{\phi} + \frac{\mathrm{d}V}{\mathrm{d}\phi} = 0. \tag{1.50}$$

[2] This means that we can move easily from flat space to curved space, i.e. $\eta_{\mu\nu} \to g_{\mu\nu}$ and $\partial_\mu \to \nabla_\mu$.

We can then use Eq. 1.49 to obtain expressions for the energy and pressure of the scalar field. These are given by

$$\rho = \frac{1}{2}\dot{\phi}^2 + V(\phi), \quad p = \frac{1}{2}\dot{\phi}^2 - V(\phi) \tag{1.51}$$

Substituting Eqs. (1.51) into the Friedmann and Raychaudhri equations from Section 1.5.2, we derive similar equations for the scalar field, which are in turn given by

$$H^2 = \frac{8\pi G}{3}\left(\frac{1}{2}\dot{\phi}^2 + V(\phi)\right) \quad \text{and} \quad \frac{\ddot{a}}{a} = -\frac{8\pi G}{3}\left(\dot{\phi}^2 - V(\phi)\right). \tag{1.52}$$

Furthermore we define the equation of state for the field, w_ϕ by the ratio of pressure to density of the field

$$w_\phi = \frac{p}{\rho} = \frac{\dot{\phi}^2 - 2V(\phi)}{\dot{\phi}^2 + 2V(\phi)}. \tag{1.53}$$

A scalar field in a FLRW background is a perfect fluid, and so by integrating the continuity equation we obtain the energy density as a function of the dark energy equation of state for the field [80],

$$\rho(z) \propto \exp\left[3\int_0^z \frac{1 + w_\phi(z')}{1 + z'}\mathrm{d}z'\right], \tag{1.54}$$

which is given as $f(z)$ in Eq. (1.29)

In the context of acceleration, we introduce the slow-roll parameters:

$$\epsilon \equiv \frac{m_{\rm pl}^2}{16\pi}\left(\frac{V'}{V}\right)^2 \quad \eta \equiv \frac{m_{\rm pl}^2}{8\pi}\frac{V''}{V}, \tag{1.55}$$

where the prime $'$ denotes differentiation with respect to the field ϕ, or $V' = dV/\mathrm{d}\phi$. The conditions for slow-roll are that $\epsilon, |\eta| \ll 1$. One can equally define the slow-roll parameters in terms of the Hubble parameter and its derivatives [86]:

$$\widetilde{\epsilon} \equiv \frac{m_{\rm Pl}^2}{4\pi}\left[\frac{H'(\phi)}{H(\phi)}\right]^2 \quad \widetilde{\eta} \equiv \frac{m_{\rm Pl}^2}{4\pi}\frac{1}{H(\phi)}\frac{\mathrm{d}^2 H(\phi)}{\mathrm{d}\phi^2}, \tag{1.56}$$

where again the imposing slow-roll means the $\widetilde{\epsilon}, |\widetilde{\eta}| \ll 1$. During early stages of acceleration, none of these parameters need necessarily be small, since a large fraction of the energy density of the Universe ($\sim 30\%$) does not have negative pressure. Hence the coincidence problem described in Section 1.11.1 can be restated as why the slow-roll parameters are not small despite the acceleration of the Universe at late times [87].

Performing a Taylor series expansion of Eq. (1.53) in $\beta \equiv \dot{\phi}^2/V(\phi)$ yields:

$$w_\phi = \frac{\beta - 1}{\beta + 1} = -1 + 2\beta - 2\beta^2 + ... \tag{1.57}$$

Hence for small β, i.e. $\dot{\phi}^2 \ll V(\phi)$, (when the field is slowly rolling), the dark energy approaches a cosmological constant, $w \approx -1$.

Chapter 2

Early Universe Constraints on the Detectability of Dark Energy Dynamics

Figure 2.1: © Scott Adams, online at www.dilbert.com 18/10/2007

2.1 Introduction

Scaling quintessence models are physically well-motivated alternatives to the cosmological constant, Λ. After a review of scaling solutions, we show that imposing early universe constraints on the energy density of dark energy in these models strongly limits the deviation from ΛCDM at late times. The detectability of such models will hence be limited for the next decade until the DETF Stage IV experiments [60]. This work is published in [88].

2.2 Big Bang Nucleosynthesis and Dark Energy

Big Bang Nucleosynthesis (BBN) occurred shortly after the Big Bang. When the temperature of the Universe reached around 1 MeV, the abundances of the light elements, ^{3}He, ^{4}He, ^{6}Li, ^{7}Li, ^{1}H, ^{2}H $\equiv$ D, ^{3}H, ^{7}Be and ^{8}Be were set through a series of chemical reactions in the early Universe. We assume that the reader is reasonably familiar with the process of BBN, the details of which can be found in [14, 89, 90, 91, 92]. Big Bang Nucleosynthesis is sensitive to the amount of dark energy at early times, and hence the BBN measurements provide strong constraints on early dark energy [93].

At high temperatures ($T \gg$ MeV) the numbers of protons and the number of neutrons in the Universe are in equilibrium via the weak interactions [14, 89]:

$$n + \nu \leftrightarrows p + e^- \qquad n + e^+ \leftrightarrows p + \bar{\nu}, \tag{2.1}$$

where the symbols $n, \nu, \bar{\nu}, p, e^-, e^+$ denote the neutron, electron neutrino (and its anti-neutrino), the proton, electron and positron respectively.

The number of species i (where i indexes the particular species) is distributed according to the Boltzmann equation. In the non-linear regime this is given by [14]:

$$N_i \propto (m_i T)^{3/2} \exp\left(-\frac{m_i}{T}\right), \tag{2.2}$$

where T is the temperature of the reaction and m_i the species mass. Hence during equilibrium, the ratio of neutrons to protons is given by

$$\frac{n}{p} \approx \exp\left(-\frac{m_n - m_p}{T}\right), \tag{2.3}$$

where $m_n - m_p \simeq 1.29$ MeV is the difference in mass between the neutron and the proton. For temperatures around 1 MeV the number of protons is roughly equal to the number of neutrons, but that the ratio Eq. (2.3) tends to zero as the temperature decreases. The weak interaction rates drop rapidly, as $\Gamma \propto T^5$, and at a critical temperature, T_{crit}, the reactions go out of

equilibrium. At this temperature the ratio of neutrons to protons "freezes out", and remains essentially constant.

At early times the Universe is radiation-dominated, and therefore we neglect matter in the Hubble parameter, and Eq. (1.30) becomes

$$H(z) = H_0\sqrt{\Omega_{rad}T^4 + \Omega_{\rm DE}f(z)}. \tag{2.4}$$

The dark energy enters into the equation via $f(z)$, Eq. (1.29) in Section 1.7. Big Bang Nucleosynthesis is sensitive to the dark energy at early time in two key ways.

- **The temperature of freeze out**
  As mentioned above, the neutron to proton ratio is determined by T_{crit}, the temperature at which the reactions Eq. (2.1) go out of equilibrium. The interaction rate of Eq. (2.1) relative to the expansion of the Universe is [14]

  $$\frac{\Gamma}{H} \simeq \frac{G_F^2 T^5}{T^2/m_{\rm pl}} \simeq \left(\frac{T}{\rm MeV}\right)^3, \tag{2.5}$$

  where $G_F = 1.16637(1)\times 10^{-5}{\rm GeV}^{-2}$ is the Fermi constant and $H = \dot{a}/a$ is the Hubble rate in the early Universe given in Eq. (2.4). For temperatures below 1 MeV, the interaction rate Γ is lower than the expansion rate, and so the neutrino interactions are too weak to maintain equilibrium [14, 89]. The ratio n/p, Eq. (2.3), is exponentially sensitive to change in T_{crit}, and hence to the cosmology at BBN.

- **The age of the Universe**
  The formation of ^{4}He and the heavier elements requires deuterium D, which is formed through

  $$p + n \leftrightarrows D + \gamma. \tag{2.6}$$

  Deuterium is, however, only produced in significant amounts for temperatures below $T \approx 0.06$ MeV, otherwise it is destroyed by energetic photons [89]. This results in the deuterium bottleneck. During the time between freeze-out and significant deuterium production, the free neutrons begin to decay, with a half-life of $\tau_n = 885.7 \pm 0.8$s. Essentially all the free neutrons go into the production of D, and so the abundance of the elements is very sensitive to the time taken for the temperature to drop from 1 MeV to 0.06 MeV, given by

  $$t = \int_0^z \frac{1}{1+z}\frac{dz}{H(z)}. \tag{2.7}$$

  This is also then sensitive to the expansion of the Universe through $H(z)$.

Observations of the abundances of these light elements from the Lyman alpha absorption feature in high-redshift quasars (see [92, 91] and references therein) constrain the amount of primordial

deuterium, while measurements of the CMB [94, 6] put limits on the baryon density. Observations of low metallicity HII regions [95, 96] constrain the abundance of ^{4}He, while metal-poor stars constrain the abundances of ^{7}Li (see [96] for a set of references), although there is a significant tension between observed Li abundances and those predicted by BBN in a FLRW cosmology consistent with the WMAP data [97].

We have discussed how BBN is very sensitive to the amount of dark energy present in the early Universe. We now turn our attention to scaling models of dark energy in which the dark energy tracks the dominant energy components until it breaks away and begins to dominate at late times. These models will allow the constraint on dark energy at early times to carry through and constrain the detectability of such dark energy models at late times.

2.3 Scaling Models of Dark Energy

Scalar fields are ubiquitous in modern cosmology, and are popular partly due to the fact that they arise naturally in particle physics [80] (see [98] for a review of particle physics and cosmology), and so extend the cosmological constant to a model with dynamical dark energy. Scalar fields are introduced in Section 1.11.

As outlined in Section 1.11, the scalar field is specified by the form of its potential $V(\phi)$. One such model for the potential of the scalar field is the exponential potential,

$$V(\phi) = M^4 e^{-\lambda\kappa\phi}, \tag{2.8}$$

where M is a constant with dimensions of mass, λ is a dimensionless constant, $\kappa^2 = 8\pi G = 8\pi m_{\rm pl}^{-2}$ and $m_{\rm pl} = 1.22 \times 10^{19}$ GeV is the Planck mass. The energy density of the scalar field, ρ_ϕ is given by Eq. (1.51), and hence the critical energy density (again see Section 1 for details) is defined by $\Omega_\phi \equiv \kappa^2\rho_\phi/3H^2$.

The key characteristic of this potential is that is exhibits a scaling property, in that it scales with the background fluid, so that $w_\phi = w_b$, with $w_b = 0$ during matter domination and $w_b = 1/3$ during radiation domination. The energy density of the field remains constant and equal to the value

$$\Omega_\phi = \frac{3(1+w_b)}{\lambda^2}, \tag{2.9}$$

provided that $\lambda^2 > 3(w_b + 1)$.

The solution ϕ with energy density given by Eq. (2.9) is an *attractor solution* [99]. In the context of dynamical systems, this means that regardless of the initial value of the field, the field will converge to this solution. If the field starts from an initial value dominated by its kinetic energy (i.e. $V(\phi) \ll \dot{\phi}^2$), the equation of state of the field will be $w \approx 1$, and hence the energy density of the field will scale as $\rho \sim 1/a^6$, with then $\dot{\phi} \propto 1/a^3$ [100]. The kinetic energy density of the

field will drop as a^{-6} until it reaches the scaling solution. If Ω_ϕ is very small (i.e. much less than Eq. (2.9)), then the Hubble parameter will be dominated by background. This acts as a friction term in the dynamics of ϕ, and causes ϕ to drop more slowly than the background. Hence ϕ has an effective w greater than the background; as a result Ω_ϕ increases until it reaches the scaling solution.

The fact that the attractor solution exhibits scaling is an important result as it means that at early times (when the dark energy is sub-dominant during the matter and radiation epochs) the energy density of the field remains fixed at a constant value. We will show that this scaling property allows any constraints on the energy density at early times to be brought through to late times, until the field emerges from scaling and starts to dominate the energy density of the Universe.

The other attractor (when $\lambda^2 < 3(w_b+1)$) is a solution of late-time acceleration, when the energy density of the Universe is dominated by the scalar field, with $w_\phi = -1 + \lambda^2/3$ [101, 102, 80].

Since one of the attractor solutions of the system for the single exponential potential is scaling and another is dark energy domination, it makes sense to construct a potential that is a sum of the two exponentials [101]:

$$V(\phi) = M_1^4 e^{-\lambda\kappa\phi} + M_2^4 e^{-\mu\kappa\phi}, \tag{2.10}$$

with carefully chosen constants. In that way we construct a potential that results in scaling at early times and acceleration at late times. Here $\mu < \sqrt{2}$ ensures acceleration at late times, since for these values the potential resembles that of 'power-law' inflation [100, 99], with $a \simeq t^2/2$. Furthermore, the coefficients M_1 and M_2 are determined according to the model considered and the constraints on the present-day value of the scalar field energy density.

We define the upper bound on the density parameter of the scalar field by ϵ. BBN implies that $\Omega_{\rm DE}(T \sim 1 \text{ MeV}) < \epsilon$, with $\epsilon = 0.045$ at 2σ [93]. In order to carry forward these constraints on the energy density to late times, the field must be scaling by this time. If the field is not yet scaling at BBN, these constraints cannot be carried through to late times since we have no guarantee that the density did not grow a large amount before scaling began. However, it was shown that the field will in fact approach the attractor long before nucleosynthesis [99, 100], and so we can treat it as scaling at this time. In addition our results remain even if the field only starts to scale at the time of decoupling (around $z \sim 1000$), since similar or better constraints hold from analysis of the CMB [104, 105]. Hence the value of $\epsilon = 0.045$ is given as a conservative bound.

Scaling at early times implies that the upper bound $\Omega_{\rm DE}(z > z_{\rm t}) < \epsilon = 0.045$ for all redshifts greater than $z_{\rm t}$, the redshift at which the equation of state stops scaling. Hence we investigate the detectability of a model in which the field exhibits scaling with the background fluids until some transition redshift z_t when the field begins to dominate the energy density of the Universe. We give a specific parametrisation of a such a model in Section 2.5.

2.4 General Scaling Constraints on the Energy Density of Dark Energy

Given the upper bound on the density parameter of the scalar field from BBN, $\Omega_{\rm DE}(z_{\rm BBN}) < \epsilon \equiv 0.045$ [93] for scaling models of dark energy, we give model-independent constraints on the background cosmological observables $H(z)$ and the distance modulus $\mu(z)$, as defined in Chapter 1 for all such scaling models.

The density parameter (see Chapter 1) of the dark energy (where we neglect the contribution from radiation) is defined as the ratio of the dark energy density to the critical density, or

$$\Omega_{\rm DE}(z) = \frac{\Omega_{\rm DE} f(z)}{\Omega_{\rm DE} f(z) + \Omega_m (1+z)^3}, \tag{2.11}$$

where $f(z)$ describes the redshift dependence of the dark energy density as given in Eq. (1.29).

Beyond the redshift where the scaling ends the energy density of the dark energy is constant (i.e. $\Omega_{\rm DE}(z \geq z_t)$ is constant in perfectly scaling models). Hence the constraint from early times implies that $\Omega_{\rm DE}(z \geq z_t) < \epsilon$.

When the field is in the matter dominated epoch (and scaling) it tracks the background as $w(z) = 0$, for $z > z_t$. This constraint coupled to the constraint on the density parameter limits the form of f, as

$$f(z \geq z_t) = \frac{\epsilon(1+z)^3}{r(1-\epsilon)} = \frac{0.047}{r}(1+z)^3 \tag{2.12}$$

where $r = \Omega_{\rm DE}/\Omega_{\rm m} \approx 7/3$ is evaluated today, and we have substituted in the value for ϵ from Bean *et al.* [93].

We illustrate the constraint on $\Omega_{\rm DE}(z)$ in Figure 2.2, for various models of the dark energy density. The constraint that $\Omega_{\rm DE}(z) \to 0.7$ as $z \to 0$ is imposed on the solutions. We see that for $z > z_t$, the value of $\Omega_{\rm DE}$ is scaling and is fixed at ϵ, the early Universe limit.

Clearly this constraint on the energy density implies a constraint on the cosmological observables, like the Hubble parameter and distance measures. Starting with the Hubble parameter, the general constraint on $H(z)$ in the scaling regime is:

$$\frac{H_{\rm DE}}{H_\Lambda}(z \geq z_t) = \sqrt{\frac{(1+z_t)^3}{(1-\epsilon)((1+z_t)^3 + r)}} \tag{2.13}$$

Given that $r = \Omega_{\rm DE}/\Omega_m$ is Eq. (2.13) is maximised at $r = 0$, and hence we establish a strong model-independent upper bound

$$\frac{H_{\rm DE}}{H_\Lambda}(z \geq z_t) \leq \sqrt{\frac{1}{1-\epsilon}} = 1.023, \tag{2.14}$$

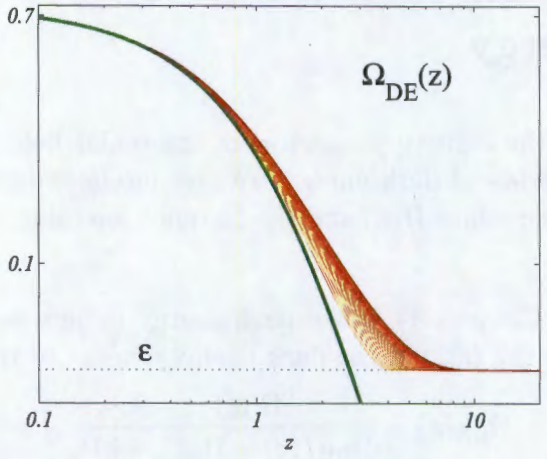

Figure 2.2: **Evolution of $\Omega_{\mathrm{DE}}(z)$** for the scaling model parameterised by the polynomial parametrisation of $w(z)$, Eq. (2.17). The approach to the BBN limit $\epsilon = \Omega_{\mathrm{DE}}(z = z_{\mathrm{BBN}}) = 0.045$ (**dashed line**) can be seen for $z \to \infty$. The curves are plotted for a range of coefficients in the models, from $z_t = 4$ (**light orange**) to $z_t = 10$ (**dark red**). For comparison we also show the curve for ΛCDM (**green curve**), where the energy density drops to zero before $z = 2$. Figure 2.4 shows the corresponding observational quantities for these scaling quintessence models.

where the numerical value is obtained by substituting in the value for ϵ from [93].

This limit can be seen in the left panel of Fig. 2.4, where the Hubble parameter for all models tends towards this limit for $z > z_t$. This has strong implications for detecting deviations from ΛCDM at high redshift, since the limit above means that any such deviations are bound to be less than 2.3%. It is important to note that this limit only applied for $z > z_t$. To derive constraints on the Hubble parameter for redshifts $0 < z < z_t$, we will need to parameterise a specific form for $w(z)$. One such parametrisation is given in Section 2.5.

The distance modulus, given by $\mu(z)$ is constrained in a similar manner. Once again, the interesting quantity is the deviation from ΛCDM, as this indicates how likely they are to be distinguishable from a cosmological constant model with no evolution in the dark energy. Hence the quantity $\Delta\mu \equiv \mu_{\mathrm{DE}}(z) - \mu_{\Lambda}(z)$ is given by:

$$\Delta\mu = 5\log_{10}\left(\frac{d_{L,\mathrm{DE}}(z)}{d_{L,\Lambda}(z)}\right) \tag{2.15}$$

where $d_L(z)$ is the luminosity distance for the given model ($\mu(z)$ is defined in Eq. (1.38), see Section 1.7 for a summary of the observables).

Assume that there exists a number α such that $H(z)/H_{\Lambda}(z) \leq 1 + \alpha^2$ for all z. For example the constraint on the energy density constraint discussed above, i.e. $\Omega_{\mathrm{DE}}(z \geq z_t) < 0.045$, yields

the constraint on H that $\alpha^2 \simeq 2.3\%$. Since d_L involves integrals over $1/H(z)$, the constraint propagates through as $d_{L,\mathrm{DE}}(z)/d_{L,\Lambda}(z) \geq (1+\alpha^2)^{-1}$. Hence $\Delta\mu(z)$ obeys the inequality

$$0 \geq \Delta\mu(z) \geq -5\log_{10}(1+\alpha^2). \tag{2.16}$$

A bound of $\alpha^2 = 0.025$ gives $|\Delta\mu(z)| \leq 0.054$ mag. This is visible as the limit on $\Delta\mu(z)$ in Fig. 2.4. Propagating the limit on H using ϵ will impose an even stronger constraint, since $z \geq z_t$, $\alpha^2 \leq \epsilon/2$. Again it is worth noting that these general results do not constrain $H(z < z_t)$, which instead requires a specific model for $w(z)$. We now turn to one such parametrisation.

2.5 Late-time Evolution of the Models

The models of interest must satisfy scaling until some redshift, z_t, and then yield late-time acceleration. In order to achieve this, we need to parameterise our models once the field exits the scaling regime. The double exponential potential [101, 102] as outlined in Section 2.3 achieves such late-time acceleration for carefully chosen values of the constants. Models of this form were considered in [88], although we do not discuss the detectability of such models here. Instead we focus our attention on the $w(z)$ models parameterised by a polynomial in redshift.

2.5.1 Polynomial parametrisation of w(z)

We consider a quadratic parametrisation of the dark energy equation of state, $w(z)$ [106], that exits the scaling regime at z_t. It is given by

$$w(z) = \begin{cases} w_0 + w_1 z + w_2 z^2 & \text{for } z < z_t \\ 0 & \text{for } z \geq z_t \end{cases} \tag{2.17}$$

We are interested here in describing minimally coupled scalar fields with canonical kinetic terms. In other words they satisfy the constraints in Eq. (1.48).

In general we consider the case where $w_0 = -1, w_2 \neq 0$. We force continuity in the equation of state at the boundary between scaling and dark energy domination, i.e. at $z = z_t$, which implies

$$w_2 = \frac{1}{z_t^2} - \frac{w_1}{z_t}. \tag{2.18}$$

The BBN constraint provides w_1 in terms of z_t, and we are left with a family of curves that satisfy the early Universe constraints and the bounds on the energy density today. We have set $w(z=0) = -1, \Omega_{\mathrm{DE}}(z=0) = 0.7$.

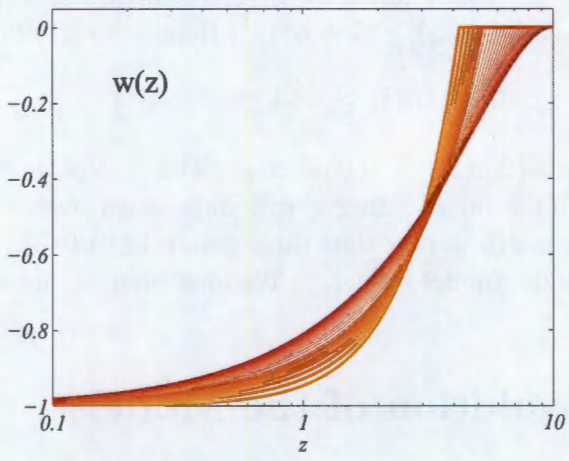

Figure 2.3: **Late-time parametrisation of scaling dark energy.** The polynomial parametrisation $w(z)$ given as Equation (2.17) for z_t from 4 (**light orange**) to 10 (**dark red**). The models are fixed at $w(z=0) = -1$. The density parameter for these models, $\Omega_{\rm DE}(z)$ is shown in Figure 2.2, and the observables for this parametrisation are given in Figure 2.4.

Figure 2.3 shows this polynomial parametrisation for various values of the redshift z_t, in the range $4 < z_t < 10$, with the lower bound of this range was chosen to ensure that we are describing a minimally coupled canonical scalar field, so $w(z) \geq -1 \ \forall \ z$.

The observables from this family of $w(z)$ curves are shown in Fig. 2.4. We note that for $z \leq 1$ the BBN constraint is so strong that all models have $w(z) < -0.8$, as shown in Fig. 2.4, and the density parameter for these models is shown in Fig. 2.2. The largest deviation of $H(z)$ from the ΛCDM comparison model is about 2.7% with the largest deviation in the distance modulus only about 0.03 magnitudes (occurring at $z = 2$).

This shows that if $w \simeq -1$ today we cannot expect significant deviations from ΛCDM at any redshift and only Dark Energy Task Force (DETF) Stage-IV experiments [60] are likely to detect dark energy dynamics with any real significance. However while current data favour $w(0) \simeq -1$, they are consistent with larger values, such as $w(0) < -0.86$ [6, 39]. This might give some hope to the detection of dynamics in models with larger values of w today.

2.6 Conclusions

Scaling models are physically well-motivated alternatives to the cosmological constant. We have reviewed the basic definition of scaling models, where the energy density of the field is constant

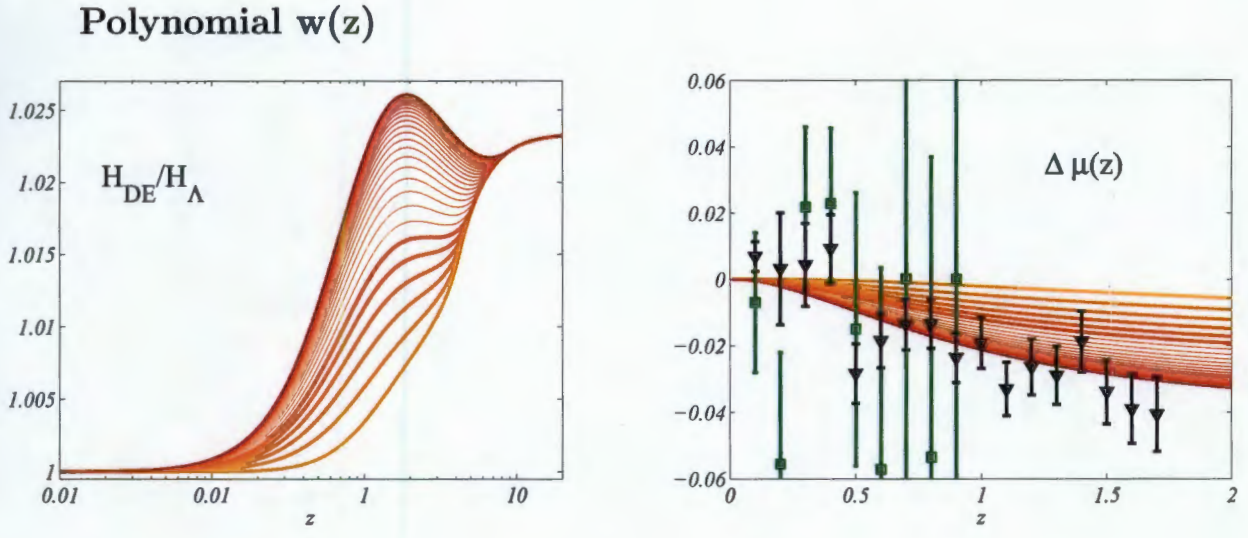

Figure 2.4: **Observables from the polynomial parametrisation:** allowed observables for the polynomial $w(z)$ (shown in Figure 2.3) showing the small deviations from the ΛCDM predictions. All models have $|dw/dz(0)| < 0.2$. For $w(0) < -0.9$ (the thicker lines) $H_{\rm DE}(z)$ deviates from $H_\Lambda(z)$ by at most 2.7%, and implies a deviation in distance modulus of less than 0.05 mag. The error bars in the right panels correspond to the Stage-III (large boxed errors) and Stage-IV (small triangular errors) supernova surveys respectively. These are produced for the bottom curve in each case.

during scaling as its equation of state tracks the background. These scaling properties allow us to propagate the constraint on early dark energy through to late times. In so doing, we have shown that the constraint $\Omega_{\rm DE} < \epsilon$ on the energy density of the scalar field at the time of Big Bang Nucleosynthesis (and similarly for decoupling) strongly limit the allowed dynamics at late times. We discussed the general constraints on the observables from scaling models of dark energy for $z > z_t$, and have investigated one particular scaling model at low redshift.

We have explicitly assumed, however, that one excludes phantom behaviour of w, in that we have forced $w \geq -1$ in all cases. Hence unless we allow much more freedom in our choice of w, and if it is not close to the maximum value allowed by current data, then we have shown that the detection of dynamical models of dark energy will likely have to wait a decade for the Stage-IV DETF [60] experiments. We should not then let the non-detection of dark energy dynamics discourage us from searching for dynamical alternatives to the current 'flavour of the month' cosmology.

Chapter 3

Fisher Analysis and Flex corrections

Figure 3.1: © Joe Sayers, online at www.jsayers.com/thingpart 08/06/2005

3.1 Introduction

This section reviews and extends the Fisher Matrix formalism. We calculate non-Gaussian corrections to the likelihood which we call the Fisher Flex corrections. We introduce the Fisher Flex test as a test of whether the assumption of Gaussianity in the standard Fisher Matrix formalism will produce biased constraints on cosmological parameters. This original research is in preparation for publication [107].

3.1.1 Bayesian Statistics

The physical interpretation of statistics is a topic of much debate. This debate is particularly relevant in terms of two opposing statistical frameworks, namely the frequentist and Bayesian approaches. Briefly stated, the frequentist interpretation of probability is that the probability of a given event A is the ratio of the number of times the event occurs in a large number of trials,

$$P_A = \lim_{N\to\infty} \frac{N_A}{N}, \tag{3.1}$$

where N_A is the number of times event A occurs. This school of thought is characterised by the objectivity of the observer when defining the probability. The intuition or understanding of the observer is not important in this case. This approach is criticized by those in favour of evidential or Bayesian probability, which defines probability as a measure of the state of knowledge [108]. Here the notion of prior knowledge affects the probability of an event. We will not debate the merits of the two methods here, but will use Bayesian theory from here onwards.

Firstly, the conditional probability of event A given event B is defined as $P(A|B)$, which is the probability that event A will occur given that B occurs. The posterior probability, $P(T|D)$, is the probability of a theory or model T given the data D we observe. This is something which we do not know *a priori*. Bayes' theorem, however allows one to write the posterior in terms of the likelihood, which is the probability of the data assuming a certain model, as follows:

$$P(T|D) = P(D|T)\frac{P(T)}{P(D)}, \tag{3.2}$$

where $P(D|T)$ is the likelihood of the data given the assumed model, $P(T)$ is the prior on the theoretical model, and encodes any knowledge on the validity model, and $P(D)$ is the Bayesian evidence, which is generally treated as an arbitrary normalisation factor.

Bayes' theorem is used to determine the values of the parameters that are most likely to be correct. In other words, the best-fit parameters are those that maximise the posterior, Eq. (3.2). Since the evidence is treated as normalisation, and the prior is input, maximising the posterior is achieved by maximising the likelihood, $P(D|T)$, which is

$$\mathscr{L} = P(D|T). \tag{3.3}$$

We are interested in the both the maximum likelihood parameters and their corresponding errors. For a random variable X distributed according to a Gaussian function with mean μ, then the 1σ error (the standard deviation) is defined to be such that $|x-\mu| < \sigma$ with 68% probability. These errors are a measure of the curvature of the likelihood, since values close to the mean value (the parameter value that yields the maximum value of the likelihood) indicate a very steep likelihood surface, whereas wide errors mean that the likelihood is very flat in terms of those parameters. In terms of a general likelihood of parameters, $\mathscr{L}$ one could use percentiles to determine the values of the $1\sigma, 2\sigma$ errors. Under the assumption of Gaussianity, however, the Fisher Matrix allows us to estimate exactly the curvature of the likelihood surface, and hence determines the error on the maximum likelihood parameter values.

3.1.2 Fisher Information Theory

Fisher Information Theory is a powerful statistical tool used in many fields, and has gained popularity in astronomy and cosmology in recent years. It describes how much information a measurement of a particular observable quantity will give you about parameters in an underlying model. More precisely, if we denote the vector of observables $\vec{X} = (X_1, X_2, ..., X_i, ..., X_n)$, where i labels the specific observables, then the Fisher Information Matrix or Fisher Matrix (FM) quantifies how much information these observables contain about the parameters $\vec{\theta} = (\theta_1, \theta_2, ..., \theta_j, ..., \theta_m)$ in the model.

A key point in Fisher analysis is that the Fisher Matrix treatment allows one to compute the errors on these parameters $\vec{\theta}$, around a given input model $\vec{\theta}^*$. In other words, assuming a given model and fiducial values of the parameters in that model, the FM then allows you to estimate how well you would be able to constrain those parameters from observations.

In general the Fisher Matrix is given in terms of the likelihood function $\mathscr{L}(\vec{\theta}) = f(\vec{X}; \vec{\theta})$, via the expectation value of the derivatives of the log of the likelihood with respect to the parameters $\vec{\theta}$, or

$$F_{AB} = -\left\langle \frac{\partial^2 \ln \mathscr{L}}{\partial\theta_A \partial\theta_B} \right\rangle, \tag{3.4}$$

where the angle brackets indicate the expectation value of derivatives. It is worth noting that for a random variable X with probability density $f_X(x)$, the expectation value any arbitrary function $g(x)$ is defined to be

$$\langle g(X) \rangle = \int_{-\infty}^{\infty} g(x) f_X(x) dx. \tag{3.5}$$

If the likelihood (Eq. 3.3)) can be written as $\mathscr{L} \propto \exp(-\chi^2/2)$ where $\chi^2 = -(\mathbf{d}-\mathbf{t})^{\mathrm{T}}\mathbf{C}^{-1}(\mathbf{d}-\mathbf{t})/2$ is the usual chi-squared statistic relating the theory $\mathbf{t}$ to the data $\mathbf{d}$ and $\mathbf{C}$, (the data covariance

matrix which is a measure of how the data are correlated), then Eq. (3.4) can be expressed instead in terms of a sum over derivatives of the observed quantities as:

$$F_{AB} = \frac{\partial X}{\partial \theta_A}^{\mathrm{T}} C^{-1} \frac{\partial X}{\partial \theta_B} + \frac{1}{2} \mathrm{Tr}\left(C^{-1} \frac{\partial C}{\partial \theta_A} C^{-1} \frac{\partial C}{\partial \theta_B} \right), \tag{3.6}$$

The X_i's in Eq. (3.6) are the observables, and $\overrightarrow{\theta}$ the vector of parameters in the model. $\frac{\partial C}{\partial \theta_j}$ is the derivative of the covariance matrix with respect to the parameter θ_j, which measures how the covariance of the data depends on the assumed model and parameter values. In most cosmological applications of Fisher Matrix theory, it is assumed that the errors are only weakly dependent on cosmological parameters, and so this second term in the expression for the Fisher Matrix can be ignored.

In the case when the data are uncorrelated, then the covariance matrix $\mathbf{C}$ is diagonal, $C_{ij} = \mathrm{diag}[\sigma_1^2, ...\sigma_n^2]$ and Eq. (3.6) then reduces to the simple equation

$$F_{AB} = \sum_i^N \frac{1}{\sigma_{X,i}^2} \left[\frac{\partial X}{\partial \theta_A} \frac{\partial X}{\partial \theta_B} \right]\Bigg|_i, \tag{3.7}$$

where the sum over $i = 1 : N$ is a sum over data points in your data set.

The inverse of the Fisher Matrix corresponds to the error covariance matrix, and so we can convert from the Fisher Matrix F_{AB} to errors on particular parameters. The Cramér-Rao bound states that the variance of any unbiased estimator, or one whose expectation value is equal to the true value of the parameter, is at least as high as the inverse of the Fisher information [109]. In one dimension this means that the errors on the parameter are always larger than the square root of the diagonal component of the inverse of F, or $\Delta\theta_A \geq (F^{-1/2})_{AA}$. In other words the bound states that the errors from Fisher analysis are lower bounds for the error on parameters.

3.1.3 Marginalisation

In general we consider a likelihood in terms of N parameters (i.e. an N-dimensional likelihood). We are, however, often interested in only certain n parameters, and so we want to marginalise over the other m 'nuisance' parameters. For example, the likelihood $P(\theta_i)$ for parameter θ_i, is obtained from the full likelihood by marginalising over the other $\theta_j, j \neq i$ as follows:

$$P(\theta_i) = \int_{-\infty}^{\infty} P(\theta_1, .., \theta_i, .., \theta_N) d\theta_1 d\theta_2 ... d\theta_{i-1} d\theta_{i+1} ... d\theta_N. \tag{3.8}$$

This marginalisation is simple in terms of the Fisher Matrix formalism, if we write the full Fisher

Matrix in terms of sub-matrices, as

$$F = \begin{pmatrix} A & B \\ B^{\mathrm{T}} & C \end{pmatrix} \tag{3.9}$$

where A is the $n \times n$ sub-matrix for the parameters of interest, B is a $n \times m$ matrix and C and $m \times m$ matrix. The marginalised matrix of interest then is given by [110] as

$$\widetilde{F} = A - BC^{-1}B^{\mathrm{T}}, \tag{3.10}$$

where the first term is the matrix of the reduced parameter space and the second term encodes the effects of the marginalisation over the other parameters. This can be linked to the formulation in terms of integration (Eq. (3.8)) if we express the multi-dimensional integral in terms of the n parameters of interest and the m nuisance parameters, as

$$\int \exp\left(A + 2B_i x^i + C_{ij} x^i x^j\right) d^m x, \tag{3.11}$$

where x is the set of m nuisance parameters. Since we are integrating over these nuisance parameters, the matrix A is just a constant with respect to these parameters. Then Eq. (3.11) can be expressed as

$$\int \exp\left(A + 2B_i x^i + C_{ij} x^i x^j\right) d^m x = \sqrt{-\frac{\pi}{\det C}} \exp\left(A - BC^{-1}B^{\mathrm{T}}\right). \tag{3.12}$$

Since the overall normalisation factor is not relevant, we note then that the term in the exponent of Eq. (3.12) is nothing but the marginalised matrix $\widetilde{F}$ given by Eq. (3.10), and so we have shown how integration over the parameters that are not of interest is equivalent to marginalisation via the matrix manipulation technique described above.

Equivalently, one could invert the original Fisher Matrix F, form a $n \times n$ matrix consisting of the rows and columns of the n parameters of interest, and then invert this sub-matrix to get $\widetilde{F}$ [33]. In the two dimensional case, we can then define an error ellipse in the two parameters at a given significance level α by the matrix equation

$$\overrightarrow{\Delta\theta}^{\mathrm{T}} \widetilde{F} \overrightarrow{\Delta\theta} = \alpha. \tag{3.13}$$

3.2 Fisher Matrix Techniques in Cosmology

As an example of how Fisher Matrix ellipses give us intuition about the feasibility of our model, consider Figure 3.2. The 1σ error ellipse is generated (using the code Fisher4Cast [107, 111] developed with fellow students at the University of Cape Town) around the fiducial ΛCDM model with the coefficients in the CPL [82, 83] parametrisation $(w_0, w_a) = (-1, 0)$. Models with values of w_0, w_a taken from inside this ellipse are not distinguishable from the fiducial model at

the 1σ confidence level. However, a model with parameters taken from outside this 1σ contour is clearly distinguishable from the fiducial model at the 1σ level. Hence the Fisher Matrix allows us to determine which models will be discernible from the assumed cosmological model at various confidence levels.

Parameter	**Value**
Redshift	$z = 0.1 : 0.1 : 2$
Observables	**Percentage error**
H(z)	$\sigma_H = 1\%$ at each z_i
$d_A(z)$	$\sigma_{d_A} = 1\%$ at each z_i
$G(z)$	$\sigma_G = 1\%$ at each z_i
Cosmological model	**Values**
$(H_0, \Omega_m, \Omega_k, w_0, w_a)$	$(70\text{kms}^{-1}\text{Mpc}^{-1}, 0.3, 1 \times 10^{-10}, -1, 0)$
Priors on model	$(1 \times 10^4, 1 \times 10^4, 1 \times 10^4, 0, 0)$

Table 3.1: Survey data to investigate the affect of curvature on or knowledge of dark energy. Taken from [112] .

FMs are also used to predict the sensitivity of future surveys and to evaluate how expected errors on future measurements (data) map onto the space of errors on inferred cosmological parameters of interest. In designing future experiments, we are interested in studying how the experiments will constrain cosmological parameters in our model. This can of course be done by simulating data for a particular experiment from a specific cosmological model, and then running the simulated data through the data reduction pipelines to 'reconstruct' the input cosmology. However, such techniques are computationally very costly, especially when sampling over a very large multi-dimensional parameter space. The Fisher Matrix, however is a much faster way to derive such constraints, and so Fisher matrices are optimally used for things like telescope (and survey) design in astrophysics and cosmology.

As a particular example of Fisher Matrix projections in the literature, Figure 3.3 shows projected errors from the forthcoming Large Synoptic Survey Telescope [53, 62], which will detect up to 200 000 SNe Ia per year. Zhan *et al.* [113] propose not only to use these SNe to measure the luminosity distance but to use the large numbers of SNe ($\sim$ 20000) SNe Ia as tracers to measure the BAO as well (the luminosity and angular diameter distances are given in Eq. 1.35 of Section 1.7). Figure 3.3 shows the projected constraints on the dark energy parameters from this experiment. Note the effect of including a prior on the parameters from the Planck satellite [114] (see Section 3.1.1 for a discussion on prior matrices.) An extensive review of Fisher matrices applied to cosmology can be found in [109].

Figure 3.4 (which is Figure 7 from [110]), shows projected 1σ error ellipses from a 5-dimensional likelihood for a projected redshift survey of the baryon acoustic oscillations (BAO). The ellipses are plotted for different ranges in redshift, with the projected ellipse from the combined survey

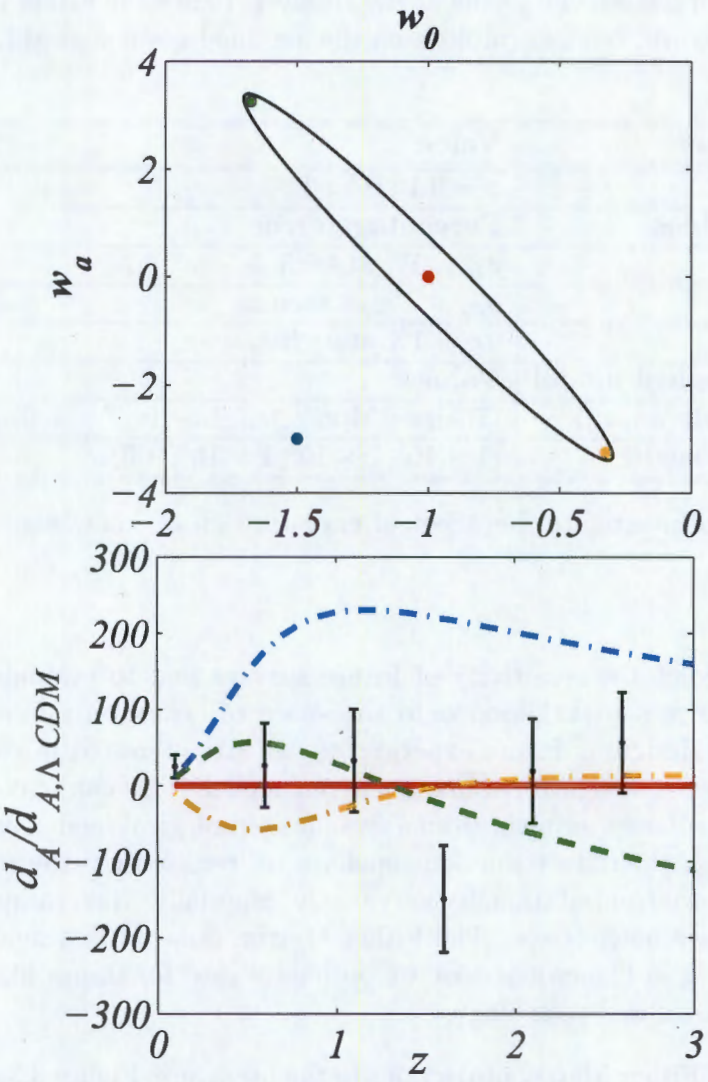

Figure 3.2: **The link between parameter space and model likelihood.** This schematic plot shows the an error ellipse for a given survey **(top panel)** and the models of the angular diameter distance corresponding to those models **(bottom panel)**. The details of the survey are given in Table 3.1. Models for the angular diameter distance $d_A(z)$ generated using parameters within the 1σ ellipse (the **green** and **yellow** points) are not distinguishable from the assumed model - which is plotted as the red curve with the errors for the survey. However, once outside this ellipse (the **blue** point), we see that the corresponding models are distinguishable from the data at 68% confidence. The 1σ error ellipse is plotted using the Fisher4Cast code [107, 111].

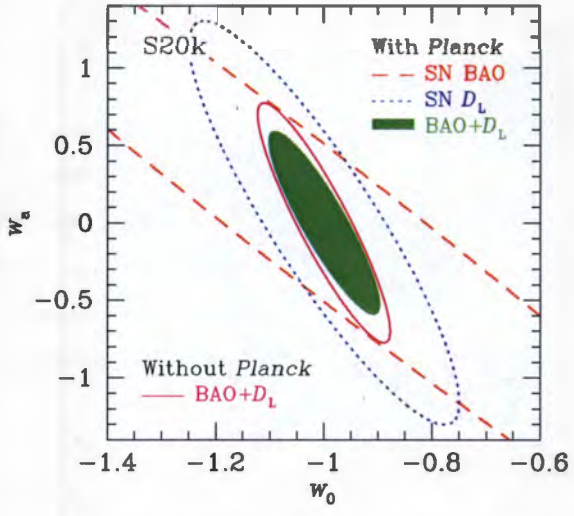

Figure 3.3: **LSST survey projections.** Constraints on the coefficients in the CPL parametrisation [82, 83] from measurements of the BAO from 20 000 SNe Ia (**red dashed line**) are shown with the luminosity distance constraints (**blue dotted line**), which is Figure 3 in [113]. Combining information from both probes yields tighter constraints, as shown by the **green filled ellipse**. The constraints are slightly changed without the inclusion of the Planck prior.

shown as the small central ellipse. This illustrates the power of combining information from many redshifts in surveys to measure the baryon acoustic oscillations.

In order to evaluate the power of a given survey, Figures of Merit (FoMs) can be defined using, among others, the error ellipse in the parameter plane that results from the Fisher Matrix through Eq (3.13). Examples of such FoMs can be found in [60, 115, 116]. This idea of a Figure of Merit will be useful when investigating the affect of cosmic curvature on the precision of our knowledge of dark energy, which will be discussed in Chapter 4.

We give examples of the formalism outlined out in the previous section in a cosmological context. In this context the observables are given by the Hubble parameter or the distance modulus for example (these are introduced in Section 1.7). The vector of cosmological parameters in our model, $\vec{\theta}$, (assuming a FLRW cosmology) consists of H_0, the value of the Hubble parameter today, Ω_m, the critical energy density of the matter content of the Universe today, Ω_k, the density of the curvature of the Universe and the coefficients w_0, w_a in the CPL [82, 83] parametrisation of the dark energy equation of state, $w(z)$. In the following sections we give examples of the Fisher derivatives of the Hubble parameter as a function of the parameters $\vec{\theta}$. To illustrate the model dependence of the Fisher derivatives, we also compute them for a different model of the dynamical equation of state $w(z)$.

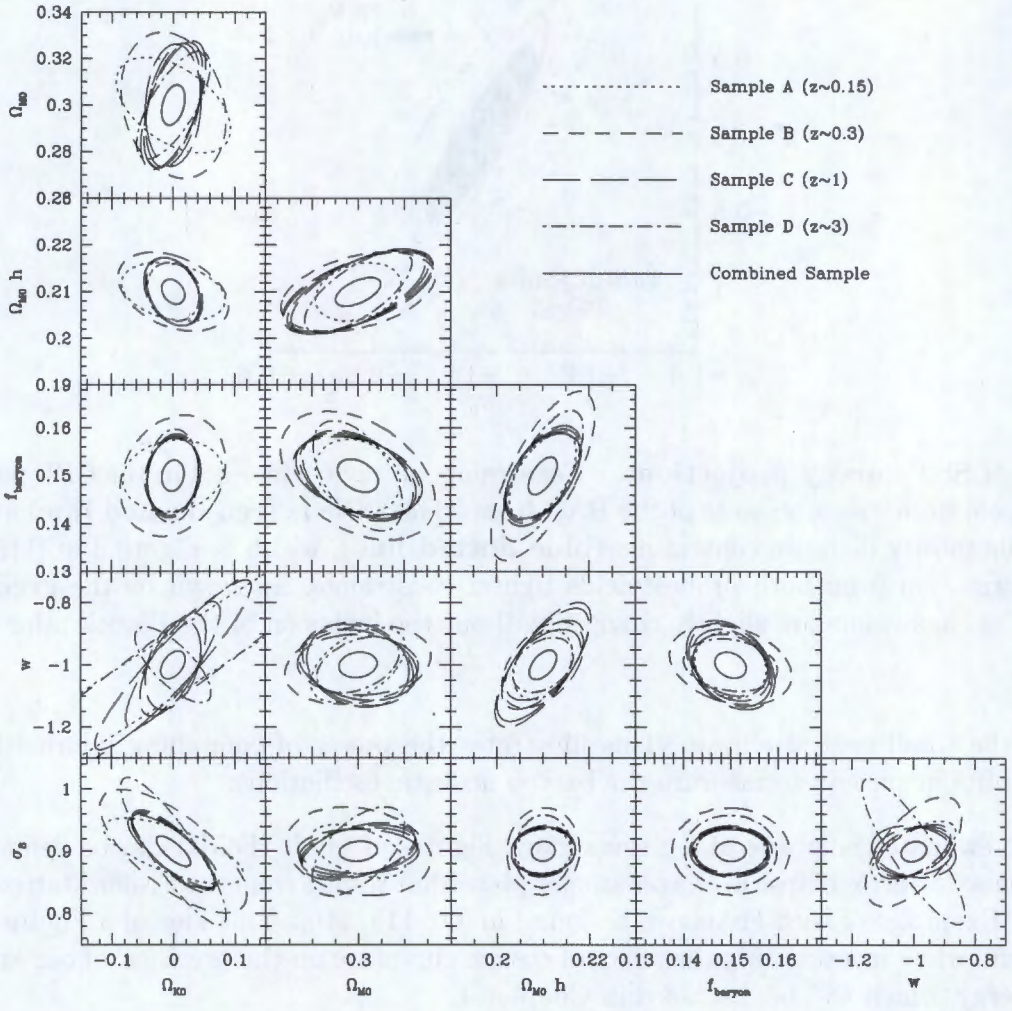

Figure 3.4: **Projected error ellipses for a galaxy redshift survey**. The ellipses for a survey to measure the BAO using different tracers at different redshifts, taken from [110], where it is Figure 7. The **dotted** lines show the contours from a volume limited survey of $M_r \sim -22$ galaxies, while survey B (**short-dashed line**) is for a survey of luminous red galaxies at low redshift. The **long-dashed** lines are for surveys of giant ellipticals or star forming galaxies over a redshift range ($0.5 < z < 1.3$), and survey D is a high-redshift sample of Lyman break galaxies (**dot-dashed line**). Combining information from the various sample greatly increases the expected accuracy on the dark energy parameters of the CPL [82, 83] parametrisation, as can be seen from the solid central ellipse.

3.3 Example of Fisher Derivatives

3.3.1 The Hubble Parameter

As introduced in Section 1.7, the expansion history of the Universe is described by the Hubble parameter (Eq. (1.30). The parametrisation for dark energy enters the Hubble in the form of the evolution of the energy density of the dark energy, or Eq. (1.29). Assuming the CPL parametrisation, given as $w(z) = w_0 + w_a z/1 + z$ (Eq. (1.45) in Section 1.11.2) we can write $f(z)$ as

$$f(z) = (1+z)^{3(1+w_0+w_a)} \exp\left\{-3w_a \frac{z}{1+z}\right\}. \tag{3.14}$$

In contrast for the dark energy model $w(z) = w_0 + w_1 z$ (given as Eq. (1.43)) which is used in many analyses [81, 117, 118], $f(z)$ becomes

$$f(z) = (1+z)^{3(1+w_0-w_1)} \exp\left(3w_1 z\right). \tag{3.15}$$

Assuming a FLRW background and the equations for the Hubble parameter in this model, we can compute the Fisher derivatives with respect to the 3 general cosmological parameters, H_0, Ω_m, Ω_k, and the parameters for the assumed model of dark energy. We give the derivatives in terms of the w_0, w_a in the CPL parametrisation, and w_1, w_2 in the linear parametrisation of $w(z)$.

- H_0

  As the Hubble constant, H_0 only appears as a multiplicative term, the Fisher derivative of $H(z)$ with respect to the Hubble constant H_0 is simple and yields:

  $$\frac{\partial H}{\partial H_0} = E(z), \tag{3.16}$$

  where $E(z)$ is the function defined in Section 1.7.

- The matter density Ω_m

  The matter density only enters $H(z)$ through $E(z)$, and hence we use the chain rule to determine the derivatives:

  $$\frac{\partial H}{\partial \Omega_m} = H_0 \frac{1}{2E}\left\{(1+z)^3 - f(z)\right\}. \tag{3.17}$$

- Curvature Ω_k

  gain curvature only occurs in $E(z)$, yielding:

  $$\frac{\partial H}{\partial \Omega_k} = H_0 \frac{1}{2E}\left\{(1+z)^2 - f(z)\right\} \tag{3.18}$$

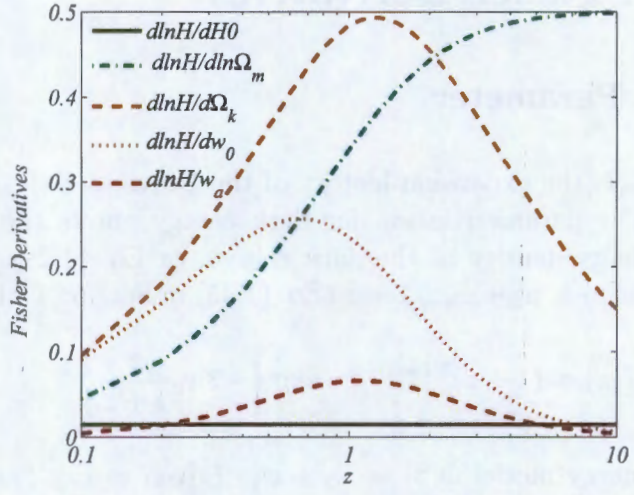

Figure 3.5: **Fisher Derivatives for the Hubble parameter.** The derivatives are given for H_0 **(solid olive line)**, $\ln\Omega_m$ **(dot-dashed green line)**, Ω_k **(dashed light brown line)**, w_0 **(dotted brown line)** and w_a **(dashed dark brown line)**. This figure was produced using Fisher4Cast [107, 111].

- Equation of state parametrisations

  Firstly we take Fisher derivatives with respect to the specific parameters of the CPL [82, 83] given in Eq. (1.45).

  – *The coefficient w_0*

  The derivatives with respect to $H(z)$ decompose into derivatives with respect to $f(z)$, the evolution of the energy density of the dark energy as:

$$\frac{\partial H}{\partial w_0} = \frac{H_0}{2E}\left\{(1-\Omega_m-\Omega_k)\frac{\partial f(z)}{\partial w_0}\right\} \tag{3.19}$$

  where we define

$$\begin{aligned}\frac{\partial f}{\partial w_0} &= (1+z)^{3(1+w_0+w_a)}\ln(1+z)3\exp\left\{-3w_a\frac{z}{1+z}\right\} \\ &= 3f(z)\ln(1+z).\end{aligned} \tag{3.20}$$

  – *The coefficient w_a*

  Similarly the derivatives with respect to w_a are given by

$$\frac{\partial H}{\partial w_a} = \frac{H_0}{2E}(1-\Omega_m-\Omega_k)\frac{\partial f(z)}{\partial w_a}, \tag{3.21}$$

where again the partial derivative with respect to $f(z)$ is

$$\frac{\partial f(z)}{\partial w_a} = 3f(z)\left(\ln(1+z) - \frac{z}{1+z}\right). \tag{3.22}$$

The derivatives in terms of the coefficients in the linear parametrisation of $w(z)$ are different only in that the $\partial f/\partial w_i$ derivatives change for the parametrisation, namely

- *The coefficient* w_1

$$\begin{aligned}\frac{\partial f}{\partial w_1} &= (1+z)^{3(1+w_1-w_2)}\ln(1+z)3\exp\{3w_2 z\} \\ &= 3f(z)\ln(1+z).\end{aligned} \tag{3.23}$$

- *The coefficient* w_2

$$\begin{aligned}\frac{\partial f}{\partial w_1} &= -3\ln(1+z)(1+z)^{3(1+w_1-w_2)}\exp\{3w_2 z\} + (1+z)^{3(1+w_1-w_2)}3z \\ &= 3f(z)(z-\ln(1+z)).\end{aligned} \tag{3.24}$$

3.4 Testing the Fisher Approximation

As defined in Section 3.1, the Fisher Matrix relies on the assumption of Gaussianity in the likelihood of the parameters. In general we know that this is not the case. There are many examples in the literature of error 'ellipses' between parameters that are far from ellipsoidal. As an example, an error contour plot for the parameters Ω_m, w plane from the Supernova Union project [19].

Another example of the discrepancy between simulations of data (through Monte Carlo Markov Chain (MCMC) methods) and Fisher Matrix techniques is shown in Figure 3.7, which is taken from [119] as Figure 3. This shows the projected error ellipses for the Planck CMB mission [114] over an 8-dimensional parameter space for both methods. The parameters under consideration are $(\Omega_b h^2, \Omega_{dm} h^2, f_\nu, \Omega_\Lambda, \tau, Y_{He}, A_s, n_s)$, representing respectively the baryon and the dark matter densities, the hot fraction of dark matter $f_\nu \equiv \Omega_\nu/\Omega_{dm}$, the cosmological constant energy density, the optical depth to re-ionisation, the primordial Helium fraction, and, finally, the primordial spectrum amplitude A_s and spectral index n_s. In some cases there is a large difference between the ellipse predicted from the Fisher Matrix, which assumes Gaussianity in the likelihood surface, and the simulated MCMC data. Moreover, in some cases the ellipses from simulations are smaller than the predicted error ellipse from the Fisher Matrix, which would seem to violate the Cramér-Rao bound. It is therefore worthwhile to develop a way to check this assumption by computing the higher order terms in the expansion of the log likelihood function.

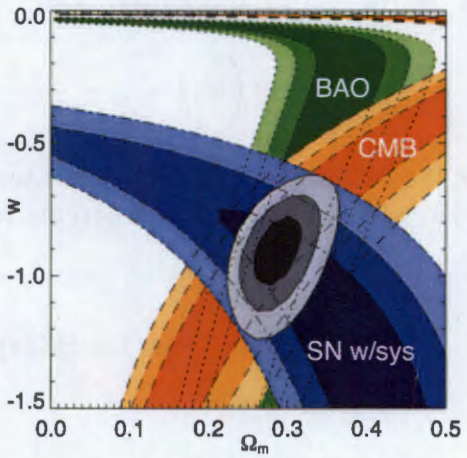

Figure 3.6: **Non-Gaussianity in likelihood contours** – An example error contour taken from the Supernova Union Project [19] in the Ω_m, w plane shows contours that are highly non-ellipsoidal. The 68.3%, 95.4% and 99.7% contours are shown for data from Supernovae, the Cosmic Microwave Background and Baryon Acoustic Oscillations. The seemingly non-Gaussian nature of the likelihood for these parameters is the motivation for testing the Fisher assumption of Gaussianity.

3.4.1 Taylor Series Expansion of the Log Likelihood

We start by writing the likelihood $\mathscr{L} = \exp(\ln \mathscr{L})$, and hence we can write the likelihood as a product of the exponent of all the terms in the Taylor series expansion for the log likelihood, given by

$$\begin{aligned} \ln \mathscr{L}(\vec{\theta^*} + \delta\vec{\theta}) &= \ln \mathscr{L}(\vec{\theta^*}) + \sum_i \ln \mathscr{L}(\vec{\theta^*}) + \delta\theta_i \\ &+ \frac{1}{2}\sum_{ij} \frac{\partial^2 \ln \mathscr{L}(\vec{\theta})}{\partial_{ij}}\bigg|_{\vec{\theta}=\vec{\theta^*}} \delta\theta_i\delta\theta_j \\ &+ \frac{1}{6}\sum_{ijl} \frac{\partial^3 \ln \mathscr{L}(\vec{\theta})}{\partial_{ijl}}\bigg|_{\vec{\theta}=\vec{\theta^*}} \delta\theta_i\delta\theta_j\delta\theta_l + \ldots \end{aligned} \tag{3.25}$$

The first term in this expression is merely a constant, and can effectively be ignored as an arbitrary normalisation. At the fiducial or input value of the parameters $\vec{\theta} = \vec{\theta}^*$, the likelihood is a maximum, and hence, the second term in the expansion, which contains first derivatives of

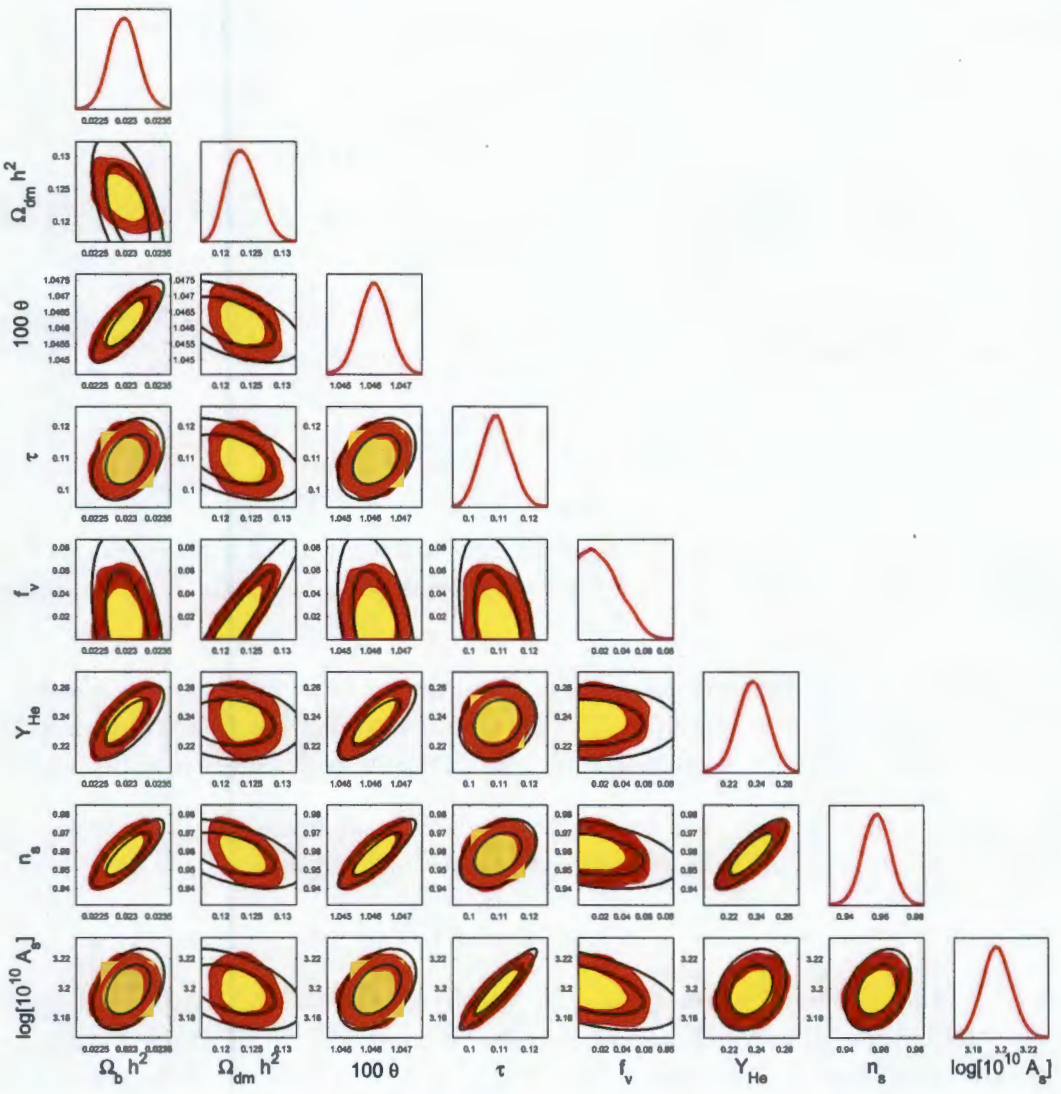

Figure 3.7: **Tests of the Fisher Matrix Approximation.** Projected 68% and 95% confidence levels from the Monte Carlo (colored/shaded) and the Fisher Matrix (black lines) methods, for Planck without lensing extraction and the minimal, eight-parameter ΛCDM model specified by the parameters $\{\Omega_b h^2, \Omega_{dm} h^2, f_\nu, \Omega_\Lambda, \tau, Y_{He}, A_s, n_s\}$, representing respectively the baryon and the dark matter densities, the hot fraction of dark matter $f_\nu \equiv \Omega_\nu / \Omega_{dm}$, the cosmological constant energy density, the optical depth to re-ionisation, the primordial Helium fraction, and, finally, the primordial spectrum amplitude and spectral index. Taken from [119]. The diagonal plots show the corresponding marginalised probabilities for each cosmological parameter. This plot shows how the Monte Carlo simulations and Fisher Matrix predictions do not always agree (and even seem to break the Cramér-Rao bound). Given the discrepancy between simulation and Fisher Matrix predictions, it is clear that testing the validity of the Fisher Matrix is important in cosmological analysis.

the likelihood, will be zero. The third term contains second derivatives,

$$F_{ij} = \sum_{ij} \frac{\partial^2 \ln \mathscr{L}(\vec{\theta})}{\partial_{ij}}\bigg|_{\vec{\theta}=\vec{\theta}^*}, \tag{3.26}$$

is the term used in traditional Fisher Matrix analysis, where $\partial_{ij} \equiv \partial^2/\partial\theta_i\partial\theta_i$ are derivatives with respect to the theoretical parameters in the model (for example H_0).

It is however the last term in the expansion which encodes the non-Gaussian contribution at third order to the log likelihood expansion, which we will denote by

$$G_{ijl} = \sum_{ijl} \frac{\partial^3 \ln \mathscr{L}(\vec{\theta})}{\partial_{ijl}}\bigg|_{\vec{\theta}=\vec{\theta}^*}, \tag{3.27}$$

where again we define $\partial_{ijl} \equiv \partial^3/\partial\theta_i\partial\theta_j\partial\theta_l$ as the third derivatives with respect to the cosmological parameters θ. We could include non-Gaussian terms of higher order, but for simplicity consider the third derivatives only at this point.

We would like to quantify how the term of third derivatives affects the likelihoods and errors on parameters derived in our analysis. We need to convert from Eq. (3.25) in terms of likelihoods to terms containing derivatives of observables, in the same way we rewrote Eq. (3.4) as Eq. (3.6).

Again we use the fact that we can relate the likelihood function $\mathscr{L}$ by to the χ^2 statistic by writing $\mathscr{L} \sim \exp[-\chi^2/2]$. Here we define χ^2 in vector form as

$$\chi^2 = ((\mathbf{d}-\mathbf{t})^{\mathrm{T}}\mathbf{C}^{-1}(\mathbf{d}-\mathbf{t})) \tag{3.28}$$

and $(\mathbf{d}-\mathbf{t})$ is a column vector (of length N, the number of data points) of the data $\mathbf{d}$ minus the theoretical model $\mathbf{t}$, which will be specific to a particular observable (which we named X_i). This definition is the more general case of Eq. (3.1.2), where we assumed that the covariance matrix C as diagonal. Furthermore, we assume that when evaluated at the maximum value of the likelihood we have

$$\langle(\mathbf{d}-\mathbf{t})\rangle = 0, \tag{3.29}$$

which is a key assumption in our derivation.

We start by using the product rule in taking derivatives of χ^2 with respect to the cosmological parameters θ_i using the definition Eq. (3.28). Note that we take derivatives of the theory with respect to the parameters - the data points represented by $\mathbf{d}$ do not change with the assumed theoretical model. As in Eq. (3.6), we assume that the errors (the covariance matrix, C) are only weakly dependent on the cosmological parameters, and so terms with derivatives of C^{-1}, namely the $\mathbf{C}_{,\mathbf{i}}^{-1}$ are neglected. They will be represented by $\mathscr{O}(\mathbf{C}_{,\mathbf{i}}^{-1})$.

3.4.2 Derivatives of χ^2

First Order Derivatives

We take derivatives of χ^2 at first order as

$$\begin{aligned} \chi^2_{,i} &= -\mathbf{t}^{\mathrm{T}}_{,i}\mathbf{C}^{-1}(\mathbf{d}-\mathbf{t}) - (\mathbf{d}-\mathbf{t})^{\mathrm{T}}\mathbf{C}^{-1}\mathbf{t}_{,i} + (\mathbf{d}-\mathbf{t})^{\mathrm{T}}\mathbf{C}^{-1}_{,i}(\mathbf{d}-\mathbf{t}) \qquad (3.30) \\ &= -\mathbf{t}^{\mathrm{T}}_{,i}\mathbf{C}^{-1}(\mathbf{d}-\mathbf{t}) - (\mathbf{d}-\mathbf{t})^{\mathrm{T}}\mathbf{C}^{-1}\mathbf{t}_{,i} + \mathcal{O}(\mathbf{C}^{-1}_{,i}). \qquad (3.31) \end{aligned}$$

Note that in the assumption of the vanishing average at the maximum of the likelihood, Eq. (3.29), this term falls away, which is what we expect from the form of Eq. (3.25).

Second Order Derivatives

At second order, the derivatives of χ^2 with respect to the parameters $\overrightarrow{\theta}$ are:

$$\begin{aligned} \chi^2_{,ij} &= \left[-\mathbf{t}^{\mathrm{T}}_{,ij}\mathbf{C}^{-1}(\mathbf{d}-\mathbf{t}) + \mathbf{t}^{\mathrm{T}}_{,i}\mathbf{C}^{-1}\mathbf{t}_{,j} + \mathcal{O}(\mathbf{C}^{-1}_{,j})\right] \\ &\quad + \left[\mathbf{t}^{\mathrm{T}}_{,j}\mathbf{C}^{-1}\mathbf{t}_{,i} - (\mathbf{d}-\mathbf{t})^{\mathrm{T}}\mathbf{C}^{-1}\mathbf{t}_{,ij} + \mathcal{O}(\mathbf{C}^{-1}_{,j})\right]. \end{aligned} \qquad (3.32)$$

The assumption that the average of χ^2 evaluated at the maximum (fiducial) value is zero as in Eq. (3.29) means that the first and third terms vanish. Under the assumption of uncorrelated data, the vector dot product can be written as a sum over products, or

$$\langle \chi^2_{,ij} \rangle = 2\left[\sum_k \frac{t_{k,i}t_{k,j}}{\sigma^2_k}\right]. \qquad (3.33)$$

We can then recover the first term of equation (3.4), where t here is the theoretical observable function, X:

$$F_{ij} = \left\langle \frac{\partial^2 \ln \mathscr{L}}{\partial_{ij}} \right\rangle = -\frac{1}{2}\langle \chi^2_{,ij} \rangle = -\sum_k \frac{t_{k,i}t_{k,j}}{\sigma^2_k}; \qquad (3.34)$$

where the sum (in Eq. (3.26)) over the indices i, j is an average, and the sum over $k = 1 : N$ is for all the data points.

Third Order Derivatives

Once again we use the chain rule to take derivatives of Eq. (3.32) in order to get the third derivatives of χ^2, neglecting once more all terms with first (or higher) derivatives of $\mathscr{O}(\mathbf{C}_{,\mathrm{i}}^{-1})$.

$$\begin{aligned}\left\langle \chi^2_{ijl} \right\rangle &= \left(\mathbf{t}^{\mathrm{T}}_{,ij}\mathbf{C}^{-1}\mathbf{t}_{,l} + \mathbf{t}^{\mathrm{T}}_{,l}\mathbf{C}^{-1}\mathbf{t}_{,ij}\right) \\ &+ \left(\mathbf{t}^{\mathrm{T}}_{,li}\mathbf{C}^{-1}\mathbf{t}_{,j} + \mathbf{t}^{\mathrm{T}}_{,j}\mathbf{C}^{-1}\mathbf{t}_{,li}\right) \\ &+ \left(\mathbf{t}^{\mathrm{T}}_{,jl}\mathbf{C}^{-1}\mathbf{t}_{,}i + \mathbf{t}^{\mathrm{T}}_{,i}\mathbf{C}^{-1}\mathbf{t}_{,jl}\right).\end{aligned} \tag{3.35}$$

Eq. (3.35) simplifies to

$$\left\langle \chi^2_{ijl} \right\rangle = 2\sum_k \left[\frac{t_{k,(ij}\, t_{k,l)}}{\sigma^2_k}\right] \tag{3.36}$$

in the uncorrelated case, with the round brackets indicating the three terms of symmetric permutations of i, j, l. In order to express the derivatives of the likelihood in terms of the derivatives we have found here, we again use $\langle \partial^3 \ln \mathscr{L}/\partial_{ijl} \rangle = -\frac{1}{2}\left\langle \chi^2_{,ijl} \right\rangle$, we have thus that

$$G_{ijl} = \left\langle \frac{\partial^3 \ln \mathscr{L}}{\partial_{ijl}} \right\rangle = -\frac{1}{2}\begin{cases}\mathbf{t}^{\mathrm{T}}_{,ij}\mathbf{C}^{-1}\mathbf{t}_{,l} + \mathbf{t}^{\mathrm{T}}_{,l}\mathbf{C}^{-1}\mathbf{t}_{,ij} + \\ \mathbf{t}^{\mathrm{T}}_{,li}\mathbf{C}^{-1}\mathbf{t}_{,j} + \mathbf{t}^{\mathrm{T}}_{,j}\mathbf{C}^{-1}\mathbf{t}_{,li} + \\ \mathbf{t}^{\mathrm{T}}_{,jl}\mathbf{C}^{-1}\mathbf{t}_{,}i + \mathbf{t}^{\mathrm{T}}_{,i}\mathbf{C}^{-1}\mathbf{t}_{,jl}.\end{cases} \tag{3.37}$$

This is the general form of the equation, and results in a tensor G_{ijl} with products of first and second derivatives. Again this can be simplified to the fully uncorrelated case as:

$$\left\langle \frac{\partial^3 \ln \mathscr{L}}{\partial_{ijl}} \right\rangle = \sum_k -\frac{1}{\sigma^2_k}\left[\frac{\partial^2 t_k}{\partial\theta_{(i}\partial\theta_j}\frac{\partial t_k}{\partial\theta_{l)}}\right] + \mathscr{O}\left(\frac{\partial \mathbf{C}^{-1}}{\partial\theta_i}\right), \tag{3.38}$$

where the round brackets on the indices imply the permutations of i, j, l.

3.4.3 The Fisher Flex Corrections

In the previous section we took analytical derivatives of the likelihood of the data at first, second and third order. Combining Eq. (3.25) with Eqs. (3.37) and (3.34) we have that at third order the 'flex corrected' form of the likelihood,

$$\ln \mathscr{L}(\vec{\theta^*} + \delta\vec{\theta}) = \ln \mathscr{L}(\vec{\theta^*}) + \frac{1}{2}F_{ij}\delta\theta_i\delta\theta_j + \frac{1}{6}G_{ijl}\delta\theta_i\delta\theta_j\delta\theta_l, \tag{3.39}$$

where we have truncated the expansion of the log likelihood at third order, for simplicity. In order to quantify the important of including such effects, we must compare the likelihoods of

the parameters on the assumption of Gaussianity, with the change once we include the term involving G_{ijl}.

The likelihood is in general a function of many parameters (in our cosmological example we have 5 parameters of interest). To consider the flex corrections in general we need to marginalise over all the parameters we are not interested in, which involves taking integrals over the parameter space of those 'nuisance' parameters. In order to do this marginalisation we need to make some simplifying assumptions about the nuisance parameters.

We can consider a special sub-case, however, where we merely set the other parameters to their fiducial values and then compute one-dimensional likelihoods for the parameters of interest.

Computationally, this involves taking the matrix of first derivatives of the full set of parameters (again with reference to the cosmological example this would be a 5×5 matrix), and taking one column of this matrix that contains first derivatives of the parameter of interest. One can then perform numerical differentiation to this column to obtain another matrix of second derivatives of all that column with respect to the other parameters.

To plot the likelihood itself, we take steps in the parameter space $\delta\theta_i \equiv \theta_i - \theta_i^*$ for each parameter i. The one-dimensional likelihoods obtained in this manner are shown in Figure (3.8) for the example of the Hubble parameter, $H(z)$.

3.4.4 Fisher Flex Test

Using the one dimensional likelihoods, we can construct a Fisher Flex test, which will indicate whether or not the assumption of Gaussianity is valid, or more precisely, just how large the deviation from Gaussianity is.

Assuming Gaussianity, the 1σ error is defined to be the position $\theta = \theta^* + \sigma$ where the likelihood drops to $1/\sqrt{e}$. Similarly one can ask what are the values σ^+, σ^- which coincide with the values on either side of θ^* where again the likelihood drops to $1/\sqrt{e}$. Since the flex-corrected likelihood is no longer Gaussian, they will in general have very different values. Hence we can define

$$\Delta = \max\left(\frac{|\sigma^+ - \sigma|}{\sigma}; \frac{|\sigma - \sigma^-|}{\sigma}\right). \tag{3.40}$$

By comparing the size of the largest of the two 'non-Gaussian' σs with the Gaussian σ, one can measure how far away from Gaussian the likelihood is, and thus how the assumption of Gaussianity will change the inferred errors on the parameters.

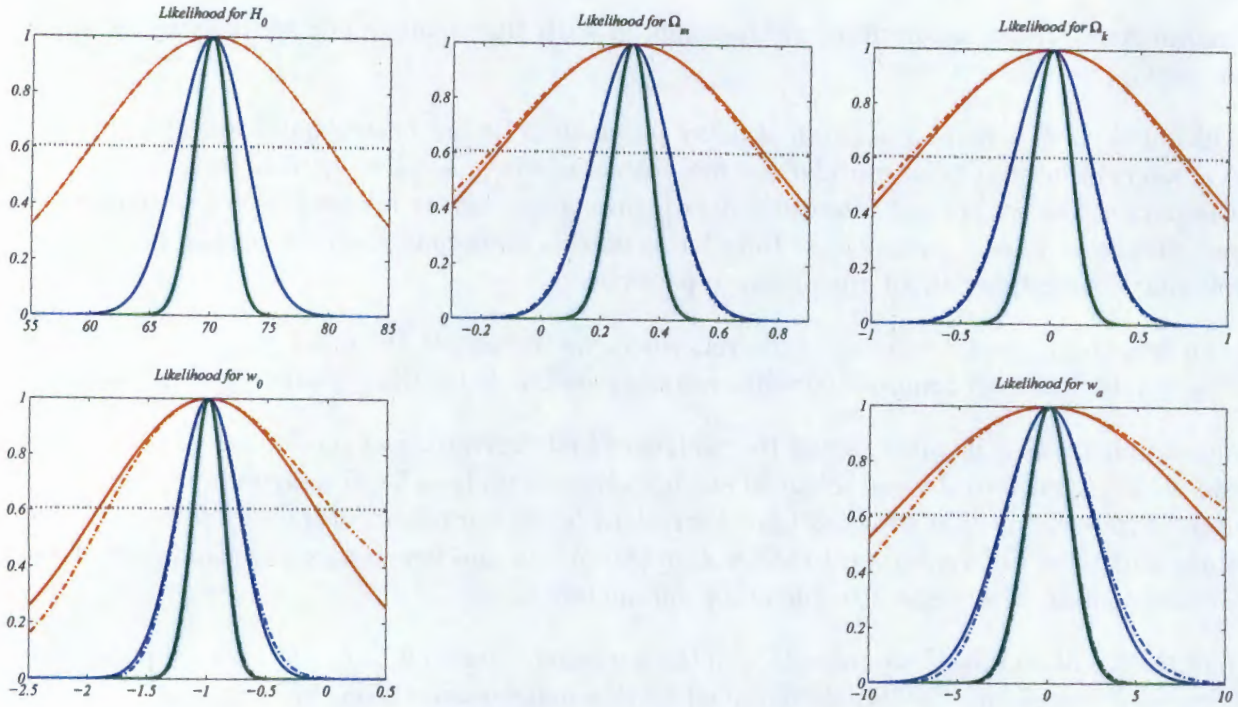

Figure 3.8: **Testing the assumption of Gaussian likelihoods.** The 1-dimensional likelihoods of the parameters $(H_0, \Omega_m, \Omega_k, w_0, w_a)$ are given assuming Gaussianity and using the normal Fisher Matrix **(solid lines)** and including the contribution from the non-Gaussian higher order derivatives of the χ^2 **(dashed lines)**. These likelihoods are considering measurements of the Hubble parameter at redshifts $0 < z < 1.1$, as summarised in Table 3.1. The size of the flex correction increases for increasing errors on the measurement of H. The likelihoods are shown for $\delta H = (0.05, 0.1, 0.35)$ respectively.

3.5 Conclusions

The Fisher Matrix is a powerful statistical tool to perform error projection and forecasting for future surveys and experiments, and is particularly useful in astrophysics and cosmology. It is an efficient way to project errors on cosmological observables to constraints on parameters, and allows one to investigate degeneracies between parameters quickly and easily. We introduced the Fisher formalism, and provided an example of the Fisher derivatives for the specific cosmological example of the Hubble parameter.

In the standard Fisher Matrix formalism, Gaussianity is assumed in the likelihood of the parameters. Analyses of real data have, however, shown that this is not always the case. This assumption of Gaussianity could incorrectly bias estimates of the error on parameters, which is potentially of much interest for designing and optimising cosmological surveys. We introduce

Fisher Flex Corrections to the standard Fisher Matrix formalism, as higher order derivatives of the log likelihood. This Fisher Flex test provides a check as to whether the assumption of Gaussianity is valid in parameter estimation forecasting.

Fisher Matrix techniques will be used in Section 4 when we investigate the relationship between dark energy and other cosmological parameters, such as the curvature and matter densities of the Universe.

Chapter 4

Dark Energy Degeneracies with Cosmological Parameters

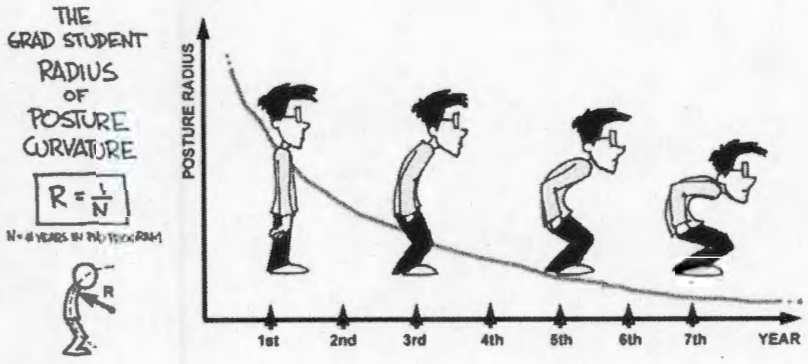

Figure 4.1: © Jorge Cham, online at www.phdcomics.com 11/22/1999

4.1 Introduction

Incorrect assumptions about densities, Ω_m and curvature, Ω_k have powerful implications for the reconstruction of dark energy dynamics. Errors in curvature are particularly important and hence Ω_k needs to be marginalised over in addition to the usual cosmic parameters in any real analysis. We discuss these degeneracies between dark energy and the cosmic parameters given perfect measurements of Hubble rate, distances and the infinitesimal volume element, both parametrically and in a non-parametric framework. This work has been published in [120].

The problem of dark energy is one of the key unsolved problems in modern cosmology. The last decade has seen much work in both the observational and theoretical community in an attempt to understand its origin and nature. The main thrust of this work has been in detecting deviations from the simplest model of dark energy, the ΛCDM model, and to determine the possible dynamical behaviour of the equation of state as a function of redshift, $w(z)$. We introduce dynamical dark energy in Section 1.11. Any observations made are, however, sensitive to many cosmological components like the cosmic curvature Ω_k, and the energy density of matter Ω_m, and not exclusively to dark energy. This leads to degeneracies between these cosmological components and the inferred dark energy. These degeneracies have been investigated by many in the cosmology community [121, 122, 123, 124].

As an illustration, this degeneracy can be seen in Figure 12 of the recent WMAP5 results [6] (here Figure 4.2), which shows the degeneracy between the curvature of the Universe and dark energy. The CMB on its own provides weak constraints on curvature due to this curvature-dark energy degeneracy, as can be seen from the blue error contour in the left panel of Figure 4.2. Adding measurements of distances (the angular diameter distance and luminosity distance are introduced in Section 1.7) significantly improves the constraints. This complimentarity of probes is illustrated in Figure 4.3 of Section 4.4.1, where we show how the errors on dark energy decrease when combining data from both the Hubble parameter and distance information, even allowing for uncertainty in the curvature of the Universe. We discuss the complimentarity between the expansion and distance measures in Section 4.4.

Clarkson *et al.* [122] discussed this degeneracy between the geometry of the universe and the dark energy equation of state in that a Universe with constant equation of state in the presence of spatial curvature can mimic one with dynamical dark energy. We extend this work to include investigations of the degeneracies that result from cosmic volume measurements, *without assuming* a particular form for the parametrisation of dark energy.

It is common practice, however, to assume some functional form for the dynamical equation of state (examples of some parametrisations are given in Section 1.11). We show how curvature affects the inferred values of the parameters in certain models of dark energy, and link our non-parametric approach to standard techniques.

In the case of the degeneracies with matter, Kunz [121] argues that observations are only sensitive

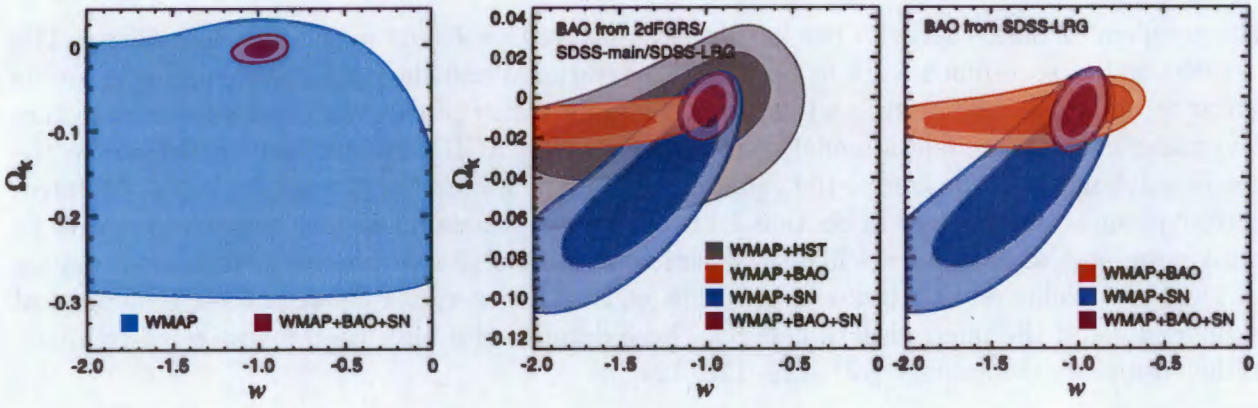

Figure 4.2: **The curvature-dark energy degeneracy.** The marginalised 65% (**dark inner contours**) and 95% contours in the $\Omega_k - w$ plane (with a prior on the constant $w > -2.5$), as Figure 12 from [6]. The left panel shows the 95% contour level from WMAP measurements alone. Constraints on the parameters are improved with the inclusion of data from SNe from the Hubble Space Telescope [71, 70], the Supernova Legacy Survey (SNLS) [68] and the SupErNovae Trace Cosmic Expansion (ESSENCE) survey [69] (WMAP + SN) and from the measurements of the Baryon Acoustic Oscillations in the Sloan Digital Sky Survey (SDSS) galaxies [32] (and the LRG subset) [31, 35] and the Two degree field (2dF) survey[125], labelled collectively by WMAP + BAO. Also included are measurements of the Hubble constant [126] (WMAP + HST). The difference between the right and middle panels is that the right hand panel has a slightly weaker prior [32]. This shows that the CMB alone cannot break the degeneracy between dark energy and curvature, while including data from many probes helps narrow the constraints.

to the full energy-momentum tensor and thus cannot see beyond a combination of the dark matter and dark energy component. This provides motivation for reconstructing the degeneracies between dark energy and matter from perfect observations.

4.2 Parametric Degeneracies with Dark energy and Curvature

We begin with a standard method of reconstructing dark energy from observations, given errors on those observations. We introduced the Fisher matrix formalism in Chapter 3. Not only can the Fisher matrix allow one to project how errors on observables from future surveys will impact the inferred errors on parameters, but this treatment allows us to investigate the relationship between specific cosmological parameters for a given survey. This is particularly useful in understanding the degeneracy between cosmic curvature and dark energy in a parametric way. That is, by parameterising the form of $w(z)$ we can investigate the degeneracy between Ω_k and the parameters in the specific dark energy model.

To illustrate this, we compute the Fisher error ellipses for the parameters w_0, w_a in the CPL parametrisation

$$w(z) = w_0 + w_a \frac{z}{1+z}, \tag{4.1}$$

which is given as Eq. (1.45) in Chapter 1.11. Once we have obtained the Fisher matrix F_{AB} from the derivatives of the observables we consider using Eq. (3.6) and the covariance matrix of the data, we add in the prior matrix on the parameters, as

$$F_{AB} \rightarrow F_{AB} + P_{AB}, \tag{4.2}$$

which encodes any prior information on the parameters, as outlined in Chapter 3. In general this matrix allows for correlation between the parameters, but in the case where the parameters θ_i are uncorrelated, this prior matrix is a matrix with diagonal entries $P_i = 1/\sigma_i^2$. In other words this prior matrix gives a measure of how certain we are of the input value of the parameter, and is based on prior experiments and theory.

However, we will see that changing the prior value on the curvature parameter (or our confidence in our previous measurements of curvature) has a large affect on the resultant error ellipses in the *dark energy* parameter space. We illustrate this in Figure 4.3, produced using the Fisher4Cast suite of code [107, 111]. This error ellipse in the $w_0 - w_a$ plane is shown for changes in the value of the prior on the curvature from Prior$(\Omega_k) = 10^1$ to Prior$(\Omega_k) = 10^6$, while keeping prior values on the other parameters fixed. We plot this for the both expansion rate $(H(z))$, distance measurements, e.g. $d_A(z)$, and the ellipse resulting from the combination of both observables. It is worth noting that the combined error ellipse provides much tighter

constraints on the coefficients in the dark energy equation of state parametrisation, although even this combined ellipse is degraded with curvature. We will see this degeneracy broken in a similar fashion when considering the non-parametric degeneracy between curvature and dark energy in Section 4.3.

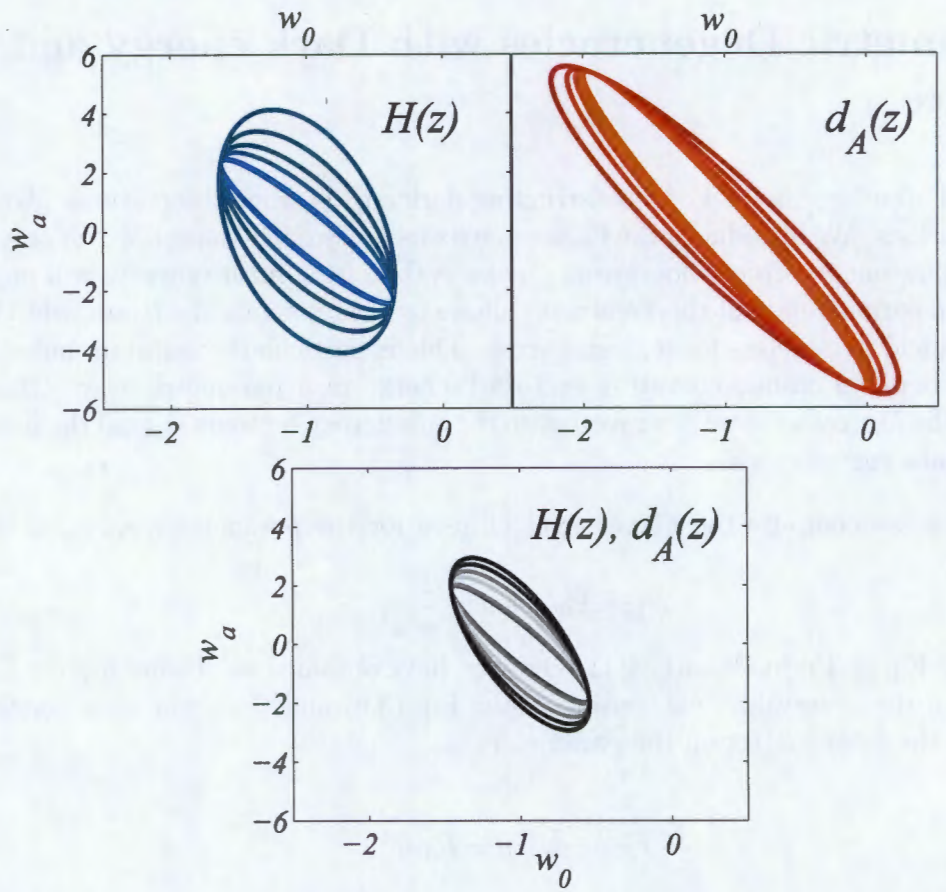

Figure 4.3: **Curvature degrades the errors.** Error ellipses in $w_0 - w_a$ plane for a survey characterised by Table 3.1 in Chapter 3. The ellipses shown are for measurements of the Hubble parameter (**blue curves**) and the angular diameter distance (**orange curves**). The black ellipse is obtained by combining the data from both observables, hence yielding much tighter constraints on dark energy than the observables considered separately. We vary the prior on the energy density of the curvature, Ω_k from 10^6 (innermost curves) to 10 (outer curve) in factors of 10, except for the last three steps, which are 46, 22 and 10 respectively. As the curvature prior gets weaker (i.e. we are less confident in the flatness of the Universe), the size of the error ellipse in the w_0, w_a parameters increases, and so our constraints on dark energy are weakened. Changing the prior on curvature also rotates the ellipse, which corresponds to changing the degeneracy direction between the dark energy parameters. Figure produced using Fisher4Cast [107, 111].

This degrading of the error ellipse translates into a change in the Figure or Merit of the survey, as introduced in Chapter 3. As the prior on curvature increases, the size of the error ellipse in the $w_0 - w_a$ plane decreases, which results in an increase in the Figure of Merit (FoM). This is illustrated in Figure 4.4, which was constructed using the Fisher4Cast code [107, 111] for the survey data summarised in Table 3.1 in Chapter 3. The figure of merit flattens out for both very large and very small values of the prior. This can be explained by the fact that for very large prior values the contribution of the cosmic curvature is essentially "nullified", whereas for very small values of the curvature the prior is effectively zero and the ellipse is completely degenerate with the curvature.

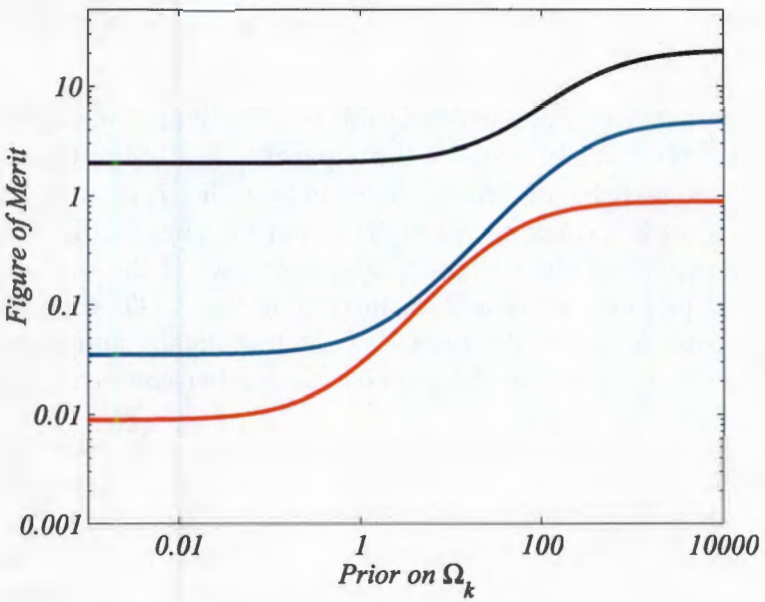

Figure 4.4: **Increasing the FoM by changing prior on curvature.** As illustrated in Figure 4.3, curvature degrades the error on the dark energy parameters. We plot the Dark Energy Task Force (DETF) Figure of Merit [60] (the inverse of the area of the ellipse in the $w_0 - w_a$ plane) as a function of the prior on the energy density of curvature, Ω_k for the Hubble parameter **(blue curve)** and angular diameter distance **(orange curve)** separately and for the combined error ellipse **(black curve)**. In all cases the shape of the curve is roughly the same, with no change in the FOM beyond a certain value of the prior, both in case of very large and very small priors. Figure produced using Fisher4Cast [107, 111].

4.3 The Non-Parametric Dark Energy Equation of State from Observations

We have illustrated how curvature degrades our constraints on the dark energy parameters in an assumed model. However, one can reconstruct this degeneracy in a fully non-parametric approach without assuming a particular function form for $w(z)$.

We consider three key observables of the background geometry when investigating the degeneracies between dark energy and other cosmic parameters, namely measurements of distances using the concept of 'standard candles' or 'standard rulers', of the Hubble parameter and of the change in the fractional volume of the Universe (e.g. from number-counts), as defined in Section 1.7 of Chapter 1.

The Hubble parameter is in its own right an observable which will play an important role in future dark energy experiments. $H(z)$ is a measure of the expansion rate of the Universe, and allows us to directly probe its dynamical behavior. As discussed in Section 1.7, Baryon Acoustic Oscillation surveys simultaneously provide measurements of $H(z)$ and the angular diameter distance, $d_A(z)$ at the same redshift by exploiting the radial and angular views of the acoustic oscillation scale [34, 33], a fact that will provide key new data in coming years [35, 40, 127]. The third key background test we will discuss is the observation of the fractional volume change as a function of redshift which can also in principle be determined via number-counts or the BAO.

We wish to reconstruct both the dark energy equation of state as a function of redshift $w(z)$ and the values of Ω_k, Ω_m from observations of the above three functions. It was shown in [122] that we can determine the curvature directly, and independently of the other parameters or dark energy model by solving for the curvature in the equation for the distance $D_t(z)$, (given in Chapter 1 as Eq. (1.34)) which is related to the angular diameter distance d_A and luminosity distance d_L by $d_L(z) = c(1+z)D_t(z)/H_0 = (1+z)^2 d_A(z)$. Solving for the curvature in Eq. (1.34), we obtain

$$\Omega_k = \frac{[H(z)D_t'(z)]^2 - H_0^2}{[H_0 D_t(z)]^2}. \tag{4.3}$$

The key thing to note in Eq. (4.3) is that while the right hand side is a function of redshift, the left hand side of the equation is valid at any redshift. Such independent measurements of the curvature of the universe can in turn be used to test the Copernican Principle in a model-independent way, which was proposed in [79].

The key idea behind this non-parametric approach is that assuming we have 'perfect' and uncorrelated data from observations we would like to reconstruct $w(z)$ *without assuming* a specific parametrisation. Depending on the particular observable of interest, there are different ways to reconstruct w.

4.3.1 Dark Energy from Hubble Measurements

It is straightforward to find $w(z)$ from the Hubble rate [128, 123], from Eq. (1.20), and is given by:

$$w(z) = -\frac{1}{3}\frac{\Omega_k H_0^2(1+z)^2 + 2(1+z)HH' - 3H^2}{H_0^2(1+z)^2[\Omega_m(1+z)+\Omega_k] - H^2}. \tag{4.4}$$

Here the prime in this equation indicates the derivative of the Hubble parameter with respective to redshift. If we knew the values of Ω_m and Ω_k, this equation would fully specify the dark energy. However, this explicitly reveals a degeneracy between Ω_m and $w(z)$ which cannot be overcome by background tests alone [121]. This is discussed further in Section 4.4.2. By considering the Friedmann equation, Eq. (1.19), we see that individual tests of the background cosmology such as $H(z), D_t(z), V'(z)$ measure the combination $\Omega_m + \Omega_{DE} f(z)/(1+z)^3$, but not the two separately.

In a similar manner to the reconstruction of $w(z)$ from the Hubble parameter, we can reconstruct dark energy from the other two observables.

4.3.2 Dark energy from Distance measurements

From distance measurements, we may invert Eq. (1.34) by solving for $w(z)$ in the equation. This yields

$$w(z) = \frac{2\,(1+z)\,(D_t^2\Omega_k + 1)\,D_t'' - D_t'\left[\Omega_k\,(1+z)^2\,D_t'^2 + 2\,\Omega_k D_t\,(1+z)\,D_t' - 3 - 3\,D_t{}^2\Omega_k\right]}{3\left\{\left[\Omega_k + \Omega_m\,(1+z)\right](1+z)^2\,D_t'^2 - D_t^2\Omega_k - 1\right\}D_t'}, \tag{4.5}$$

Hence we can reconstruct the dynamical dark energy from measurements of the distance $D_t(z)$, from either angular diameter distance measurements or measurements of the luminosity distance and their derivatives. Volume measurements effectively 'combine' both distance measurements and the Hubble parameter, and we apply similar techniques to reconstruct $w(z)$.

4.3.3 Dark Energy from Volume Measurements

As outlined in Section 1.9, the infinitesimal volume element is given by Eq. (1.39) as

$$V'(z) \equiv \frac{\mathrm{d}^2 V}{\mathrm{d}z\mathrm{d}\Omega} = \frac{c^3 D_t(z)^2}{H_0^2 H(z)}. \tag{4.6}$$

In order to reconstruct $w(z)$ from volume measurements as an analytical formula we need to solve for $w(z)$ from Eq. (4.6), where is appears in the expression for $D_t(z)$ as a double integral (Eq. (1.34)) and in $H(z)$ in the form of $f(z)$ as one integral over z. Hence it is rather tricky

to obtain an analytical expression for $w(z)$ as it involves the root of a quartic power. Instead we reconstruct $w(z)$ by solving the differential equation for $f(z)$ and then differentiating to get $w(z)$.

Starting with Eq. (1.34), we solve for the derivative of the Hubble parameter and equate this with the expression for H' in terms of $w(z)$ from Eq. (4.4) and use

$$w(z) = \frac{(1+z)f'(z)}{3f(z)} - 1 \tag{4.7}$$

to yield a first order differential equation for $f(z)$, namely

$$f'(z) = -\frac{A(z) + B(z) + C(z)}{H_0^2 V' \Omega_{\rm DE}}, \tag{4.8}$$

where

$$A(z) = -4\Big(V' H_0 \left(c^3 \sqrt{f(z)\Omega_{\rm DE} + X_{11}} + V' H_0^3 \Omega_k \left(f(z)\Omega_{\rm DE} + X_{11}\right)\right)\Big)^{1/2},$$

with

$$X_{ab} = (1+z)^2(a\Omega_k + b\Omega_m(1+z)),$$
$$B(z) = 2H_0^2 V'' \left(f(z)\Omega_{\rm DE} + X_{11}\right)$$

and

$$C(z) = H_0^2 V'' \frac{X_{32}}{1+z}.$$

We solve this set of equations for $f(z)$ and then use (4.7) again to yield $w(z)$. The solution for $f(z)$ is unique since we demand $f(0) = 1$.

4.4 Reconstructing $w(z)$

From Sections 4.3.1, 4.3.2, 4.3.3 we have three separate expressions for $w(z)$ from observations. Assuming we lived in an exact FLRW universe, if we knew Ω_m and Ω_k perfectly then these expressions for $w(z)$ would yield the same function $w(z)$. However we do not know the curvature (or matter density) perfectly. So the question is: what is the effect of, for example, imposing flatness on the Universe - or more explicitly, imposing $\Omega_k = 0$ when the true curvature is actually non-zero?

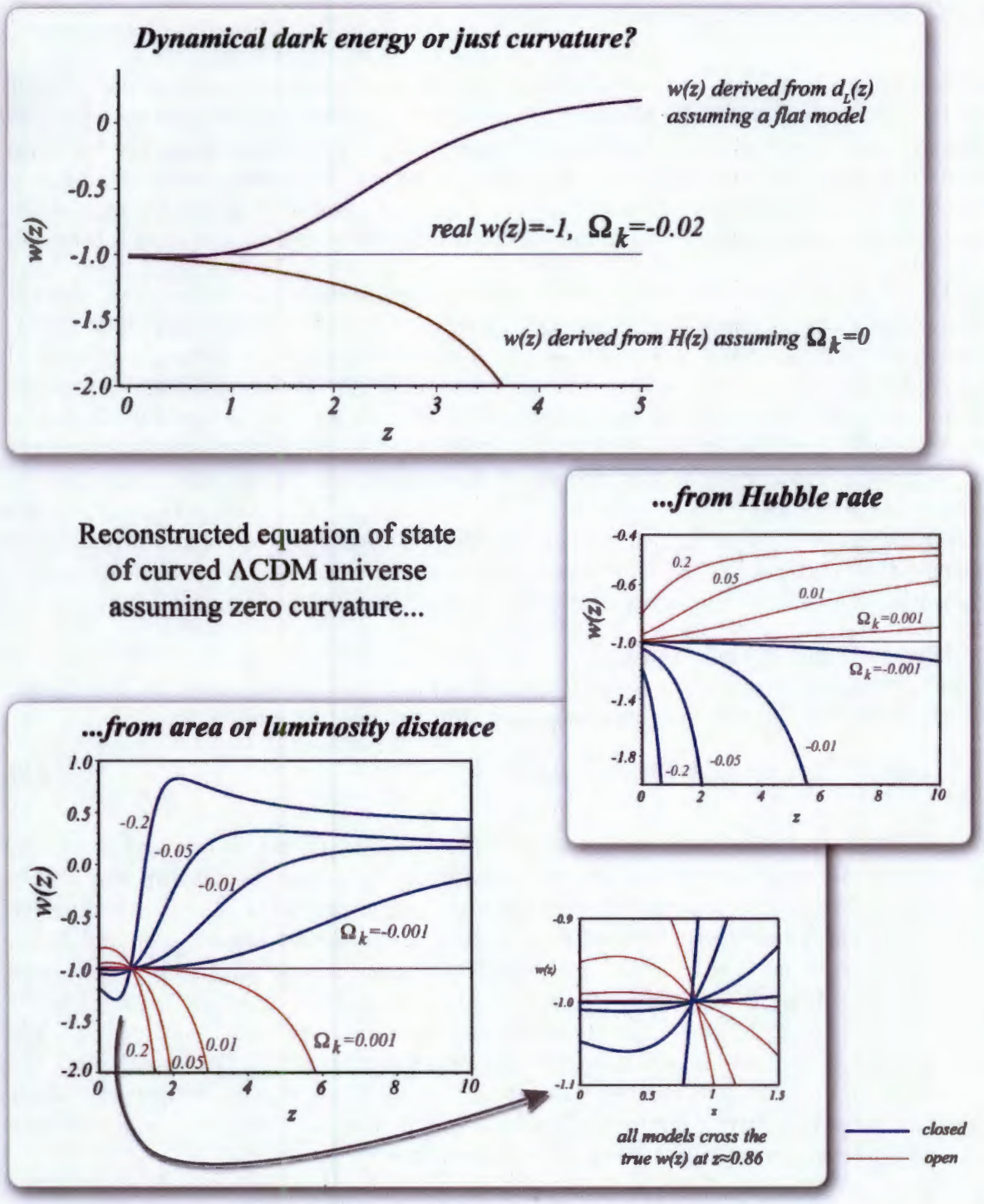

Figure 4.5: **Reconstructing the dark energy equation of state assuming zero curvature** when the true curvature is 2% in a closed ΛCDM universe. The $w(z)$ reconstructed from $H(z)$ is phantom ($w < -1$) and rapidly acquires an error of order 50% and more at redshift $z \gtrsim 2$, and diverges at finite redshift. The reconstructed $w(z)$ from $d_L(z)$ for $\Omega_k < 0$ is phantom until $z \approx 0.86$, where it crosses the true value of -1 and then crosses 0 at high redshift, where the bending of geodesics takes over from dynamical behavior, producing errors in opposite direction to the DE reconstructed from $H(z)$. In order to make up for the missing curvature, the reconstructed dark energy is behaving like a scalar field with a tracking behavior. These effects arise even if the curvature is extremely small ($< 0.1\%$). Reprinted from [122].

4.4.1 Zero Curvature Assumption

In most cosmological analyses, it is usually implicitly assumed that the error on $w(z)$ will be of order Ω_k, but, as was shown by Clarkson, Bassett and Côrtes in [122] this is not the case. They illustrated the implications of incorrectly assuming flatness by constructing the functions $d_L(z)$ and $H(z)$ under the assumption of the ΛCDM in a curved Universe (i.e. assuming $w = -1, \Omega_k \neq 0$) and inserting the results into Eqs. (4.4) and (4.5). In other words, we reconstruct the dynamical dark energy that would mimic a curved universe with a cosmological constant.

Setting $\Omega_k = 0$ in Eqs. (4.4) and (4.5), we arrive at the two different $w(z)$ functions required to reproduce the curved forms for $H(z)$ and $d_L(z)$ in a *flat* Universe with dynamic dark energy. This would apply equally to $d_A(z)$ for that matter, since the two distances measures are related only by a factor of $(1+z)^2$. We reproduce Figure 1 from [122], here as Figure 4.5, which presents this method using for simplicity the concordance value of $w = -1$. The qualitative results do not depend on the 'true' underlying dark energy model (i.e. the results are similar if another constant value of w was in fact the true underlying model, and not a cosmological constant). In addition, the assumption of flatness *per se* is not a special case, as the results presented here are qualitatively the same for any assumed Ω_k which is different from the 'true' value. In this figure, it is assumed that $\Omega_m = 0.3$ in all expressions; numbers quoted are weakly dependent on this. The implication of assuming the incorrect value for Ω_m is addressed in Section 4.4.2.

The spurious $w(z)$ inferred under this incorrect assumption of flatness can simply be thought of as the function required to yield the same $H(z)$ or $d_L(z)$ as in the actual curved ΛCDM model, or explicitly we equate the following expression (e.g. for distance measures)

$$d_L[\text{flat}, w(z)] = d_L[\text{curved}, w(z) = -1]. \tag{4.9}$$

We stress yet again that this is a non-parametric approach, as we do not assume any particular form for $w(z)$, and instead reconstruct the free function $w(z)$ at each redshift. In Fig. 4.5 we show that for ΛCDM the curvature manifests itself as evolving dark energy. The panels show the dynamical dark energy incorrectly inferred from perfect observations when we assume flatness, where the true universe is curved. In the case of the Hubble rate measurements this is clear since we are essentially solving the equation $\Omega_{DE} f(z) = \Omega_\Lambda + \Omega_k(1+z)^2$ as a function of redshift, where $f(z)$ is given by Eq. (3.14). For $\Omega_k > 0$ (open universe), $w(z)$ must converge to $-1/3$ to compensate for the curvature, which evolves as $(1+z)^2 = (1+z)^{3(1+-1/3)}$. For $\Omega_k < 0$, the opposite occurs and a redshift is reached when $w \to -\infty$ in an attempt to compensate, albeit unsuccessfully, for the positive curvature. Clearly assuming that the error on w is of the same order of magnitude as the error on the curvature is very incorrect.

By comparing the panels for the Hubble parameter and the luminosity distance from Fig. 4.5, we see that the errors in w reconstructed from $d_L(z)$ and $H(z)$ have opposing signs at $z \gtrsim 0.9$. This relates to the curvature of the geodesics in that above a critical redshift the effect of curvature on the geodesics (which affects the distance measurements) becomes more important than the pure

dynamics (as traced by the Hubble parameter). Hence the luminosity distance flips $w(z)$ in the opposite direction to that reconstructed from $H(z)$. This opposite sign in the reconstructed $w(z)$ will allow us to break the degeneracy between curvature and dark energy. This combination of measurements is key to breaking the degeneracy, even in the parametric approach. This can be seen in Fig. 4.3, where the combination of observables reduces the size of the error ellipse in the $w_0 - w_a$ plane.

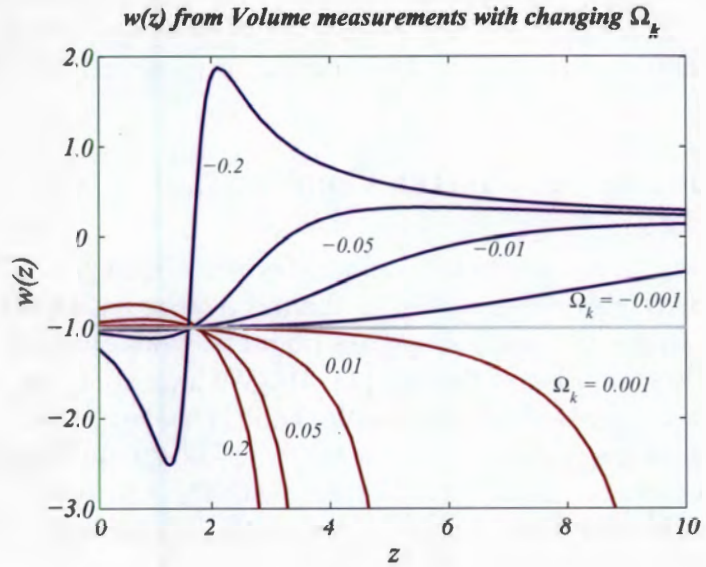

Figure 4.6: **Reconstructed dark energy from volume measurements while incorrectly assuming flatness.** Similar to the case for distance measurements in a closed Universe, the $w(z)$ reconstructed from perfect volume measurements must initially be phantom in order to compensate for curvature, and crosses the true value of $w = -1$ at a redshift of z 1.6, which is greater than the redshift of 0.86 for the distance measurements alone [122]. This is due to the dark energy appearing in the equation for the volume both in the expansion rate and in the distance measure. After this critical redshift, the $w(z)$ increases to overcome the curvature of the geodesics. Published in [120].

In the case of volume measurements the reconstructed $w(z)$ has a similar form to the w we obtained from the distance measurements $D_t(z)$. This makes sense by noting from Eq. (1.39) that the distance information enters the equation as a square power. For example in the closed Universe case the reconstructed $w(z)$ drops to more phantom values (-2.5 compared to -1.3 for the distance measurements) in order to make up for the missing curvature. Again the effect of curvature on the geodesics dominates the effect of dynamics for large z, and the distance contribution in the volume measurements flips the reconstructed $w(z)$ at $z = 1.6$. The critical redshift of this flip is determined by the redshift at which the curvature of the geodesics affecting distance measurements becomes more important than the expansion rate. This playoff is more finely balanced for volume measurements due to the fact that $H(z)$ appears both in $D_t(z)$ (as

a square power) and on its own. So $w(z)$ has to work harder in reproducing curvature to counterbalance the opposing trends of expansion history and geometry, and so the balance is achieved at higher redshift. The specific redshift at which this happens is dependent on Ω_m in that lower values imply higher value of the critical redshift. Hence we see that incorrectly assuming flatness in measurements of the background observables can result in a reconstructed $w(z)$ that mimics dynamics, yielding errors on w that are much larger than the order of errors on Ω_k. However, from Eqs. (4.3.1) - (4.3.3) we recall the degeneracy also extends to the matter density of the Universe. Hence we extend this analysis to investigate what happens when a particular value for the matter density in the Universe, Ω_m is incorrectly assumed.

4.4.2 Uncertainties in the Matter Content Ω_m

Measurements of the power spectrum from Cosmic Microwave Background (CMB) data and from measurements of BAO provide estimates of the matter content of the universe. While constraints on Ω_m are sharpened by combining data from many observations, the best-fit value is often derived under the assumption of flatness [35, 31]. We have seen that unlike the case for cosmic curvature, the degeneracy between observables and the matter content is perfect and we show that incorrectly assuming a particular value for Ω_m can also mimic deviations from ΛCDM. Here we again reconstruct $w(z)$ (now in a flat Universe with $\Omega_k = 0$) but here the errors occur when assuming the concordance value of $\Omega_m = 0.3$ incorrectly. For example in this case the $w(z)$ reconstructed from Hubble measurements Eq. (4.4) reduces to

$$w(z) = -\frac{1}{3}\frac{2(1+z)HH' - 3H^2}{H_0^2(1+z)^2[\Omega_m(1+z)] - H^2}. \tag{4.10}$$

Similar expressions are found for both the distance and volume measurements. The $w(z)$ curves obtained from incorrectly assuming $\Omega_m = 0.3$ are shown in Fig. 4.7. The complete degeneracy can be explained as follows: if we assume flatness for this example we find that changing the value of Ω_m can only affect the dark energy density, and thus change the value of $H(z)$. Since Ω_m is only present in all three observables through $H(z)$ or integrals of $1/H(z)$ (whereas the curvature entered the expression for $D_t(z)$ in an independent way), the reconstructed $w(z)$ is the same for all three measurements.

The reconstructed $w(z)$ curves do not go through $w = -1$ at $z = 0$, but are spread between -0.85 and -1.15 for $0.2 < \Omega_m < 0.4$. This has implications for the inferred values of Ω_m at late times, and suggests care must be taken to understand the assumptions involved in our inferences of cosmic parameters today. This spread is also illustrated in Fig. 4.8.

We would like to quantify the effect of incorrectly assuming the value of the curvature or matter densities on the value of the dark energy at late times. Given any scenario of an assumed cosmology that differs from the 'true' Universe, we can derive the value of today, $w(z = 0)$ from

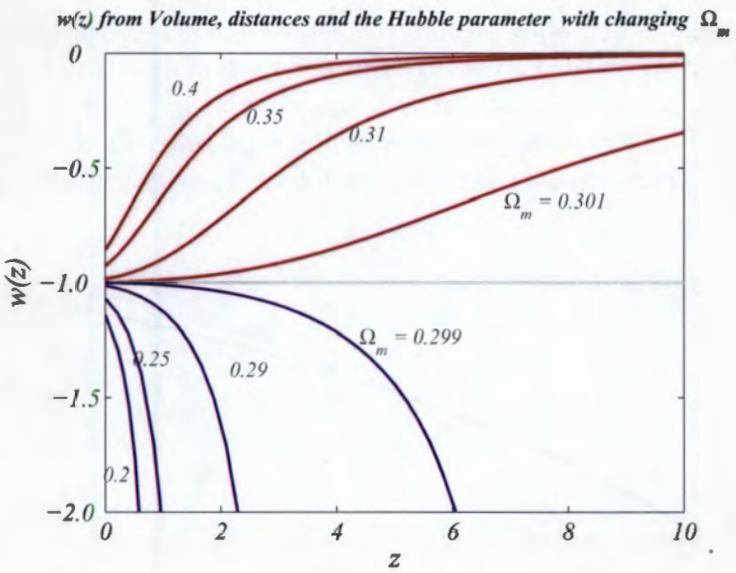

Figure 4.7: **Reconstructed dark energy from an incorrectly estimated matter density.** The reconstructed $w(z)$ for changing Ω_m from all three measurements $(H, d_L, dV/dz)$. Since we assume flatness while only changing Ω_m, all three observables yield the same reconstructed $w(z)$, since Ω_m only enters the functions through $H(z)$ or integrals of $1/H$. For $\Omega_m > 0.3$ the dark energy tries to compensate for the extra matter contribution and so asymptotes to $w = 0$ as $z \to \infty$. For $\Omega_m < 0.3$ the $w(z)$ is of the same form to what is reconstructed from neglecting curvature in a closed Universe (see Fig. 4.5), and the phantom w tends to $-\infty$ as it attempts to compensate for the 'missing' matter density. Published in [120].

both the Hubble and distance measurements as

$$w(0) = \frac{3 - 4\Omega_{k*} - 3\Omega_m + \Omega_k}{6\Omega_m + 6\Omega_{k*} - 3\Omega_{m*} - 3 - 3\Omega_k} \sim \frac{\epsilon_m}{(-1+\Omega_{m*})} - \frac{2\Omega_k}{3(-1+\Omega_{m*})} - 1, \tag{4.11}$$

where $\epsilon_m = \Omega_{m*} - \Omega_m$ as defined above where the asterisk indicates the assumed but incorrect values of the corresponding quantities. We vary this equation in one 'true' density (Ω_m or Ω_k) at a time, while keeping the other constant at the assumed value of either $\Omega_k = \Omega_{k*}$ or $\Omega_m = \Omega_{m*}$ to produce the curves in Fig. 4.8. This parameter $w(z = 0)$ allows us to easily quantify the affect of assuming an incorrect cosmological model on the inferred low-redshift value of w.

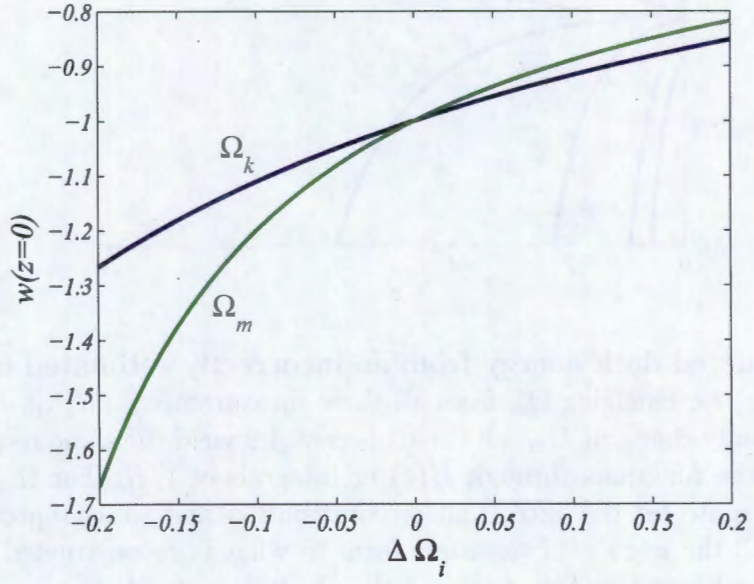

Figure 4.8: **Low redshift variation in $w(z)$ from $H(z)$ and $D_t(z)$.** Incorrectly assuming concordance values of $\Omega_m = 0.3$ and $\Omega_k = 0$ results in a variation in the low-redshift value of $w(z)$ reconstructed from observables. The relationship between the error in the cosmological parameter and the reconstructed value for w (while keeping the other cosmological parameter fixed at the prior value) is shown for both Ω_m (**green curve**) and Ω_k (**blue curve**). Published in [120].

4.5 Expansions of the Background Observables

We have illustrated the how incorrectly assuming flatness or the concordance value of the matter density can yield a dark energy that mimics dynamics, when considering perfect measurements of background observables in the FLRW model. To illustrate the dependency of the background observables on these parameters we expand them in terms of the cosmological parameters ϵ_m, Ω_k and the parameter $x = z/(1+z)$. Here ϵ_m is defined to be $\epsilon = \Omega_{m*} - \Omega_m$, where Ω_{m*} is the true value of the matter energy density and Ω_m is the assumed value, as seen in Eq. (4.11).

The expansions for $H(x), d_L(x), V'(x)$ yield

$$x = \frac{z}{1+z}$$

$$H(x) = H_0\left[1 + \frac{1}{2}\{3(1+w_0(1-\Omega_{m*}))x - (1+3w_0)\Omega_k x - 3w_0\epsilon_m\}\right] \tag{4.12}$$

$$d_L(x) = \frac{cx}{H_0}\left[1 + \{(5+3w_0(\Omega_{m*}-1)) + (1+3w_0)\Omega_k + 3w_0\epsilon_m\}x\right] \tag{4.13}$$

$$V'(x) = \frac{c^3x^2}{H_0^3}\left[1 + \{(-1+3w_0(\Omega_{m*}-1)) + (1+3w_0)\Omega_k + 3w_0\epsilon_m\}x\right] \tag{4.14}$$

It can be seen from Equations (4.12)-(4.14) that the leading term corresponds to that of the standard flat ΛCDM model, which makes sense since we are expanding the observables around concordance. However, from these equations we can directly compute the error on the particular observable *as a function of redshift* based on the difference between the 'true' cosmology and the 'assumed' cosmological model.

4.6 Connection to the Parametric Approach

In Section 4.2 we considered how curvature degrades the constraints on the coefficients in a standard parametrisation of dark energy, the Chevallier-Polarksi-Linder (CPL) parametrisation [82, 83], which is used in the Dark Energy Task Force report [60]. We now also want to connect the non-parametric approach we have developed to such standard parametric reconstructions of dark energy. We expand Eqs. (4.4) and (4.5) for the Hubble rate and distance measurements to first order in $x = z/(1+z)$, which is the variable used in the CPL expansion. The values of w_0, w_a obtained using this expansion are given below.

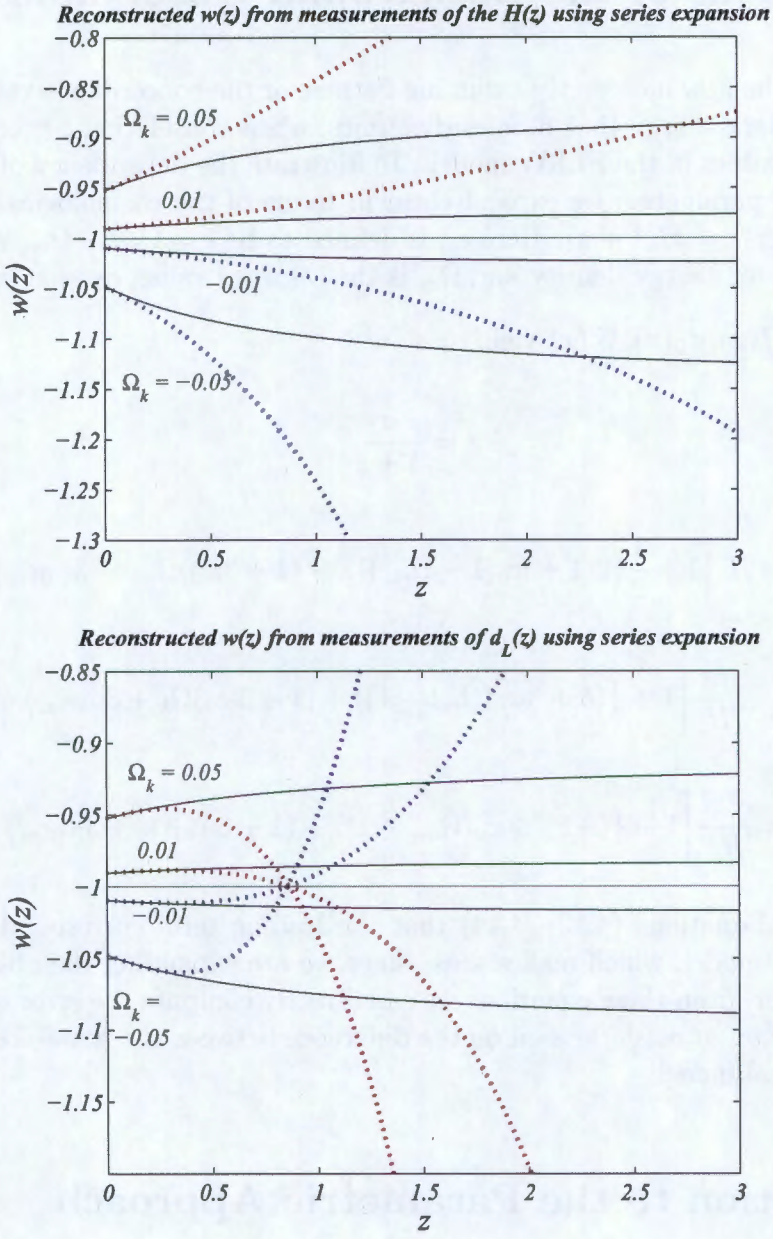

Figure 4.9: **Degeneracies in standard parametrisations.** The parametrisation $w(z) = w_0 + w_a \frac{z}{1+z}$ using the coefficients in Eqs. (4.16) and (4.15) **(solid lines)** is compared with the fully non-parametric $w(z)$ inferred from Hubble and distance measurements **(dashed lines)**. The red and blue lines correspond to values of Ω_k, as in Figure 4.5. Using a limited parametrisation of $w(z)$ like this incorrectly makes it appear that dark energy and curvature are not completely degenerate, leading to artificially strong constraints on curvature and w_0, w_a. Published in [120].

- w_0, w_a from Hubble rate measurements

$$\begin{aligned} w_0 &= -\frac{\Omega_k + 3\Omega_{\rm DE}}{3(1-\Omega_m)} \\ w_a &= \frac{4}{3}\frac{\Omega_k\Omega_{\rm DE}}{(1-\Omega_m)^2} \end{aligned} \tag{4.15}$$

- w_0, w_a from luminosity distance measurements

$$\begin{aligned} w_0 &= -\frac{\Omega_k + 3\Omega_{\rm DE}}{3(1-\Omega_m)} \\ w_a &= -\frac{2}{3}\frac{\Omega_k(\Omega_k - \Omega_{\rm DE})}{(1-\Omega_m)^2} \end{aligned} \tag{4.16}$$

We plot in Figure 4.9 the non-parametric reconstructed $w(z)$ along with the reconstructed $w_{CPL}(z)$ from the coefficients given by Eqs. (4.15, 4.16) for the observables $H(z)$ and $d_L(z)$. The key idea is that in compression $w(z)$ (or similarly $w(x = z/(1+z))$) into a specific functional form it can appear to break the degeneracy, by yielding constraints on the parameters in the expansion. However we see from Figure 4.9 that the these constraints are artificial, since by restricting it in this way does not allow the function enough freedom to reconstruct the true nature of the dynamics.

4.7 Conclusions

Pinning down the nature of dark energy, and detecting any possible dynamics are some of the most important challenges in contemporary cosmology. We have shown that dark energy is, however, degenerate with cosmic parameters such as Ω_k and Ω_m. We have illustrated the need for including curvature in dark energy analyses, by showing both how dark energy mimics curvature in a non-parametric approach, and how curvature degrades dark energy constraints when imposing a specific form for the dynamical nature of the equation of state $w(z)$. Independent measurements of the background observables help to break this degeneracy, and so combining multiple data sets gives some hope to the problem. We note, however, that at the background level the degeneracy between matter and dark energy is perfect, and we need to go to measurements of perturbations, from measurements of the growth function, for example, in order to disentangle matter from dark energy.

Chapter 5

Conclusions

Figure 5.1: © Jorge Cham, online at www.phdcomics.com 30/8/2005

Dark energy is a very active research area in modern cosmology, in both the theoretical and observational sectors of the community. Understanding the nature of dark energy is one of the key outstanding questions in contemporary physics. Much emphasis is placed on testing for the deviations from the simplest 'vanilla' ΛCDM cosmology, both in current experiments and planned surveys. Searching for possible signatures of redshift evolution in the dark energy is key to such experiments.

Future surveys such as the Dark Energy Survey (DES) [58], the Wide-Field Multi-Object Spectrograph (WFMOS) [40, 61], SkyMapper [129], Pan-Starrs [130], the Stage IV Experiments Large Synoptic Survey Telescope (LSST) [53, 62], the Supernova Acceleration Probe (SNAP) [52], EUCLID (a combination of the DUNE [131] and SPACE [132] proposals) will take optical and near-infrared observations, while PLANCK [114] will take precise measurements of the CMB, and DETF Stage IV experiments in the radio regime like the SKA [133] (and its technology demonstrators from South Africa [134] and Australia [135]) will use measurements of neutral hydrogen in the cosmic 'dark ages' to constrain dark energy.

Big Bang Nucleosynthesis provides strong constraints on the amount of dark energy in the early universe. In Chapter 2 we show that such early universe constraints on scaling models of dark energy imply that these well-motivated models will be essentially indistinguishable from ΛCDM for the next ten years until the Dark Energy Task Force Stage IV experiments [60]. We discuss observables in a particular example of a scaling model, the polynomial parametrisation for dark energy.

Chapter 3 was concerned with the use and limitations of the Fisher Matrix. After introducing the Fisher Matrix formalism, we derived Fisher Flex corrections from higher order derivatives of the log likelihood. For any survey, this formalism allows one to check whether the Fisher Matrix analysis will suffice in making parameter estimation forecasts. This is motivated by the (often highly) non-Gaussian nature of the error ellipses from real data.

In Chapter 4 we investigate the degeneracies between dark energy and the curvature and matter densities of the Universe, and highlight the need to include curvature as a free parameter in dark energy analysis. We used a Fisher Matrix analysis to illustrate the degradation of constraints on dark energy parameters as we increase the uncertainty in the curvature of the Universe. Using measurements of the background observables $H(z)$, $d_A(z)$ (or $d_L(z)$) and dV/dz we can reconstruct $w(z)$ fully without assuming a particular parametrisation. We showed how a curved Universe with a cosmological constant can mimic a flat Universe with dynamical dark energy, and applied the same analysis to incorrect assumptions of the true matter density of the Universe. In the case of matter, however, the degeneracy with dark energy is perfect.

There are many challenges on the road of discovery, and great physical insight is needed in coming years to unravel the mystery that is dark energy. It is just these challenges, however, that make the hunt for dark energy that much more enjoyable.

Bibliography

[1] Mather, J. C., Cheng, E. S., Eplee, R. E., Jr., *et al.*, ApJ **354**, L37 (1990).

[2] Reichardt, C. L., Ade, P. A. R., Bock, J. J., *et al.*, (2008), arXiv:0801.1491.

[3] Balbi, A., Ade, P., Bock, J., *et al.*, ApJ **558**, L145 (2001), arXiv:astro-ph/0005124.

[4] Readhead, A. C. S., Mason, B. S., Contaldi, C. R., *et al.*, ApJ **609**, 498 (2004), arXiv:astro-ph/0402359.

[5] Jones, W. C., Ade, P. A. R., Bock, J. J., *et al.*, ApJ **647**, 823 (2006), arXiv:astro-ph/0507494.

[6] Komatsu, E., Dunkley, J., Nolta, M. R., *et al.* (2008), arXiv:0803.0547.

[7] Nolta, M. R., Dunkley, J., Hill, R. S., *et al.* (2008), arXiv:0803.0593.

[8] Guth, A. H., Phys. Rev. D **23**, 347 (1981).

[9] Kazanas, D., ApJ **241**, L59 (1980).

[10] Sato, K., MNRAS **195**, 467 (1981a).

[11] Sato, K., Physics Letters B **99**, 66 (1981b).

[12] Starobinskij, A. A., Physics Letters B **91**, 99 (1980).

[13] Bassett, B. A., Tsujikawa, S., and Wands, D., Reviews of Modern Physics **78**, 537 (2006), arXiv:astro-ph/0507632.

[14] Kolb, E. W. and Turner, M. S., *The early universe* (Frontiers in Physics, Reading, MA: Addison-Wesley, 1990).

[15] Liddle, A. R. and Lyth, D. H., *Cosmological Inflation and Large-Scale Structure* (Cambridge, UK: Cambridge University Press, 2000).

[16] Linde, A. (2005), arXiv:hep-th/0503203.

[17] Mukhanov, V., *Physical foundations of cosmology* (Cambridge, UK: Cambridge University Press, 2005).

[18] Hubble, E., Proceedings of the National Academy of Science **15**, 168 (1929).

[19] Rubin, D., Linder, E. V., Kowalski, M. (2008), arXiv:0807.1108.

[20] Perlmutter, S., Aldering, G., Goldhaber, G., *et al.*, ApJ **517**, 565 (1999a), arXiv:astro-ph/9812133.

[21] Riess, A. G., Filippenko, A. V., Challis, P., *et al.*, AJ **116**, 1009 (1998), arXiv:astro-ph/9805201.

[22] Carroll, S. M. (1997) arXiv:gr-qc/9712019.

[23] Wald, R. M., *General relativity* (Chicago, University of Chicago Press, 1984, 504 p., 1984).

[24] Bassett, B. and Edney, R., *Introducing Relativity* (Thriplow, Icon, 2006).

[25] *http://nrumiano.free.fr/ecosmo/cg_relat.html.*

[26] *http://cmb.phys.cwru.edu/boomerang/press_images/index.html.*

[27] *http://cas.sdss.org/dr6/en/.*

[28] Dunlop, J., Peacock, J., Spinrad, H., *et al.*, Nature **381**, 581 (1996).

[29] Spinrad, H., Dey, A., Stern, D., *et al.*, ApJ **484**, 581 (1997), arXiv:astro-ph/9702233.

[30] Tegmark, M., Eisenstein, D. J., Strauss, M. A., *et al.*, Phys. Rev. D **74**, 123507 (2006a), arXiv:astro-ph/0608632.

[31] Percival, W. J., Nichol, R. C., Eisenstein, D. J., *et al.*, ApJ **657**, 51 (2007a), arXiv:astro-ph/0608635.

[32] Eisenstein, D. J., Zehavi, I., Hogg, D. W., *et al.*, ApJ **633**, 560 (2005), arXiv:astro-ph/0501171.

[33] Seo, H.-J. and Eisenstein, D. J., ApJ **598**, 720 (2003), arXiv:astro-ph/0307460.

[34] Blake, C. and Glazebrook, K., ApJ **594**, 665 (2003), arXiv:astro-ph/0301632.

[35] Tegmark, M., Eisenstein, D. J., Strauss, M. A., *et al.*, Phys. Rev. D **74**, 123507 (2006b), arXiv:astro-ph/0608632.

[36] Hogg, D. W. (1999), arXiv:astro-ph/9905116.

[37] Hamilton, A. J. S., in *The Evolving Universe*, edited by Hamilton, D. (1998) **231** 185 (1998).

[38] Bassett, B. A. and Kunz, M., Phys. Rev. D **69**, 101305 (2004), arXiv:astro-ph/0312443.

[39] Gaztanaga, E., Cabre, A., and Hui, L. (2008), arXiv:0807.3551.

[40] Bassett, B. A., Nichol, R. C., Eisenstein, D. J., *et al.*, A&G **46**, 5.26 (2005).

[41] *http://www.sdss3.org.*

[42] *http://www7.nationalacademies.org/ssb/be_nov_2006_bennett.pdf.*

[43] Daly, R. A. and Guerra, E. J., AJ **124**, 1831 (2002), arXiv:astro-ph/0209503.

[44] Jackson, J. C. and Dodgson, M., MNRAS **285**, 806 (1997), arXiv:astro-ph/0605102.

[45] Jackson, J. C., Journal of Cosmology and Astro-Particle Physics **11**, 7 (2004), arXiv:astro-ph/0309390.

[46] Mantz, A., Allen, S. W., Ebeling, H., *et al.*, MNRAS **387**, 1179 (2008), arXiv:0709.4294.

[47] *http://universeadventure.org/fundamentals/lightmagnitude.htm.*

[48] Perlmutter, S., Aldering, G., Goldhaber, G., *et al.*, ApJ **517**, 565 (1999b), arXiv:astro-ph/9812133.

[49] Riess, A. G., Kirshner, R. P., Schmidt, B. P., *et al.*, AJ **117**, 707 (1999), arXiv:astro-ph/9810291.

[50] Hamuy, M., Phillips, M. M., Suntzeff, N. B., *et al.*, AJ **112**, 2398 (1996a), arXiv:astro-ph/9609062.

[51] Hamuy, M., Phillips, M. M., Suntzeff, N. B., *et al.*, AJ **112**, 2391 (1996b), arXiv:astro-ph/9609059.

[52] SNAP Collaboration (2005), arXiv:astro-ph/0507459.

[53] Tyson, J. A., in *Survey and Other Telescope Technologies and Discoveries. Edited by Tyson, J. Anthony; Wolff, Sidney. Proceedings of the SPIE, Volume 4836, pp. 10-20 (2002).*, edited by Tyson, J. A. and Wolff, S. (2002), pp. 10–20.

[54] Davis, M., Gerke, B. F., and Newman, J. A. (2004), arXiv:astro-ph/0408344.

[55] *http://www.physics.princeton.edu/act.*

[56] Kosowsky, A., New Astronomy Review **47**, 939 (2003), arXiv:astro-ph/0402234.

[57] Ruhl, J., Ade, P. A. R., Carlstrom, J. E., *et al.*, in *Millimeter and Submillimeter Detectors for Astronomy II* Aguirre, J. E., *et al.* (2004), vol. 5498 of *Presented at the Society of Photo-Optical Instrumentation Engineers (SPIE) Conference*, pp. 11–29.

[58] The Dark Energy Survey Collaboration (2005), arXiv:astro-ph/0510346.

[59] Gerke, B. F., Newman, J. A., Davis, M., *et al.*, ApJ **625**, 6 (2005), arXiv:astro-ph/0410721.

[60] Albrecht, A. and Bernstein, G. (2006), arXiv:astro-ph/0608269.

[61] Bassett, B. A., Nichol, B., and Eisenstein, D. J., Astronomy and Geophysics **46**, 26 (2005), arXiv:astro-ph/0510272.

[62] *http://www.lsst.org.*

[63] Turner, M. S. (1997), arXiv:astro-ph/9703161.

[64] Turner, M. S., (1997), arXiv:astro-ph/9703195.

[65] Turner, M. S., (1997), arXiv:astro-ph/9703196.

[66] Turner, M. S., (1997), arXiv:astro-ph/9703197.

[67] *http://www-supernova.lbl.gov/.*

[68] Sullivan, M. and SNLS Collaboration, American Astronomical Society Meeting Abstracts **208**, 58.03 (2006).

[69] Sollerman, J., Aguilera, C., Becker, A., *et al.* (2005), arXiv:astro-ph/0510026.

[70] Riess, A. G., Strolger, L.-G., Casertano, S., *et al.*, ApJ **659**, 98 (2007), arXiv:astro-ph/0611572.

[71] Riess, A. G., Strolger, L.-G., Tonry, J., *et al.*, ApJ **607**, 665 (2004), arXiv:astro-ph/0402512.

[72] Chae, K.-H., Biggs, A. D., Blandford, R. D., *et al.*, Physical Review Letters **89**, 151301 (2002), arXiv:astro-ph/0209602.

[73] *http://www.aoc.nrao.edu/ smyers/class.html.*

[74] *http://www.jb.man.ac.uk/research/gravlens/class/class.html.*

[75] Allen, S. W., Schmidt, R. W., Ebeling, H., *et al.*, MNRAS **353**, 457 (2004), arXiv:astro-ph/0405340.

[76] Allen, S. W., Schmidt, R. W., and Fabian, A. C., MNRAS **334**, L11 (2002), arXiv:astro-ph/0205007.

[77] Bahcall, N. A., Dong, F., Bode, P., *et al.*, ApJ **585**, 182 (2003), arXiv:astro-ph/0205490.

[78] Knop, R. A., Aldering, G., Amanullah, R., *et al.*, ApJ **598**, 102 (2003), arXiv:astro-ph/0309368.

[79] Clarkson, C., Bassett, B., and Lu, T. H.-C., Physical Review Letters **101**, 011301 (2008), arXiv:0712.3457.

[80] Copeland, E. J., Sami, M., and Tsujikawa, S., Int. J. Mod. Phys. D **15** (2006).

[81] Weller, J. and Albrecht, A., Phys. Rev. D **65**, 103512 (2002a), arXiv:astro-ph/0106079.

[82] Chevallier, M. and Polarski, D., Int. J. Mod. Phys. D **10**, 213 (2001).

[83] Linder, E. V., Phys. Rev. Lett. **90**, 091301 (2003), arXiv:astro-ph/0208512.

[84] Corasaniti, P. S., Kunz, M., Parkinson, D., *et al.*, Phys. Rev. D **70**, 083006 (2004), arXiv:astro-ph/0406608.

[85] Bassett, B. A., Kunz, M., Silk, J., *et al.*, MNRAS **336**, 1217 (2002), arXiv:astro-ph/0203383.

[86] Kinney, W. H., Phys. Rev. D **66**, 083508 (2002), arXiv:astro-ph/0206032.

[87] Bassett, B., *Private Communication* (2008).

[88] Bassett, B. A., Brownstone, M., Cardoso, A., *et al.*, JCAP **007** (2008a).

[89] Mukhanov, V., International Journal of Theoretical Physics **43**, 669 (2004), arXiv:astro-ph/0303073.

[90] Weinberg, S., *Gravitation and Cosmology: Principles and Applications of the General Theory of Relativity* (Wiley-VCH 1972).

[91] Burles, S., Nollett, K. M., and Turner, M. S. (1999), arXiv:astro-ph/9903300.

[92] Fields, B. and Sarkar, S., *Big-Bang nucleosynthesis*, in Yao, W.-M. and et al., Journal of Nuclear Physics G **33**, 1 (2006), arXiv:astro-ph/0601514.

[93] Bean, R., Hansen, S. H., and Melchiorri, A., Phys. Rev. D **64**, 103508 (2001a), arXiv:astro-ph/0104162.

[94] Burles, S., Nollett, K. M., and Turner, M. S., Phys. Rev. D **63**, 063512 (2001), arXiv:astro-ph/0008495.

[95] Izotov, Y. I., Thuan, T. X., and Stasińska, G., ApJ **662**, 15 (2007), arXiv:astro-ph/0702072.

[96] Olive, K. A., Steigman, G., and Walker, T. P., Phys. Rep. **333**, 389 (2000), arXiv:astro-ph/9905320.

[97] Cyburt, R. H., Fields, B. D., and Olive, K. A. (2008), arXiv:0808.2818.

[98] Ellis, J. (2003), arXiv:astro-ph/0305038.

[99] Ferreira, P. G. and Joyce, M., Phys. Rev. D **58**, 023503 (1998).

[100] Ferreira, P. G. and Joyce, M., Physical Review Letters **79**, 4740 (1997), arXiv:astro-ph/9707286.

[101] Barreiro, T., Copeland, E. J., and Nunes, N. J., Phys. Rev. D **61**, 127301 (2000).

[102] Copeland, E. J., Liddle, A. R., and Wands, D., Phys. Rev. D **57**, 4686 (1998), arXiv:gr-qc/9711068.

[103] Bean, R., Hansen, S. H., and Melchiorri, A., Phys. Rev. D **64**, 103508 (2001b).

[104] Doran, M., Karwan, K., and Wetterich, C., J.C.A.P. **11**, 7 (2005).

[105] Doran, M. and Robbers, G., J.C.A.P. **6**, 26 (2006).

[106] Weller, J. and Albrecht, A., Phys. Rev. D **65**, 103512 (2002b).

[107] Bassett, B. A., Fantaye, Y. T., Hlozek, R. A. and Kotze, J., *In preparation.* (2008).

[108] Mackay, D. J. C., *Information Theory, Inference, and Learning Algorithms* (Cambridge University Press, 2003).

[109] Tegmark, M., Taylor, A. N., and Heavens, A. F., ApJ **480**, 22 (1997), arXiv:astro-ph/9603021.

[110] Matsubara, T., ApJ **615**, 573 (2004), arXiv:astro-ph/0408349.

[111] *http://www.cosmology.org.za.*

[112] Cooray, A., Huterer, D., and Baumann, D., Phys. Rev. D **69**, 027301 (2004), arXiv:astro-ph/0304268.

[113] Zhan, H., Wang, L., Pinto, P., *et al.*, ApJ **675**, L1 (2008), arXiv:0801.3659.

[114] *http://www.rssd.esa.int/index.php?project=planck.*

[115] Bassett, B. A., Phys. Rev. D **71**, 083517 (2005), arXiv:astro-ph/0407201.

[116] Huterer, D. and Turner, M. S., Phys. Rev. D **64**, 123527 (2001), arXiv:astro-ph/0012510.

[117] Maor, I., Brustein, R., and Steinhardt, P. J., Physical Review Letters **86**, 6 (2001), arXiv:astro-ph/0007297.

[118] Huterer, D. and Turner, M. S., AIP CONF.PROC. **599**, 140 (2001), arXiv:astro-ph/0006419.

[119] Perotto, L., Lesgourgues, J., Hannestad, S., *et al.*, Journal of Cosmology and Astro-Particle Physics **10**, 13 (2006), arXiv:astro-ph/0606227.

[120] Hlozek, R., Cortês, M., Clarkson, C., *et al.*, General Relativity and Gravitation **40**, 285 (2008), arXiv:0801.3847.

[121] Kunz, M. (2007), arXiv:0710.5712.

[122] Clarkson, C., Cortês, M., and Bassett, B., Journal of Cosmology and Astro-Particle Physics **8**, 11 (2007), arXiv:astro-ph/0702670.

[123] Linder, E. V., Astroparticle Physics **24**, 391 (2005), arXiv:astro-ph/0508333.

[124] Huang, Z.-Y., Wang, B., and Su, R.-K., International Journal of Modern Physics A **22**, 1819 (2007), arXiv:astro-ph/0605392.

[125] Percival, W. J., Cole, S., Eisenstein, D. J., *et al.*, MNRAS **381**, 1053 (2007b), arXiv:0705.3323.

[126] Freedman, W. L., Madore, B. F., Gibson, B. K., *et al.*, ApJ **553**, 47 (2001), arXiv:astro-ph/0012376.

[127] Glazebrook, K., Blake, C., Couch, W., *et al.* (2007), arXiv:astro-ph/0701876.

[128] Huterer, D. and Turner, M. S., Phys. Rev. D **64**, 123527 (2001), arXiv:astro-ph/0012510.

[129] Schmidt, B. P., Keller, S. C., Francis, P. J., *et al.*, Bulletin of the American Astronomical Society **37**, 457 (2005).

[130] Kaiser, N. and Pan-STARRS Team, in *Bulletin of the American Astronomical Society* (2005), p. 1409.

[131] Refregier, A., Douspis, M., and the DUNE collaboration (2008), arXiv:0807.4036.

[132] Cimatti, A., Robberto, M., Baugh, C., *et al.*, Experimental Astronomy pp. 12 (2008), arXiv:0804.4433.

[133] Blake, C. A., Abdalla, F. B., Bridle, S. L., *et al.*, New Astronomy Review **48**, 1063 (2004), arXiv:astro-ph0409278.

[134] *http//www.ska.ac.za.*

[135] Johnston, S., Bailes, M., Bartel, N., *et al.*, Publications of the Astronomical Society of Australia **24**, 174 (2007), arXiv:0711.2103.

Appendix A

Tensor Algebra

We give an introduction to the mathematic of General Relativity, which we have assumed in the thesis. The first of these concepts is the definition of a vector and its dual vector, a one-form.

Vectors are usually represented in terms of linear combinations of basis vectors, as

$$\underline{\mathbf{v}} = v^{\alpha}\underline{\mathbf{e}_{\alpha}}. \tag{A.1}$$

We make use of the Einstein summation convention, to express a sum. As an example, this notation expresses the sum

$$v^{0}\underline{\mathbf{e_0}} + v^{1}\underline{\mathbf{e_1}} + v^{2}\underline{\mathbf{e_2}} + v^{3}\underline{\mathbf{e_3}} \tag{A.2}$$

simply as the expression given as Eq. (A.1). It is also worth noting that the Greek subscripts or superscripts refer to vectors with four components; one time (indicated by the index 0) and three space components (indicated by i). This means that vectors are normally specified completely just by the coefficient, v^{α}. In the same way one-forms can be represented in terms of a set of basis one-forms, as

$$\widetilde{\mathbf{w}} = w_{\alpha}\widetilde{\mathbf{e}^{\alpha}}, \tag{A.3}$$

again with the coefficient w_{α} specifying the one-form. The basis of one-forms is defined so that

$$\widetilde{\mathbf{e}^{\mu}}(\underline{\mathbf{e}_{\nu}}) = \delta^{\mu}_{\nu}, \tag{A.4}$$

with δ^{ν}_{μ} the Kronecker delta, which is zero for all indices where $\mu \neq \nu$ and one when $\mu = \nu$. This means that when a one-form **acts** on a vector as

$$\begin{aligned}
\widetilde{\mathbf{w}}(\underline{\mathbf{v}}) &= w_{\mu}\widetilde{\mathbf{e}^{\mu}}v^{\nu}\underline{\mathbf{e}_{\nu}} \\
&= w_{\mu}v^{\nu}\widetilde{\mathbf{e}^{\mu}}\underline{\mathbf{e}_{\nu}} \\
&= w_{\mu}v^{\nu}\delta^{\mu}_{\nu} \\
&= w_{\mu}v^{\nu} \\
&= \underline{\mathbf{v}}(\widetilde{\mathbf{w}}),
\end{aligned} \tag{A.5}$$

where we make use of the fact that the one-forms and vectors are linear maps to $\mathbb{R}$.

This leads us to the definition of a tensor, which can be seen as a generalisation of the concept of scalars and vectors. A broad definition of a tensor of rank (n,m) is a multi-linear map from n one-forms and m vectors to the real numbers, $\mathbb{R}$. In that definition, we can think of a scalar as a tensor of rank (0,0), a one-form as a tensor of rank (0,1) (since one-forms maps vectors linearly to the real numbers) and vectors can be seen as tensors of rank (1,0).

We may define a linear transformation of co-ordinates from $x^\mu \rightarrow x^{\mu'}$ as $x^{\mu'} = \Lambda^{\mu'}_{\ \nu} x^\nu$. A special set of these transformations central to GR are the Lorentz transformations which preserves the spacetime interval between any two points in Minkowski space.

The key idea with tensors is that they are invariant under a change of co ordinates. This means that identities that hold true for a tensor in one set of co ordinates, will still hold in any other set of co ordinates. Mathematically we see that a general tensor of rank (n,m) $T^{\mu_1 \ldots \mu_n}_{\quad \nu_1 \ldots \nu_m}$, transforms as [22]:

$$T^{\mu'_1 \ldots \mu'_n}_{\quad \nu'_1 \ldots \nu'_m} = \left[\Lambda^{\mu'_1}_{\ \lambda_1} \ldots \Lambda^{\mu'_n}_{\ \lambda_n} \Lambda^{\sigma_1}_{\ \nu'_1} \ldots \Lambda^{\sigma_m}_{\ \lambda'_m} \right] T^{\lambda_1 \ldots \lambda_n}_{\quad \sigma_1 \ldots \sigma_m}, \tag{A.6}$$

with one transformation for each 'up' and 'down' index of the tensor. This transformation property of tensors is central to General Relativity. An important tensor in GR is that of the **metric tensor**. Mathematically the metric $g_{\alpha\beta}$ is defined by the inner (or dot) product of two vectors, as

$$\begin{aligned} \underline{\mathbf{u}} \cdot \underline{\mathbf{v}} &= (u^\alpha \underline{\mathbf{e}_\alpha}) \cdot (v^\beta \underline{\mathbf{e}_\beta}) \\ &= u^\alpha v^\beta \underline{\mathbf{e}_\alpha} \cdot \underline{\mathbf{e}_\beta} \\ &\equiv u^\alpha v^\beta g_{\alpha\beta}. \end{aligned} \tag{A.7}$$

Given the definition for the metric, we can also define an inverse metric, $g^{\alpha\beta}$ so that the product $g^{\alpha\beta} g_{\beta\gamma} = g_{\gamma\beta} g^{\beta\alpha} = \delta^\alpha_\gamma$.

We can use the metric (and its inverse) to raise and lower indices of general tensors. For example, we write

$$t^{\beta\gamma}_\alpha = g_{\alpha\nu} t^{\nu\beta\gamma}. \tag{A.8}$$

Similarly, we can perform contraction over indices, which indicates that we are actually performing a dot product over those indices, or sum over the components of the tensor, or $u_\beta = u^\gamma_{\beta\gamma}$. The index γ in the last example is referred to as a 'dummy' variable, since it only shows contraction and does not take part in the tensor expression. We take care to ensure that repeated indices in any tensor expression or equation indicate contraction, and so when using dummy indices in tensor equations, make sure to place them correctly.

✠